FINAL REPORT

For the U.S. Department of Transportation Solicitation #DTPH56-07-BAA-000002
Under Contract Number DTPH56-08-T-000009

MWM-ARRAY DETECTION AND CHARACTERIZATION OF DAMAGE THROUGH COATINGS AND INSULATION

Prepared for

James Merritt
U.S. Department of Transportation
Pipeline and Hazardous Materials Safety Administration
Office of Pipeline Safety
793 Countrybriar Lane
Highlands Ranch, CO 80129

By JENTEK Sensors, Inc.
110-1 Clematis Avenue
Waltham, Massachusetts 02453-7013
(781) 642-9666
jentek@shore.net

February 28, 2011

Table of Contents

1 Executive Summary

This report describes the results of a development project aimed at providing rapid nondestructive evaluation (NDE) methods for the detection of damage in carbon steel pipelines through coatings and insulation. This was accomplished by adapting JENTEK's MWM-Array technology to accommodate the coating thicknesses and properties typically used in the oil and gas industry. The MWM-Array uses a time-varying magnetic field to induce eddy-currents in the steel components and detects variations in the magnetic field due to damage in the steel component. This technology has been successfully applied in the aerospace and manufacturing industries and provides substantially improved performance for imaging surface and buried damage through coatings and for curved surfaces compared to conventional NDE methods. This project has demonstrated the feasibility of using the MWM-Array technology as an NDE tool for inspection of steel pipelines. We are confident that a fieldable solution based on this technology will be available in the near-future.

This project has achieved a number of milestones toward establishing the feasibility of imaging MWM-Arrays for detection and characterization of damage through protective barrier coatings on pipelines. These include:

- Demonstrated high spatial imaging resolution for near-surface material loss and stress corrosion crack damage through thin (less than 6.35 mm (0.25-in.)) coatings using medium-sized MWM-Arrays in the laboratory.
- Demonstrated high-frequency imaging capability to detect and characterize near-surface material loss through thick (up to 50.8 mm (2.0-in.)) coatings using large-sized arrays in the laboratory.
- Demonstrated high-frequency capability to measure magnetic permeability and coating thickness on flat steel plates for coatings up to 101.6 mm (4.0-in.) thick.
- Demonstrated capability to image mechanical damage through coatings.
- Fabricated two large flexible MWM-Arrays, denoted by VWA001 and VWA003, to image damage through coatings and insulation.
- Fabricated prototype scanners to facilitate imaging steel component material condition.
- Fabricated a large flexible MWM-Array with solid-state sense elements to support low frequency operation.
- Demonstrated feasibility of independently measuring steel magnetic relative permeability, steel thickness, and lift-off for steel plates up to 6.35 mm (0.25-in.) thick. This low-frequency measurement capability allows near-surface and far-surface material loss to be separately identified.
- Performed finite element simulations for sensor array responses over discrete areas of material loss to confirm observed measurement responses and provide means for compensating for flaw geometry effects on material loss depth estimates.

Ongoing work is aimed at improving the scanning fixtures and hardening of the instrumentation for field operation, demonstrating field capabilities for the thicker coatings, and extending capabilities of the impedance measurement instrumentation to lower operating frequencies to accommodate thicker steel walls. This project was complemented by a Chevron program aimed at developing instrumentation for characterizing damage in pipelines, including external and internal corrosion, through barrier coatings.

2 Introduction

Protective barrier coatings are used on risers, piping, and pipelines throughout the oil and gas industry. However, these coatings act as a barrier to inspection and often need to be removed in order to inspect for damage with standard nondestructive evaluation (NDE) methods. The damage in oil and gas pipelines can take a variety of forms, including internal and external corrosion and mechanical damage, with corrosion under insulation (CUI) a common form of damage. Although some NDE methods have been developed for imaging the pipeline through the protective coatings, these methods are typically too slow or require expensive scanners to be used in practical applications. This has led to the need for reliable and lower cost solutions for high resolution imaging of damage from outside the pipeline through coatings. In addition, even after the coatings are removed, it is beneficial to be able to both image and characterize the damage without the coatings.

A wide variety of these protective coatings are used throughout the oil and gas industry. Fusion bonded epoxy (FBE) and other coatings are routinely applied to oil and gas pipelines to prevent contact of the steel with corrosive soil, bacterial, fungal, and moisture environments, with FBE currently the most widely used coating system. An abrasion resistant overcoat is usually applied on top of the first layer of FBE for increased resistance to mechanical damage. Other coating systems that are widely used in pipelines, especially older pipelines, include polyethylene wrap, coal tar enamel, or an enamel tape wrap. Coating methods are often combined. Overall coating thicknesses range from approximately 0.25 mm (0.010-in.) for FBE and polyethylene coatings to 6.35-12.7 mm (0.25-0.50 in.) for the older coal tar coatings. Insulation is typically a dielectric (electrically and thermally insulating) material up to approximately 10 cm (4.-in.) thick that in turn can be surrounded by a metallic foil layer.

In this project, JENTEK's novel Meandering Winding Magnetometer (MWM®) Array technology was adapted to provide an improved method for detection and characterization of damage in pipelines, from the outside, through coatings and insulation. The damage conditions of interest include internal and external corrosion, mechanical damage, and stress corrosion cracking (SCC). This magnetic field-based sensor technology has been successfully applied in the aerospace and manufacturing industries and provides substantially improved performance for imaging surface and buried damage through coatings and for curved surfaces compared to conventional NDE methods [1-5]. Here, the sensor arrays and JENTEK's model-based inverse methods were used to determine electromagnetic and geometric properties of the pipeline material, which are then related to specific damage conditions of interest. The team for this project was JENTEK, Chevron, and Applus/RTD.

3 Project Tasks

This project was part of a consolidated contract aimed at developing instrumentation for characterizing damage in pipelines, including external corrosion, internal corrosion, stress corrosion cracking (SCC), and mechanical damage, with one set of tasks (this project, No. 304) for inspection from outside the pipeline and another (No. 306) for inspection from inside the pipeline. Funding for this project and the consolidated contract is complemented by funding from Chevron on a program titled "Development of Enhanced Inspection Tool through Protective Barriers."

The following summarizes the tasks associated with this project.

Task 1: Develop and demonstrate MWM-Array methods for imaging of external corrosion through relatively thin coatings from outside the pipeline. SCC and mechanical damage will also be addressed.

Task 2: Extend the MWM-Array high frequency external damage imaging capability to support thicker layers of insulation for pipelines.

Task 3: Develop a lower frequency MWM-Array imaging capability for imaging of internal corrosion from the outside of pipelines and to enhance mechanical damage characterization capabilities.

Task 4: Design the field demonstrations and select specific targeted needs.

Task 5: Develop scanners and other needed support equipment for field implementation.

Task 6: Perform fully integrated field demonstration of damage imaging in a representative environment.

Task 7: Develop methods and inputs for training manuals and standards.

Task 8: Evaluate performance and detection capability and recommend follow-on efforts to transition demonstrated capabilities to the field.

Task 9: Submit quarterly reports and a final report.

The first year of the project was aimed at demonstrating an imaging capability for external corrosion, SCC, and mechanical damage through relatively thin coatings in the laboratory. The second year was aimed at extending the capability to permit damage inspection through thicker coatings and to demonstrate field inspection capabilities for thin coatings. The third year was aimed at demonstrating field inspection capabilities for thicker coatings and developing a commercialization and transition plan.

4 Impact from Research Results Section

Eddy current technology is widely used in the aerospace industry and is expected to experience increasing use in petrochemical applications because new eddy current sensor arrays permit rapid and reliable imaging of pipeline material condition. The emphasis of the technology development in this project was on inspection through coatings, but the methods can also be applied to inspections with coatings removed. Both with and without coatings, these methods can provide information about the material condition that can assist with characterization of damage conditions and support assessment decisions. This project helped to establish the capabilities of imaging eddy current sensor arrays for damage inspection and characterization through coatings. This was accomplished through adaptation of the MWM-Array eddy current sensor technology for pipeline materials and demonstration measurements for a variety of inspection applications.

Although a wide variety of coatings are used throughout the oil and gas industry, the sensor design and operating conditions can be adjusted to accommodate the different inspection requirements. For example, although the coating material can vary depending upon the application, such as FBE, coal tar, or some other polymeric material, these coatings are typically electrically insulating. The only property of an insulating coating that affects the eddy current response is the coating thickness. To inspect through this coating, a sensor design with a geometry (e.g., spatial wavelength) that is comparable to the thickness should be used. A sensor with a geometry that is too small would not be able to inspect through the coating and a sensor with a geometry that is too large would have reduced sensitivity to the presence of small features. Similarly, the operating frequency of the instrumentation can be adjusted to accommodate different inspection requirements. Since the induced eddy current density varies with the excitation frequency and is largest on the steel surface nearest the sensor, high excitation frequencies are typically used for near-surface damage inspections. For inspections through the steel wall, for example for internal corrosion damage with an external inspection, low excitation frequencies are required.

The maturity of the MWM-Array technology for pipe and pipeline inspection depends upon the inspection application. For several no coating, very thin and thin coating applications, including imaging of external corrosion and mechanical damage, the technology is mature with capabilities demonstrated. For some applications, such as external corrosion and mechanical damage inspection through moderate thickness coatings (up to 1.0 or 1.5-in.), feasibility has been demonstrated but ongoing work is aimed at improving the inspection capability and refining equipment, such as improved scanner designs to facilitate field-level inspections. For other applications, such as external corrosion inspection through thick coatings, assessment of stresses and damage condition within mechanical damage sites, and far-surface corrosion inspection, additional development is required to extend the capabilities to address these needs.

5 Final Financial Section

This section reviews the financing associated with this project. Table 1 shows that the matching requirements for the project were satisfied. Note that this project was part of a consolidated program with DOT Project 306 and the total amount from partner cost sharing for the consolidated program through the Chevron "Inspection through protective barriers" program as well as Chevron internal expenses was $1,231,301. Of this amount, $555,000. is recognized for cost sharing in Project 304 and the remainder ($676,301.) is available for cost sharing recognition under Project 306.

Table 1. Project Funding Summary.

Project	Abbreviated Title	Expenditures	
		As of 1/31/11	Anticipated by end of Project 304
DOT 304	External inspection through coatings	$499,084.	$502,971.
Partner cost sharing	Chevron "Inspection through protective barriers" program plus Chevron internal expenses	$555,000.	$555,000.
Total		$1,054,084.	$1,057,971.

6 Detailed Technical Results

This section reviews the basic geometry for the MWM and MWM-Arrays, the multivariate inverse methods for converting measurement data into meaningful material and geometric properties, the scanning fixtures developed for use with these sensor arrays, results from numerous demonstration measurements, and issues for transitioning the technology into widespread field-use.

6.1 MWM and MWM-Arrays

MWM and MWM-Arrays are inductive, eddy-current-based sensors that are conformable and provide inspection and monitoring capabilities for conducting materials, such as steel pipeline walls and drill pipe [6]. MWM and MWM-Array technology is covered by numerous U.S. patents including 5,453,689; 5,629,621; 5,793,206; RE39,206; 7,049,811; 7,467,057; and 7,589,526. These patents cover not only the MWM and MWM-Array winding construct, but also the multivariate inverse methods and related calibration and measurement procedures. As shown in Figure 1, the original MWM sensor geometry had a meandering primary winding for creating a spatially periodic magnetic field when driven by an electrical current – hence the MWM name. Secondary windings (sense elements) are located on opposite sides of the primary for sensing the response.

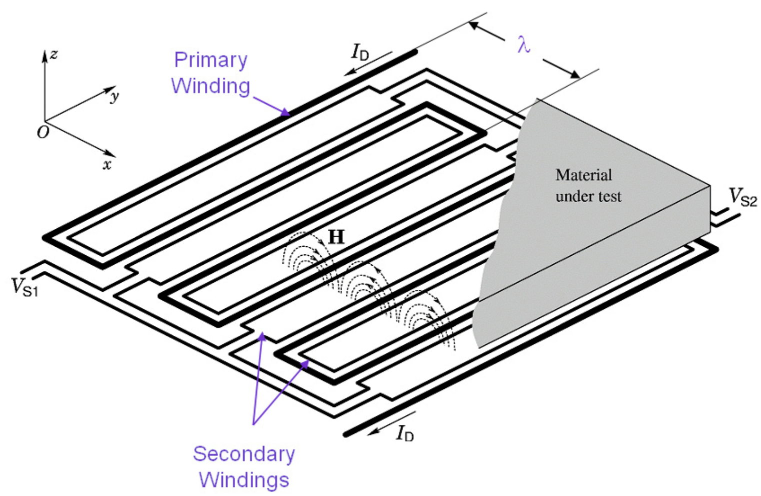

Figure 1. Original MWM sensor geometry [6].

Printed circuit microfabrication techniques are typically employed to produce the sensors, resulting in highly reproducible (i.e., essentially identical) sensors. By fabricating the windings on a thin and flexible substrate, a conformable sensor is produced. These thin and conformable sensors can be scanned across a surface, mounted on an exposed surface, or embedded within or between coating/pipeline layers or under an overwrap or repair. The relatively simple layout for the windings permits operation over a wide frequency range, typically between 1 kHz and 40 MHz. For inspection through steel pipeline walls, for example for internal corrosion inspection from the outside, a lower frequency capability (<100 Hz) is required.

The depth of penetration of the magnetic field into the test material depends upon both the input current frequency and sensor geometry (drive winding spatial wavelength λ) as shown in Figure 2(left). The penetration depth is limited by the skin depth at high frequencies and by the sensor geometry at low frequencies. At low frequencies the magnetic fields from a larger spatial wavelength sensor will penetrate further into the material under test than the fields from a shorter spatial wavelength sensor. Note that the spatial wavelength λ of Figure 1 indicates the spatial periodicity for the drive. For the MWM-Arrays of Figure 3 the relevant dimension is the gap between the drive and sense element, which is defined as λ/4 and illustrated in Figure 2(right).

Thus, while small sensor arrays can be used to create high spatial resolution property images, large sensor arrays are required for inspecting through thick materials, either steels, coatings, or insulation. For bare metal or very thin (less than 0.5 mm (0.020-in.)) coatings, very high resolution imaging is achieved with the FA28 MWM-Array of Figure 3(a). The FA24 MWM-Array shown in Figure 3(b) has larger dimensions than that of the FA28 and permits inspection through thin (up to 6.35 mm (0.25-in.)) coatings. As part of this project, larger versions of the MWM-Arrays were fabricated. The VWA001 MWM-Array shown in Figure 3(c) has a variable spatial wavelength, where the distance between the drive winding and sense element can be adjusted, which enables both deep penetration and relatively high resolution compared to other typical low frequency eddy current methods. The VWA003 MWM-Array shown in Figure 3(d) is similar to the VWA001 except that the drive winding and sensor array are smaller, which makes the sensor array easier to use. For comparison, the VWA001 has a 22-in. long drive winding and the linear array contains thirty-seven sense elements that are 6.5 mm (0.25-in.) square to provide a net scan width of 235 mm (9.25-in.), while the VWA003 has a 9-in. long drive winding and the linear array contains fifteen sense elements that are 6.5 mm (0.25-in.) square to provide a net scan width of 97.5 mm (3.75-in.).

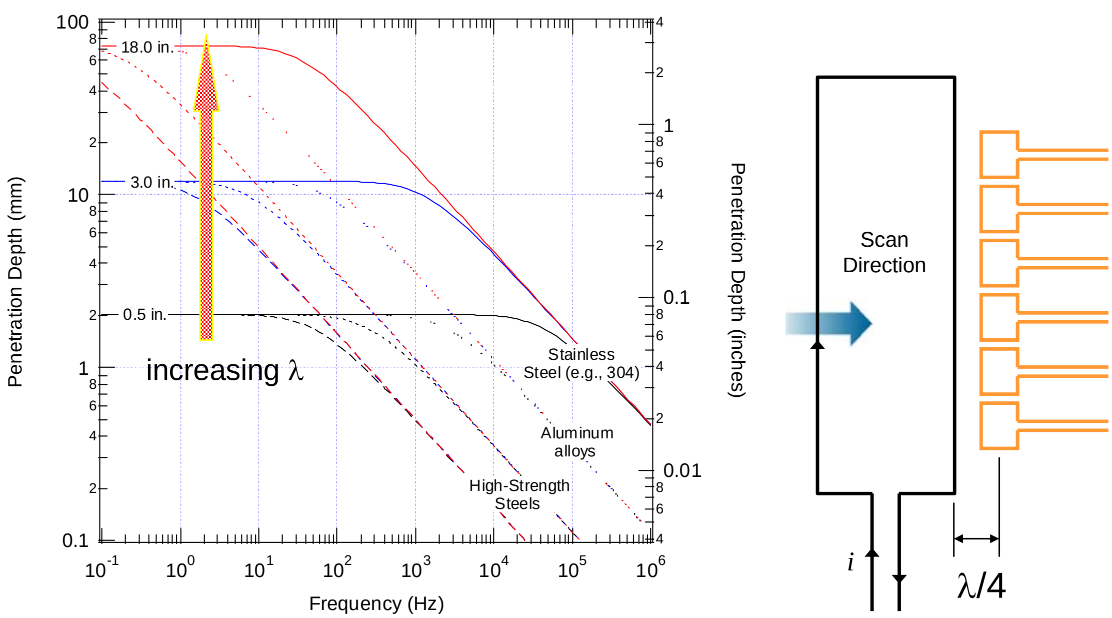

Figure 2. (Left) Depth of penetration variation with sensor dimension. (Right) schematic diagram of a sensor array.

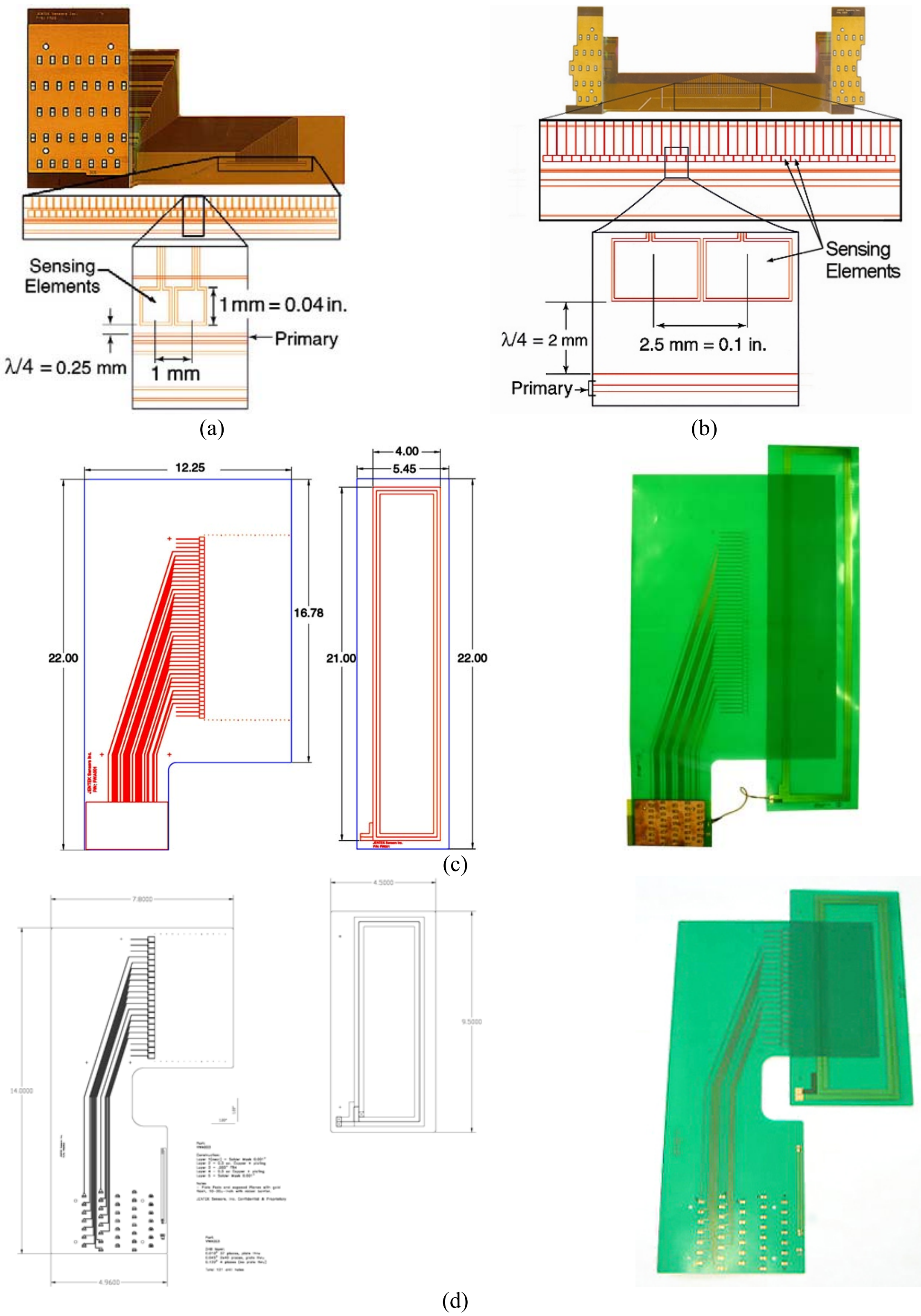

Figure 3. Several MWM-Arrays: (a) FA28; (b) FA24; (c) VWA001; and (d) VWA003 [6].

Several simulations were performed to verify that the dimensions of the arrays were reasonable. These simulations also support the use of low frequency sense elements for scanning through the thickness of the steel pipeline walls. For example, one way to estimate the effect of the finite dimensions of the drive winding on the sense element response is to calculate the field variation along the sense elements when the sensor array is in air. The response in air can be calculated using a "stick-model" for the current carrying wires in the sensor array.

For this analysis, a simplified geometry for the sensor array was used, as shown in Figure 4. For this geometry, assume that the drive winding is a single rectangular loop of dimensions 2*L* and *d* that is placed at a gap distance *g* from a linear array of sense elements. The length of the sense element array is *w*. Assuming that the net current in each leg of the drive winding is *i*, then the current from each segment can be easily evaluated using an algebraic vector form of the Biot-Savart Law for current sticks: [7]

$$\overline{\mathbf{H}} = \frac{i}{4\pi} \frac{\overline{c} \times \overline{a}}{\left|\overline{c} \times \overline{a}\right|^2} \left(\frac{\overline{a} \cdot \overline{c}}{\left|\overline{c}\right|} - \frac{\overline{a} \cdot \overline{b}}{\left|\overline{b}\right|} \right)$$

where, i is the current in the segment, $\overline{b}$ is a vector from the observation point to the start of the segment, $\overline{c}$ is a vector from the observation to the end of the segment, and $\overline{a} = \overline{c} - \overline{b}$. This expression provides the vector magnetic field intensity for arbitrary points around the drive winding. For the analysis here, only the field along the sense element array is to be determined. Assuming that the sensor array is narrower than the drive winding length ($|y| < L$), the field can be expressed as

$$\overline{\mathbf{H}} = \hat{i}_z \frac{i}{4\pi} \left\{ \sqrt{\left(\frac{1}{L-y}\right)^2 + \left(\frac{1}{g+d}\right)^2} + \sqrt{\left(\frac{1}{L+y}\right)^2 + \left(\frac{1}{g+d}\right)^2} - \sqrt{\left(\frac{1}{L-y}\right)^2 + \frac{1}{g^2}} - \sqrt{\left(\frac{1}{L+y}\right)^2 + \frac{1}{g^2}} \right\}$$

where $\hat{i}_z$ is a unit vector in the *z*-direction. Since the drive winding and sense elements are assumed to be in the same plane (*z*=0), the magnetic field is only in the *z*-direction.

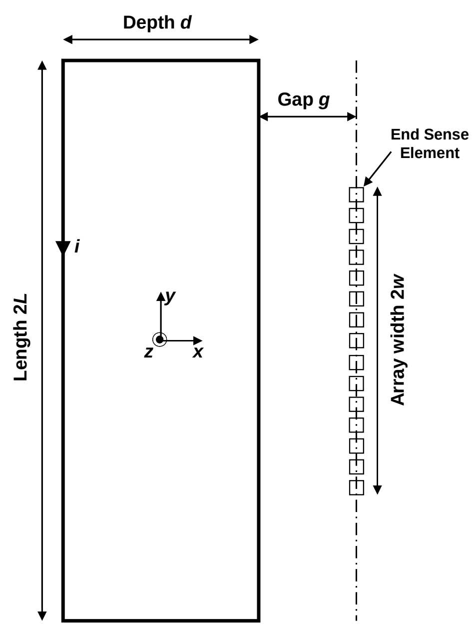

Figure 4. Model geometry for calculating nominal field variation across a linear array of sense elements.

Figure 5 shows the field variation with position along the array of sense elements. The field is at a maximum at the center and decays with position along the array; the field value is normalized to the maximum field at the center of the array. The field is relatively uniform near the center of the array but decreases near the ends of the drive winding. The end effect increases with the gap size and reduces the length over which the field would be considered uniform. Varying the drive winding dimension *d* (or *d/L*) does not have a significant effect on the field distribution in the vicinity of the sense elements; however, this dimension is expected to have an effect on the penetration of the magnetic field through thick coatings or insulation.

Figure 6 shows contour plots of the field variation with gap distance and the end position of the sense element array. The gap distance and sense element array end position are relative to the half-length of the drive winding. The field variation is expressed as a percentage change in the field at the end position of the sense element array compared to the field at the center of the array. The field at the end of the sense element array decreases as the sense element array width and the gap distance becomes large compared to the half-length of the drive winding. For the VWA001, the drive winding is approximately 21-in. long and 4.0-in. wide with a sense element array width of 9.25-in. The drive-sense gap is typically varied from 1.0 to 4.0-in. This yields normalized dimensions of *d/L* =0.381, *w/L* =0.393, and *g/L* from 0.095 to 0.381. From Figure 6, the field variation across the sensor array is less than 5%; since this variation is relatively small, the calibration procedure (air or reference part calibration) is sufficient to remove the baseline variation in the field due to the finite drive winding length.

For comparison, the VWA003 has a drive winding that is approximately 9.0-in. long and 3.0-in. wide with a sense element array width of 3.75-in. that is 1.0-in. from the drive winding. This yields normalized dimensions of *d/L* =0.667, *w/L* =0.417, and *g/L* =0.222. Figure 7 shows the corresponding contour plots of the field variation between the end sense element and the center sense element. For the VWA003, the field variation is expected to be less than 4%, which is comparable to the VWA001.

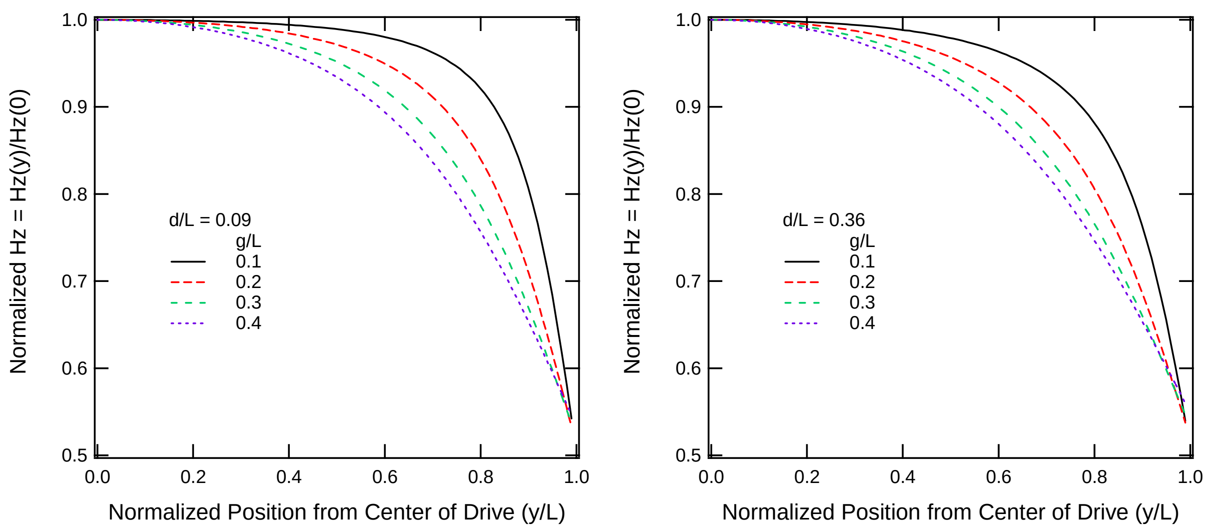

Figure 5. Field variation with position along the sense element array for (left) d/L = 0.09 and (right) d/L = 0.36.

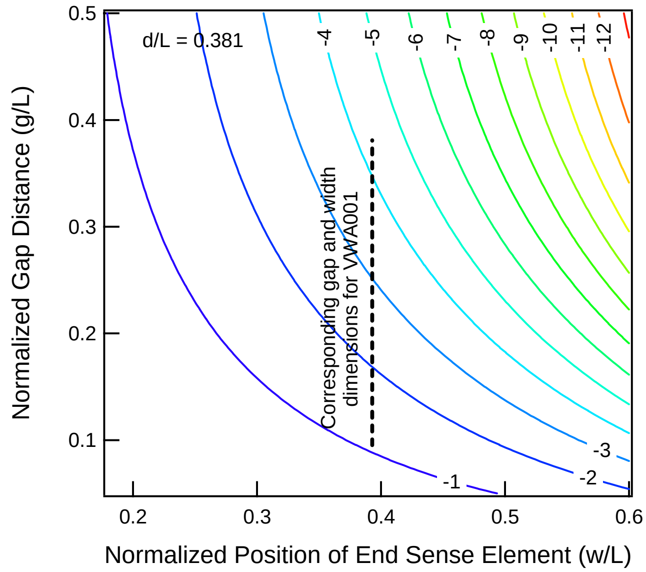

Figure 6. Percent change in field variation at the end sense element compared to a sense element at the center of the array for d/L = 0.381, which corresponds to the dimensions of the VWA001.

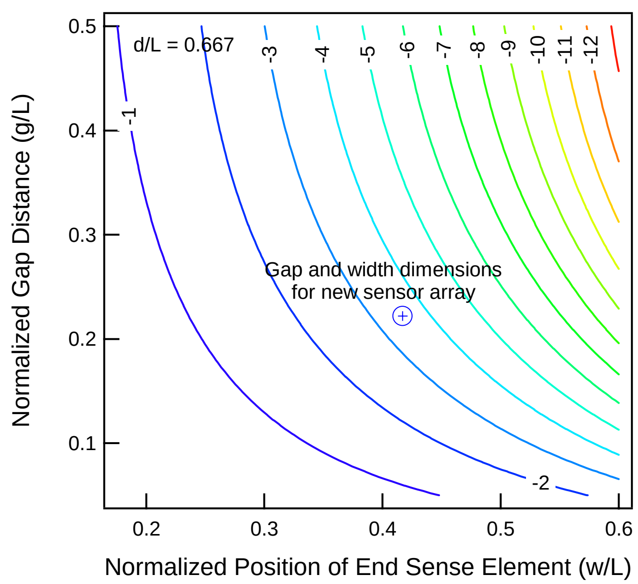

Figure 7. Percent change in field variation at the end sense element compared to a sense element at the center of the VWA003 for d/L = 0.667.

6.2 <u>Measurement Grid Methods</u>

MWM and MWM-Array responses are converted into material or geometric properties using measurement grids [8]. These grids convert two known values, such as the magnitude and phase (or real and imaginary parts) of the transimpedance, into the unknown properties of interest, such as electrical conductivity, magnetic permeability and lift-off. The grids are generated using a forward model and properties of the test material to create two-dimensional databases, or precomputed responses, which can be displayed graphically to support procedure development. Figure 8(left) shows a conductivity/lift-off grid and data from one channel of an MWM-Array in scans performed with four different insulating coating (shim) thicknesses. This figure illustrates how the conductivity and lift-off (representing the total thickness of the insulating layers) can be independently measured. For magnetizable steels, the magnetic permeability is often determined, which in turn is related to the material microstructure and the residual or applied stress at a given location. If the coatings are smooth with at most a gradual thickness variation or the sensor proximity to the surface is maintained with a scanning fixture, then the lift-off provides information about the surface topology and can be used to indicate the presence of near-surface corrosion or damage. Higher-order databases are used for the determination of more than two unknown properties of interest, such as coating thickness (via sensor lift-off or proximity), metal wall thickness, and metal electrical conductivity and/or magnetic permeability. Figure 8(right) illustrates a lattice as a family of grids.

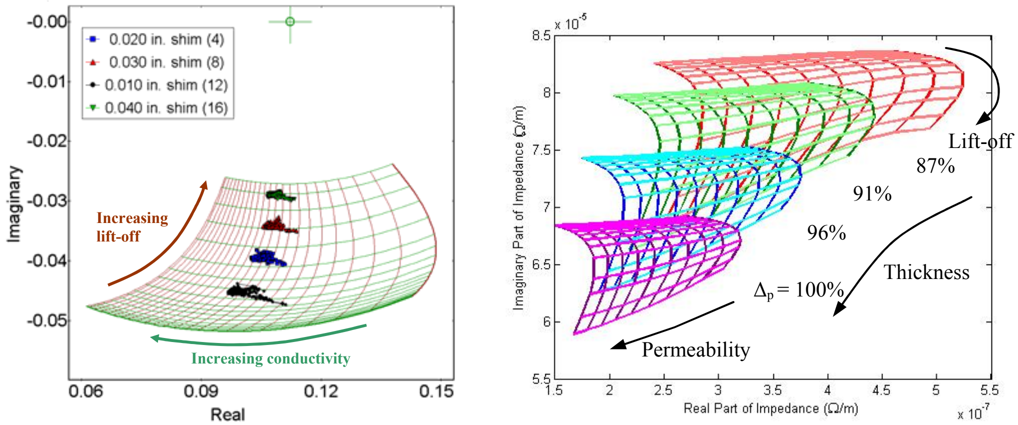

Figure 8. Representative measurement grid (left) and lattice (right) [6].

The ability to model the responses for the MWM-Arrays accurately significantly reduces calibration and scanner fixture requirements. For example, in some situations an "air calibration" can be used, permitting measurement of a component's absolute magnetic permeability or electrical conductivity without calibration reference standards. In-place recalibration and calibration verification are possible with these absolute-property sensors. Furthermore, the lift-off (proximity to the steel pipe wall surface) of each sense element is measured independently, which inherently compensates for variations in barrier coating thickness and the scanning fixture does not need to hold the sensor array at a fixed distance from the pipe wall surface.

Early in the project several types of simulations were performed in order to refine the sensor designs to accommodate the relatively thick coatings of interest for pipeline inspections. As an initial assessment of the sensitivity of the sensors, measurement lattices were generated for several situations. These lattices can be visualized as a series of measurement grids where three (or more) unknowns are to be determined. Good sensitivity is generally reflected by open grids having a large space between the grid lines. For example, Figure 9 (left) shows the simplified layer geometry for determining the properties of the weather jacket. The unknowns to be determined are the sensor proximity to the jacket (lift-off) as well as the conductivity and thickness of the jacket. Representative lattices suitable for aluminum alloy weather jackets are shown in Figure 10. The sensor response varies with the excitation frequency and, by using two or more measurement frequencies, the conductivity and the thickness of the jacket can be determined.

Once the properties of the weather jacket have been established, low frequency measurements can be used to determine the steel pipeline condition. Figure 9 (right) shows the simplified layer geometry including the weather jacket and the steel pipeline. Assuming that higher frequency measurements were performed to determine the weather jacket conductivity and thickness as well as the lift-off, this information is then incorporated into the measurement grid lattices for determining the thickness of the insulation and the presence of corrosion in the pipeline. Representative measurement grid lattices for the determining the relative permeability of the pipeline, the thickness of the pipeline, and the insulation thickness are shown in Figure 11 for $\lambda/4$ = 0.5-in. and in Figure 12 for $\lambda/4$ = 5.0-in. The low frequencies, on the order of 10-100 Hz are required to see through the outer weather jacket and through the pipeline itself. These simulations indicate that the shorter spatial wavelengths will be able to see through moderate coating thickness less than approximately 1-in., but larger dimensions such as $\lambda/4$ = 5.0-in., are required for inspection through thicker insulating layers.

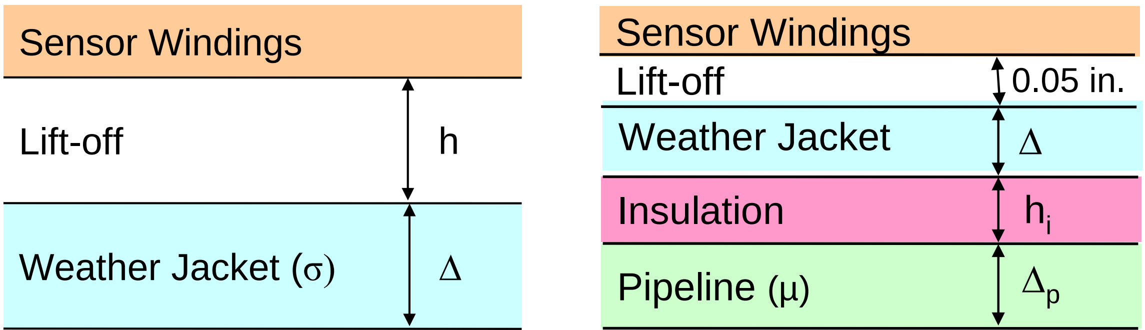

Figure 9. (Left) Simplified geometry for measurements to determine weather jacket properties. (Right) Representative layered geometry for an insulated pipeline including a weather jacket.

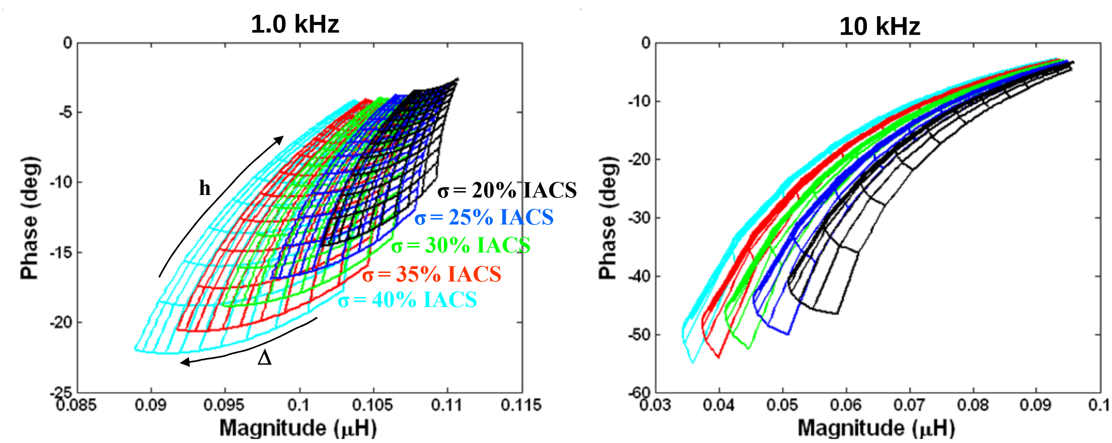

Figure 10. Conductivity/thickness/lift-off measurement grid lattices at two frequencies for $\lambda/4$= 0.13-in. and relatively high values for the electrical conductivity. The lift-off was varied from 0.01 to 0.12-in. and the Δ was varied from 0.05 to 0.15-in.

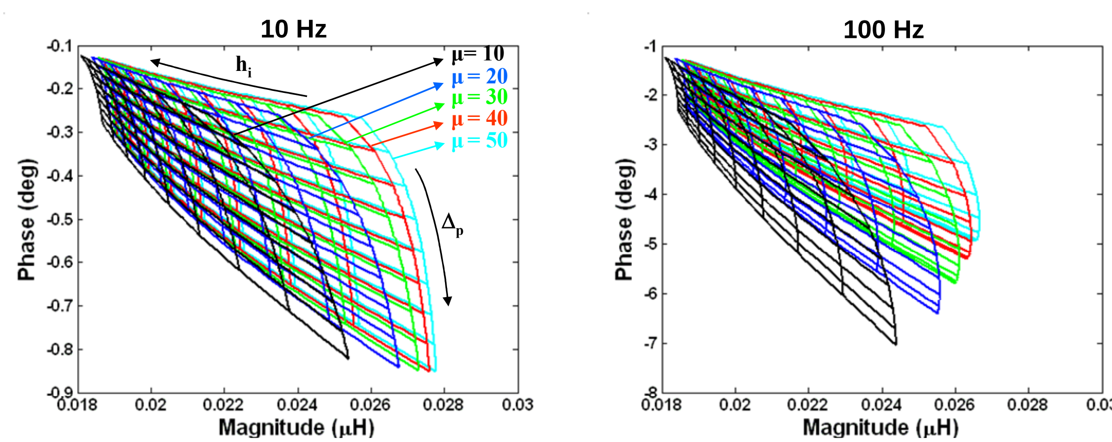

Figure 11. Pipeline-permeability/pipeline-thickness/insulation-thickness lattices for $\lambda/4$=0.5-in. The pipeline thickness Δ_p varied from 0.1 to 0.5-in. and the insulation thickness (h_i) varied from 0.2 to 1.0-in.

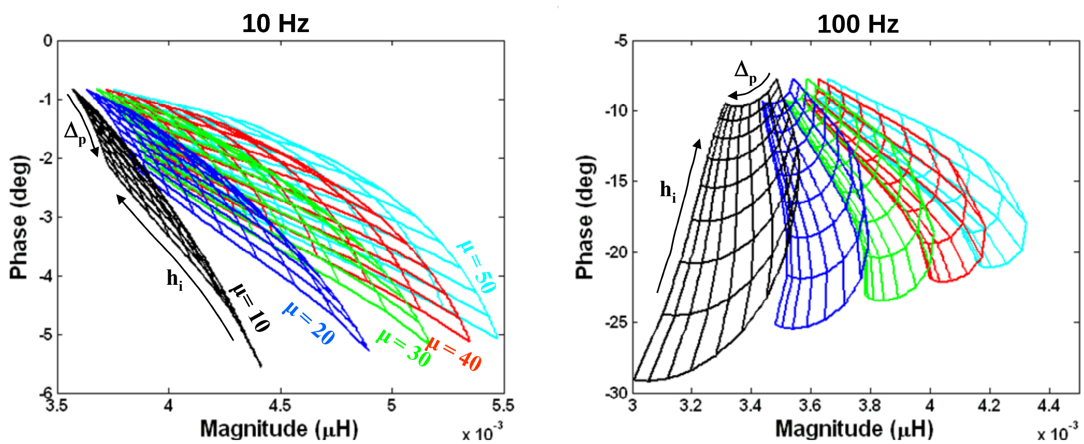

Figure 12. Pipeline-permeability/pipeline-thickness/insulation-thickness lattices for $\lambda/4$=5.0-in. The pipeline thickness Δ_p varied from 0.1 to 0.5-in. and the insulation thickness (h_i) varied from 1.0 to 5.0-in.

6.3 Scanning fixtures

In the effort to provide field support equipment for the scanning arrays, several types of scanning fixtures were investigated. The first type of fixture is shown in Figure 13 and is suitable for use with small MWM-Arrays, such as the FA28 or FA24, for damage imaging through very thin or thin coatings. The sensor array is wrapped around a rigid plastic and foam support layer and positioned underneath the probe electronics. A position encoder is used to record the array position during a scan and, depending upon the configuration, one or more wheels are used to hold the sensor array near the test material surface.

A second type of fixture is shown in Figure 14. This initial prototype scanner fixture has a linear position encoder at the front and two support wheels in the back. The plastic sheet is used to hold the sensor in place during the sensor and attaches to the scanner fixture on each side. This sheet replaces the foam and rigid backing used for previous measurements on the flat plate specimens and provides some flexibility for scanning pipelines having different sizes. This particular scanner was designed to accommodate approximately 6-in. diameter pipe.

Figure 13. Photographs of a single-sided scanner for use with an FA24 and smaller MWM-Arrays.

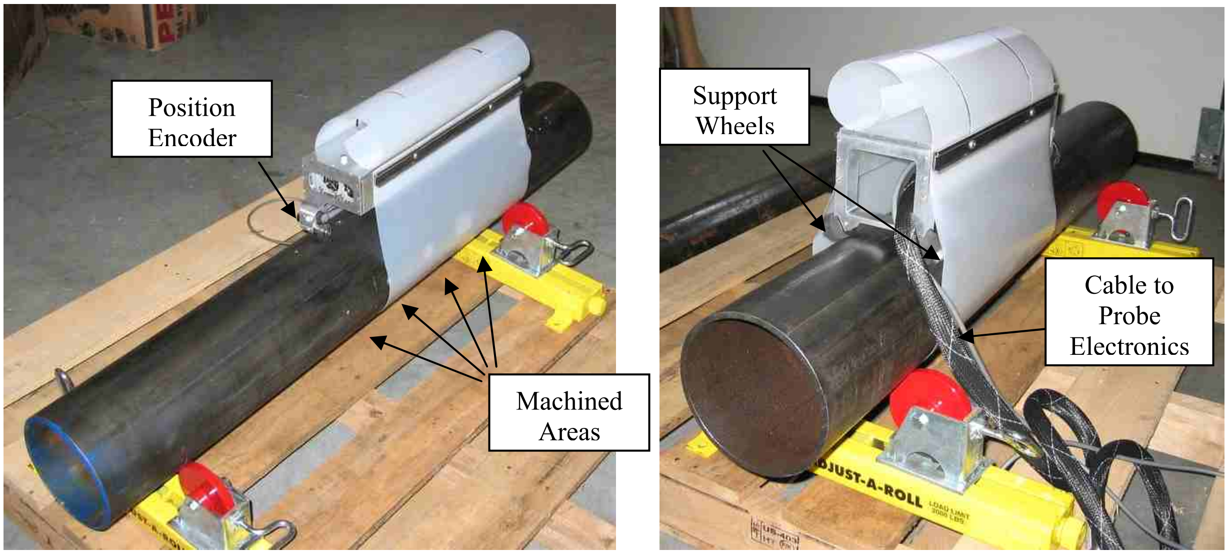

Figure 14. Photographs of a prototype fixture for external scanning of steel pipes.

Based on initial measurements on coated riser sections, several modifications were made to the prototype scanning fixture. Figure 15 shows photographs of the next generation wrap-around scanning fixture. This scanner fixture has four wheels to improve stability during scans on a pipeline. A plastic sheet is used as a back support to hold the sensor in place during the scan and attaches to the scanner fixture with a rigid clamp on one side and a ratcheting clamp on the top. The sheet passes over a tensioning bar to help hold the sensor array against the pipe. A foam layer is placed between the sensor array and the plastic sheet to provide some compliance. The primary mechanism to accommodate coating thickness variations are the linear springs placed at the top of the fixture. The probe electronics fit inside the fixture and a linear position encoder is also placed at the side of the fixture. This fixture accommodates a minimum pipeline diameter of 6-in. and coating thickness of 0.5-in. to 2.0-in.

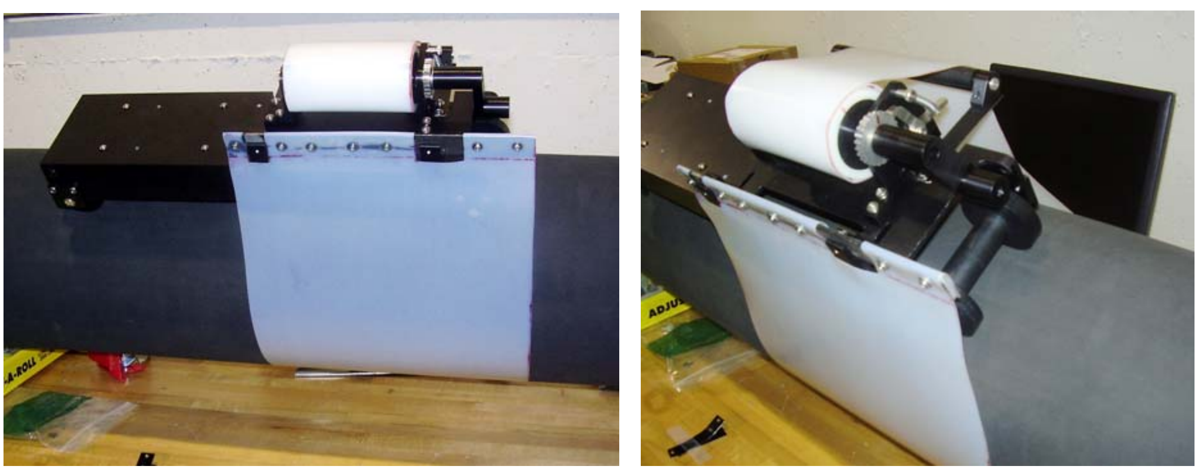

Figure 15. Photographs of the next generation wrap-around scanning fixture.

To improve the usability in the field a smaller scanner for hand-held, local inspections was also fabricated. This scanner is aimed at using smaller VWA arrays, such as the VWA003, that can be held and placed against the pipeline easily. There are two configurations of interest. The first configuration is an open-faced design; a prototype is shown in Figure 16. Similar to the wrap-around design, the sensor array extends out from the side of the probe electronics and a position encoder is placed on the small fixture holding the probe electronics. The sensor array is held in place with a foam backing. In this current embodiment, two hands are required for scanning and there can be variability in holding the sensor array against the insulation surface. However, this is a more compact inspection tool as well. The second configuration has the sensor array wrapped around a support fixture and placed underneath the probe electronics. This would make scanner easier to use with a single hand, but requires careful consideration of the effect of the material used on the back side of the sensor array; since the sensor array is designed to inspect through thick layers of insulation, without shielding, it is also sensitive to the presence of conducting and/or magnetic materials (such as the probe electronics) behind the sensor array. The first configuration was pursued since it does not have the complications associated with the shielding layer.

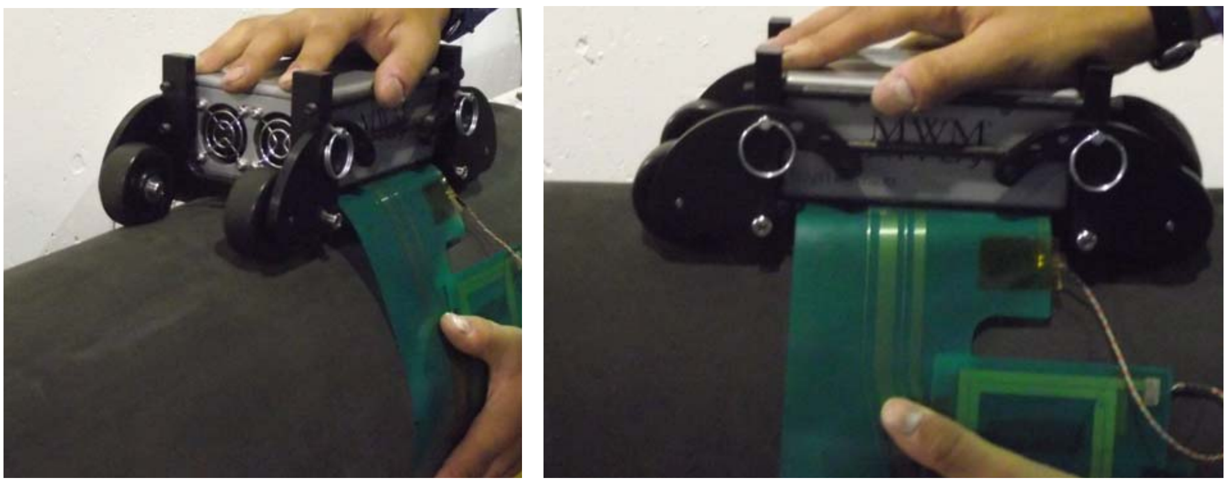

Figure 16. First generation prototype hand-held scanner.

6.4 Demonstration Results

6.4.1 Near-Surface (External) Corrosion Imaging

High frequency measurements were performed on a variety of samples. For near-surface damage inspections with insulating barrier coatings, high frequency magnetic fields readily penetrate the coating and respond to the condition of the underlying steel pipe wall. Initial and baseline measurements were performed on flat steel plates as new sensor arrays became available. This was followed by laboratory testing on a pipe section with several machined areas of material loss for a range of coating thicknesses. Measurements were also performed on coated riser sections with engineered regions of material loss underneath the coating.

6.4.1.1 Initial measurements on flat plates

Numerous measurements were performed on flat plates having machined areas of material loss. These measurements demonstrated the basic capability of the MWM-Arrays and measurement grid methods to independently measure the material condition (magnetic relative permeability of the steel) and lift-off (sense element proximity to the steel surface). These measurements also helped to establish the accuracy of the models for each sensor and contributed to procedure refinements to improve the material loss estimates.

The plates were machined from 4340 steel and had dimensions of 12-in. by 12-in. by 0.125-in. In several of these plates, five regions were machined on one side of the plate to represent areas of material loss. The dimensions of these regions are listed in Table 2. Figure 17 shows a photograph of the machined steel plates. By stacking the plates, with and without machined flaw regions and with different sides closest to the sensor array, variety of flaw configurations and thicker materials could be simulated.

Table 2. List of flaw dimensions for the flat plate specimen and corresponding sense element channels.

Flaw Number	Length (in.)	Width (in.)	Depth (in.)	Channel (through flaw center)
1	1.0	0.5	0.050	35
2	2.0	0.5	0.075	28
3	3.0	1.0	0.100	20
4	2.0	0.5	0.050	12
5	1.0	0.5	0.025	3

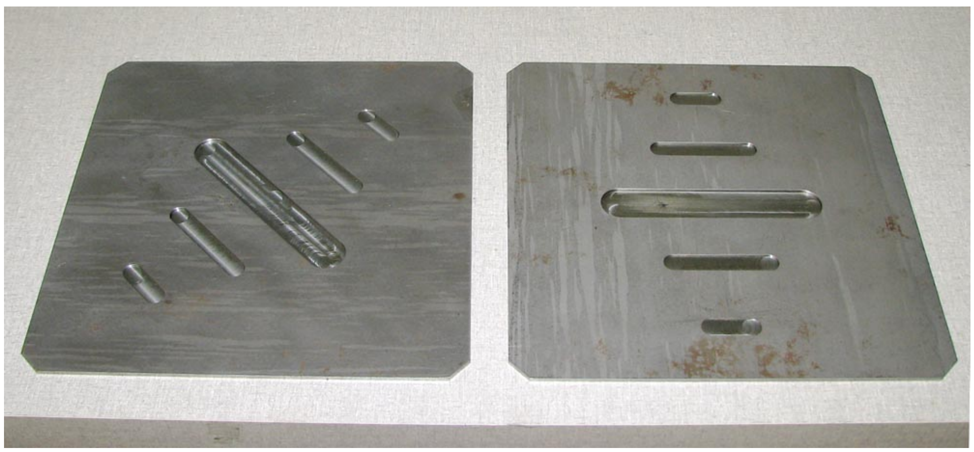

Figure 17. Photograph of flat machined steel plates for simulated corrosion loss.

Baseline demonstration measurements for simulated material loss were performed using JENTEK's medium-size FA122 MWM-Array sensor and a machined steel plate. Figure 18(left) shows the FA122 on a steel plate. The FA122 has a linear array of sense elements and a drive winding microfabricated onto a flexible insulating substrate. This array has thirty-seven 6.35 mm (0.25-in.) square sense elements and a scan width of approximately 9.25 in. A linear position encoder attached to the probe electronics provides the array position during the scan. Figure 18(right) shows a flat plate scanning fixture for the FA122, along with the impedance measurement instrumentation and laptop computer running JENTEK's GridStation software environment for data acquisition and analysis. This fixture provides a rigid support that helps maintain the position of the array relative to the probe electronics and position encoder. A foam layer behind the sensor array helps the sensor array conform to the surface of the material being examined.

Figure 18. (Left) Photograph of the medium-sized FA122 and a machined steel plate. (Right) Photograph of the instrument and FA122 MWM-Array mounted to a scanning fixture. Note that the FA122 is underneath the plastic scanner fixture.

Measurements were performed with several different thicknesses of insulating shims and paper to simulate coating or insulation thicknesses up to 12.7 mm (0.500-in.). A second plate was placed behind the machined plate so that the total steel thickness was 6.35 mm (0.25-in.) in the unflawed areas. Figure 19 shows a series of lift-off images as the simulated coating thickness is varied for a high frequency excitation of 631 kHz. The color scale was adjusted in each image to highlight the presence of the flaw regions. The larger flaws are apparent even for the larger coating thicknesses, but the smaller flaw regions approach the background signal variation for thicker coatings. This suggests that the sensitivity of a given sensor to a given flaw size (area and depth) will decrease as the coating thickness increases; however selection of other sensor designs, as described below, can offer improved sensitivity for thicker coating layers. The color variations at the sides of the images are edge effects as the sensor array moves over the edges of the steel plate. These effects are more pronounced for the higher coating thicknesses as the sensor magnetic fields responds to a large area.

Note that the left and bottom scales of the images of Figure 19 are expressed in inches while the scale on the right of the images indicates the sensor element channel number. In this case the sensor array was calibrated using a measurement in air and a measurement with a shunt sensor in which the sense elements are shorted. This is a robust method of calibration since it does not rely on knowledge of a reference material, but it requires having a shunt that is essentially identical to the sensor array. The striping in the images for the larger coating thicknesses is associated with a poor calibration for channel 22. The image quality generally improves for larger samples, where edge effects are not present.

Figure 20 shows the 631 kHz measurement grid and data used for the multivariate inverse methods. The grid lines reflect the nonlinear sensor response variation with magnetic permeability (μ) and sensor lift-off (h) for an infinite half-space of material. The measurement grids inherently account for the nonlinearity in the sensor response. In this case, an electrical conductivity of 3.75% IACS was assumed for the grid and which is typical for steel. Also plotted on the grid are data points for channel 7, which is between the two lower machined sections on the sample, for measurement points when the sensor array is over the steel plate (data points 300-600). These data points essentially follow a line of constant permeability as the lift-off or coating thickness is varied, which validates the models used for the sensor array.

Figure 21 shows B-scan plots across each of the flaws indicated in the scan images. Table 2 lists both the flaw dimensions as well as the sense element channel number corresponding to each flaw. Distant from the flaws, the change in lift-off reflects the different coating thicknesses and some channel-to-channel variability, which increases with coating thickness. However, in each case, the lift-off increases, often substantially, over the machined areas, which is consistent with these being areas of near-surface material loss.

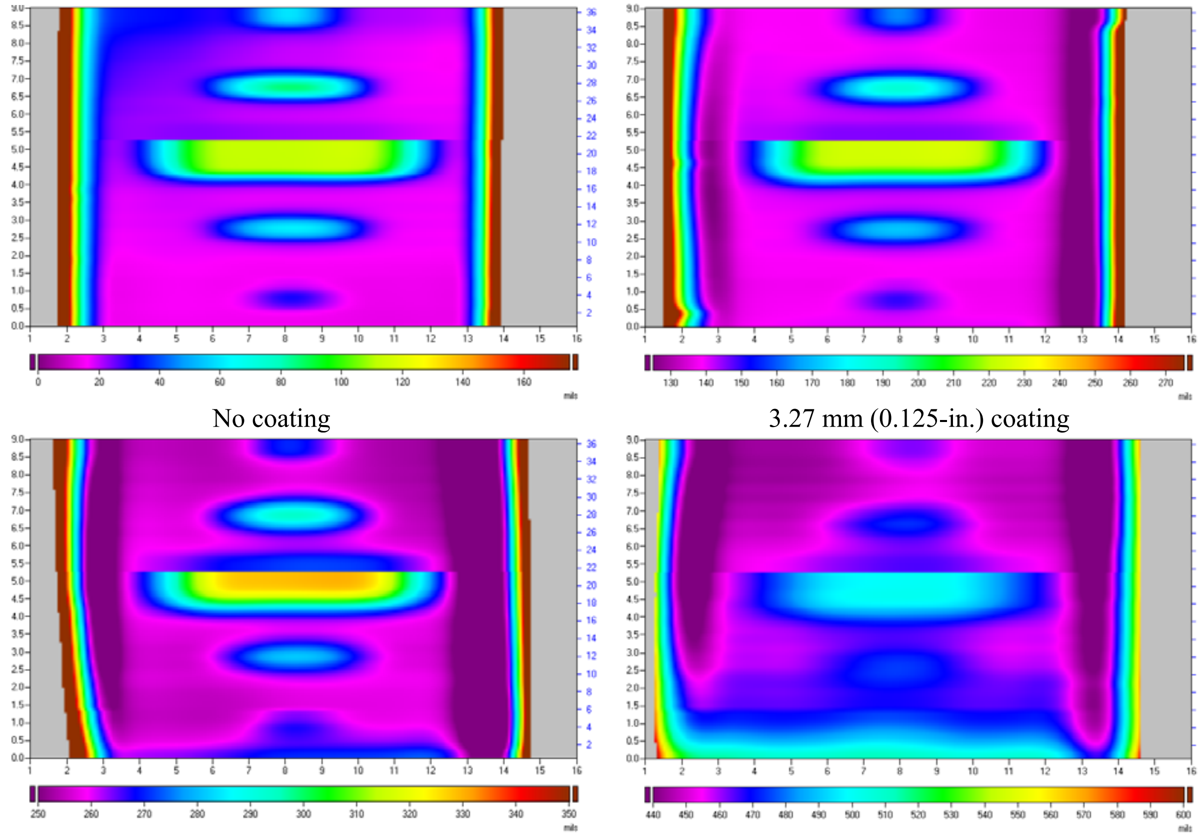

Figure 19. Images obtained from a series of scans with the FA122 over the machined steel plate and with different simulation coating thicknesses.

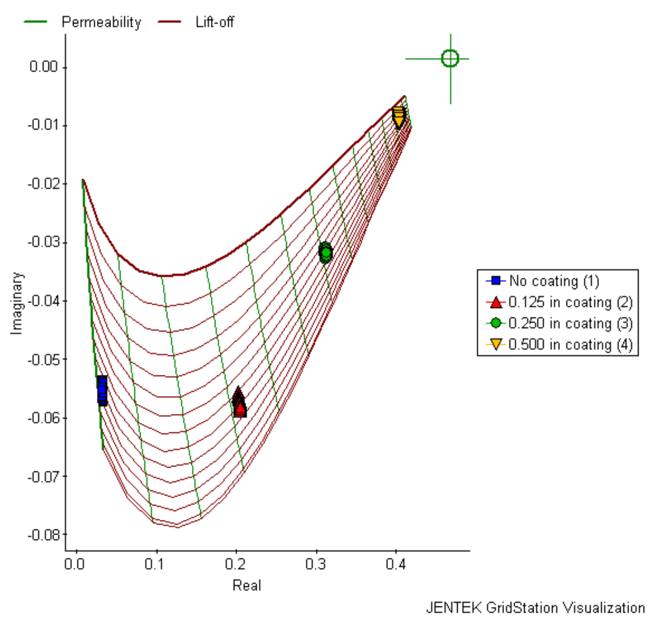

Figure 20. Measurement grid and data for an FA122 channel over the machined steel plate (from channel 7, which is between the machined regions) for several varied coating thicknesses.

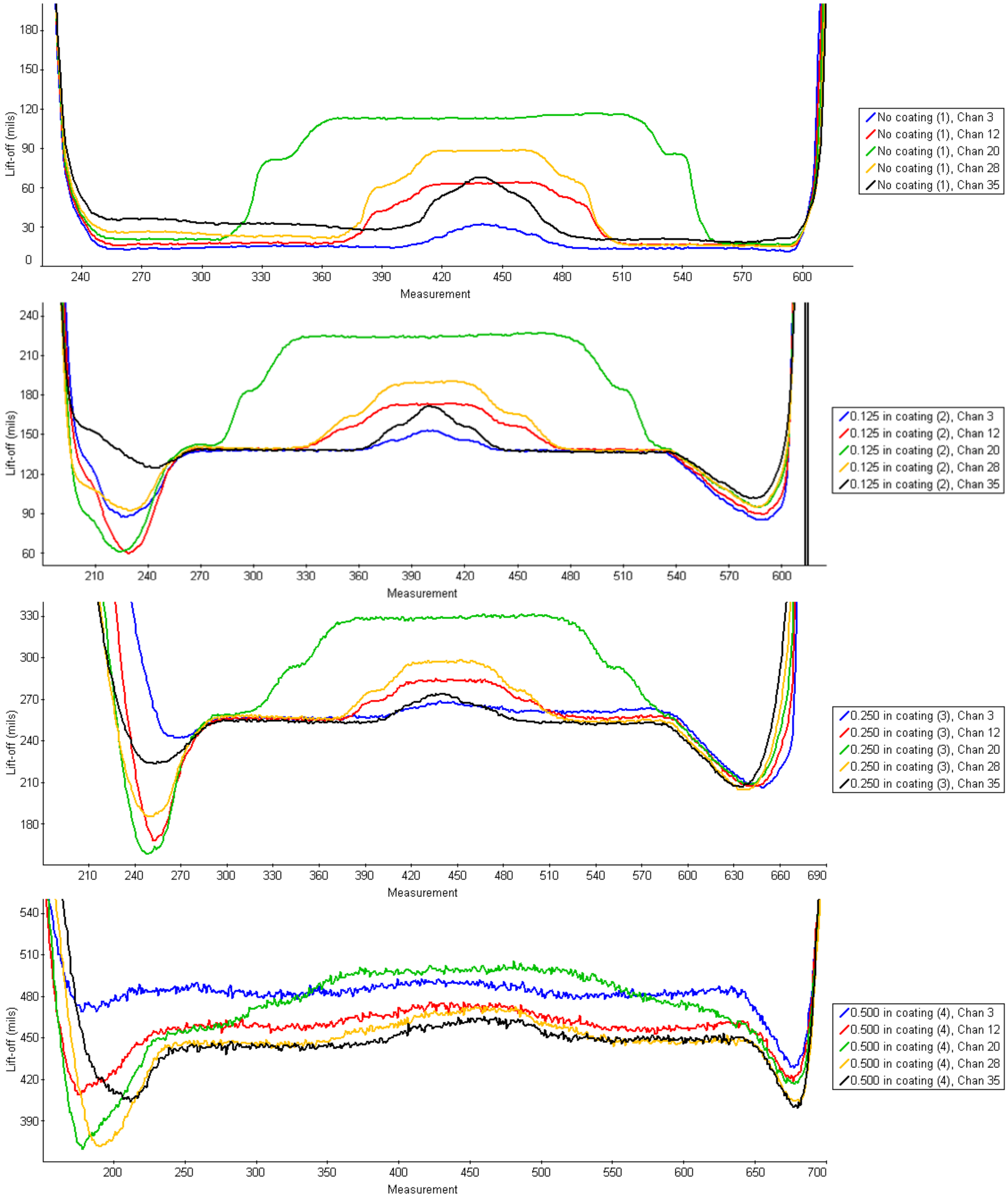

Figure 21. B-scans for comparing the FA122 responses for no coating and several insulating layer thicknesses to emulate varied coating thicknesses.

To illustrate the baseline performance of this sensor, Figure 22 shows plots of the nominal coating thickness (left) and depth of the material loss regions (right) as the coating thickness is varied. For the nominal coating thickness, there is a slight lift-off of approximately 0.010 to 0.015 inches for the small coating thicknesses due to the geometry of the sensor and the presence of protective layers placed on the sensor surface. For large coating thicknesses, there is a slight underestimate of the coating thickness; this estimate could be improved by selecting a better value for the electrical conductivity of the steel or by using multiple frequency measurements to determine the electrical conductivity simultaneously with the permeability and lift-off. Figure 22(left) also shows a plot of the measured distance obtained with a sensor model assuming a periodic geometry, which leads to a substantial underestimate of the coating thickness. This indicates the value of using the correct model in the data inversion as it makes the measurements more reliable.

For the depths of the material loss regions shown Figure 22(right), the measured values tend to underestimate the depth because the geometry of the material loss is not considered in the basic measurement grids; the basic measurement grids assumed planar material layers. This suggests that a procedure for improving the estimates of the material loss would include (1) detecting regions of material loss and roughly determining its spatial extent and (2) using a flaw-based measurement grid that incorporates this spatial information and measurement response information to obtain the depth estimate.

As a simple example of such as measurement procedure, consider the hybrid measurement grids of Figure 23, which relate the actual flaw depth to the effective lift-off change that would be expected from a planar material layer model. These responses were obtained from a three-dimensional boundary element model for the FA122 geometry assuming a steel substrate with long flaws that were 0.5 or 1.0 inches wide. The response of a sense element over the center of the flaw is indicated. As expected, the effective lift-off tends to underestimate the actual flaw depth, which the underestimate being more significant at larger coating thicknesses. However, compensation for the coating thickness and flaw geometry is accomplished by passing the measured effective lift-off and coating thickness through the hybrid measurement grids to obtain corrected material loss measurements. The result of this process, shown in Figure 24, indicates that this type of correction yields reasonable material loss values.

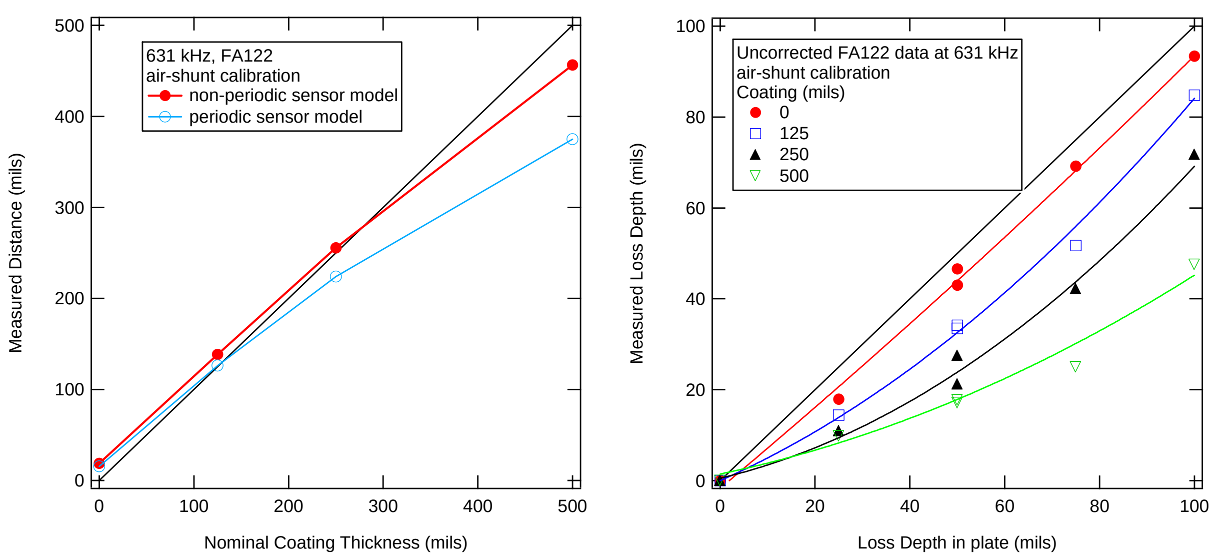

Figure 22. (Left) Nominal coating thickness measured with the FA122 at locations distant from the machined flaw regions. (Right) Nominal depth for each of the machined flaw regions using a uniform layer model that did not correct for the area of the flaw.

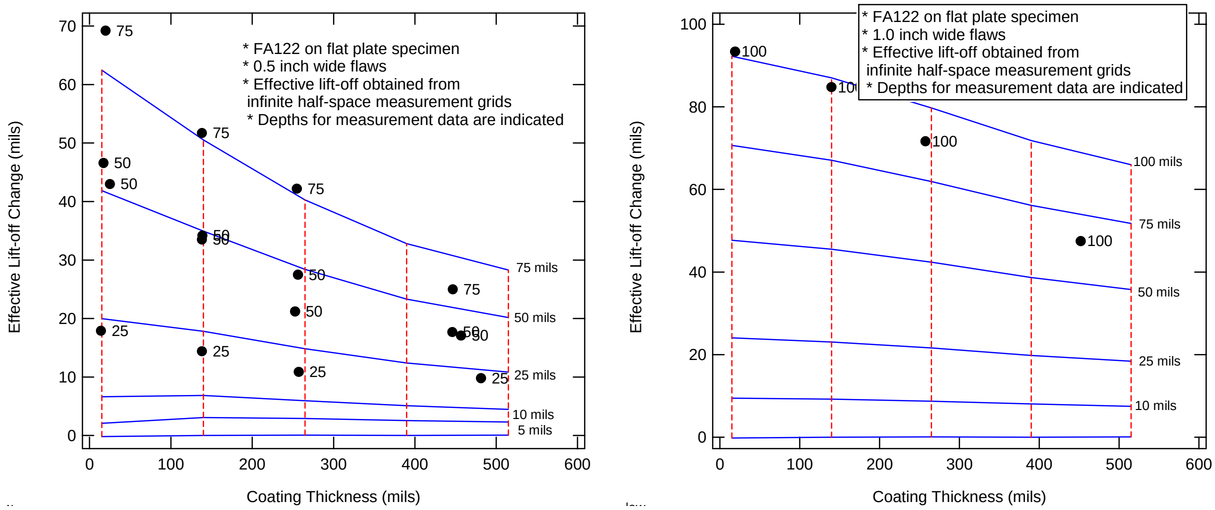

Figure 23. Hybrid measurement grids relating the flaw depth and coating thickness to the effective lift-off change obtained from a planar model. (Left): For 0.5-in. wide flaws. (Right): For 1.0-in. wide flaws.

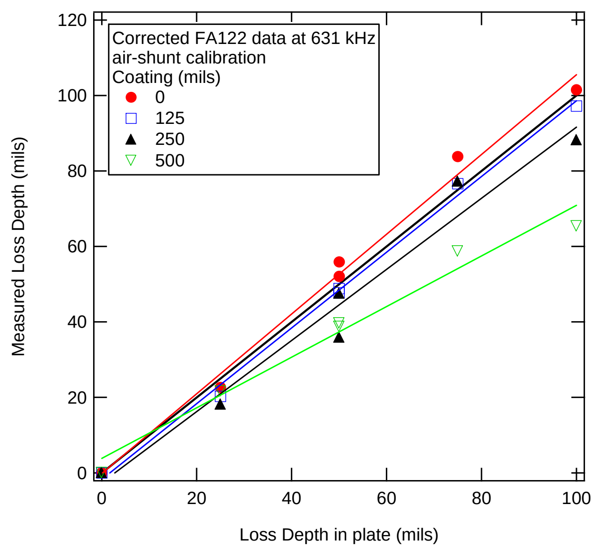

Figure 24. Plot of the depth for each of the machined flaw regions using the hybrid measurement grids of Figure 23.

6.4.1.2 Measurements on laboratory pipe sections

The bulk of the laboratory testing and demonstrations on curved materials was performed on a steel pipe section. This pipe section was 4 ft long, with an outer diameter of 6.625-in. and a wall thickness of 0.28-in. A series of flaws were machined into the outside surface to represent external material loss. This pipe section had four rows of flaws located every 90^{o} around the circumference of the pipe. The flaws were machined to depths corresponding to 5%, 10%, 25%, and 50% material loss. The nominal flaw sizes are 0.25, 0.5, 1.0 and 2.0 inches in diameter, but the curvature of the surface and the shallow flaw depth resulted in a rectangular shape for the shallower and larger flaws. The flaws are positioned near the center of the pipe in order to provide some room for moving a sensor array and scanning fixture along the pipe. These depths were chosen since they are appropriate for repair/replace maintenance decisions for pipelines.

Figure 25 shows a photograph of this pipe section along with a small-size FA24. This pipe section is loaded on top of rollers; this allows the section to be rotated so that additional scans could be made and an image of the surface topology spanning the circumference of the pipe section can be obtained. Two layers of 0.010-in. thick plastic sheets were wrapped around the pipe section to simulate the presence of a thin (0.020-in. thick) insulating coating. During the measurements, the sensor array was moved along the top surface of the pipe section. For these measurements, an air-shunt calibration was performed. This type of calibration uses a measurement in air and a measurement with a shunt sensor in which the sense elements are shorted. This is a robust method of calibration since it does not rely on knowledge of a reference material, but it requires having a shunt that is essentially identical to the sensor array. The frequencies used were 10, 100, and 631 kHz.

Figure 26 shows property images obtained for the FA24 MWM-Array at a frequency of 100 kHz. The left and bottom axes are expressed in inches. The regions of material loss are clearly visible as areas of increased lift-off as the effective distance between the sensor array and the steel surface increases. The shapes of the regions are also appropriate; for the shallower and larger flaws the regions are rectangular in shape. The flaw regions are also apparent in the relative permeability image. Since the magnetic permeability can vary with material condition, such as residual stress, this may reflect property changes associated with the flaw machining process. Note that a scan was made over each of the four rows of material loss; scans were not made over the intermediate regions that did not contain flaws. Figure 27 shows B-scan (individual sense element response) plots of the lift-off response for a sense element that passed over the center of each region. The lift-off varies with material loss as expected. These plots show that each of the material loss regions is detected.

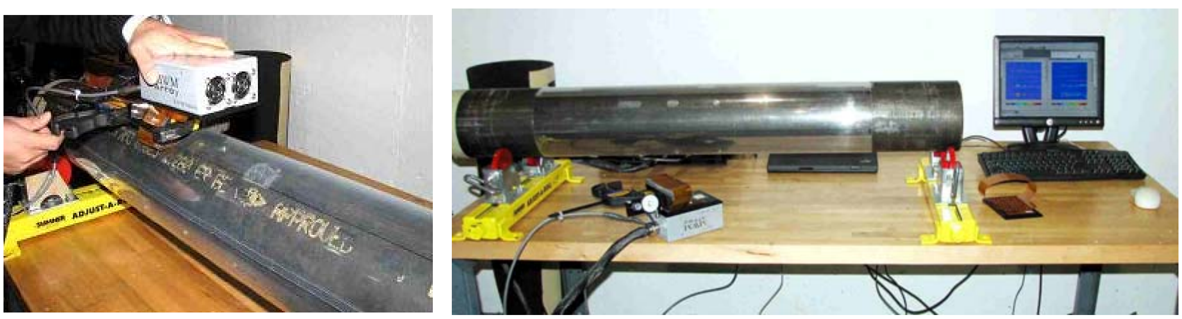

Figure 25. (Left) Photograph of an FA24 MWM-Array being scanned over a pipe section with a thin coating. (Right) Photograph of the pipe section with machine loss and on a test table.

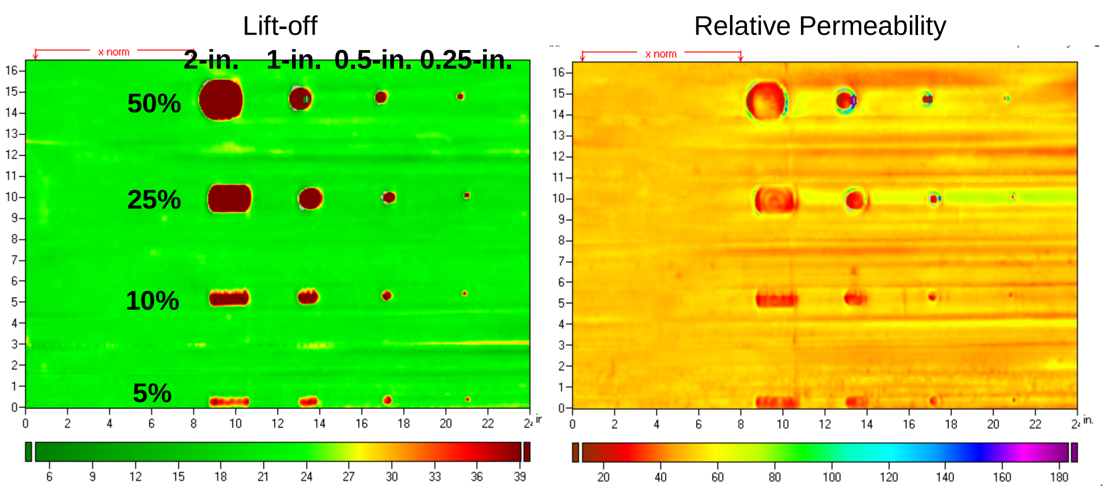

Figure 26. C-scan lift-off (left) and permeability (right) images obtained from a series of scans with an FA24 MWM-Array at 100 kHz for the pipe section having flaws machined in the outside surface and a thin (0.020-in.) plastic coating.

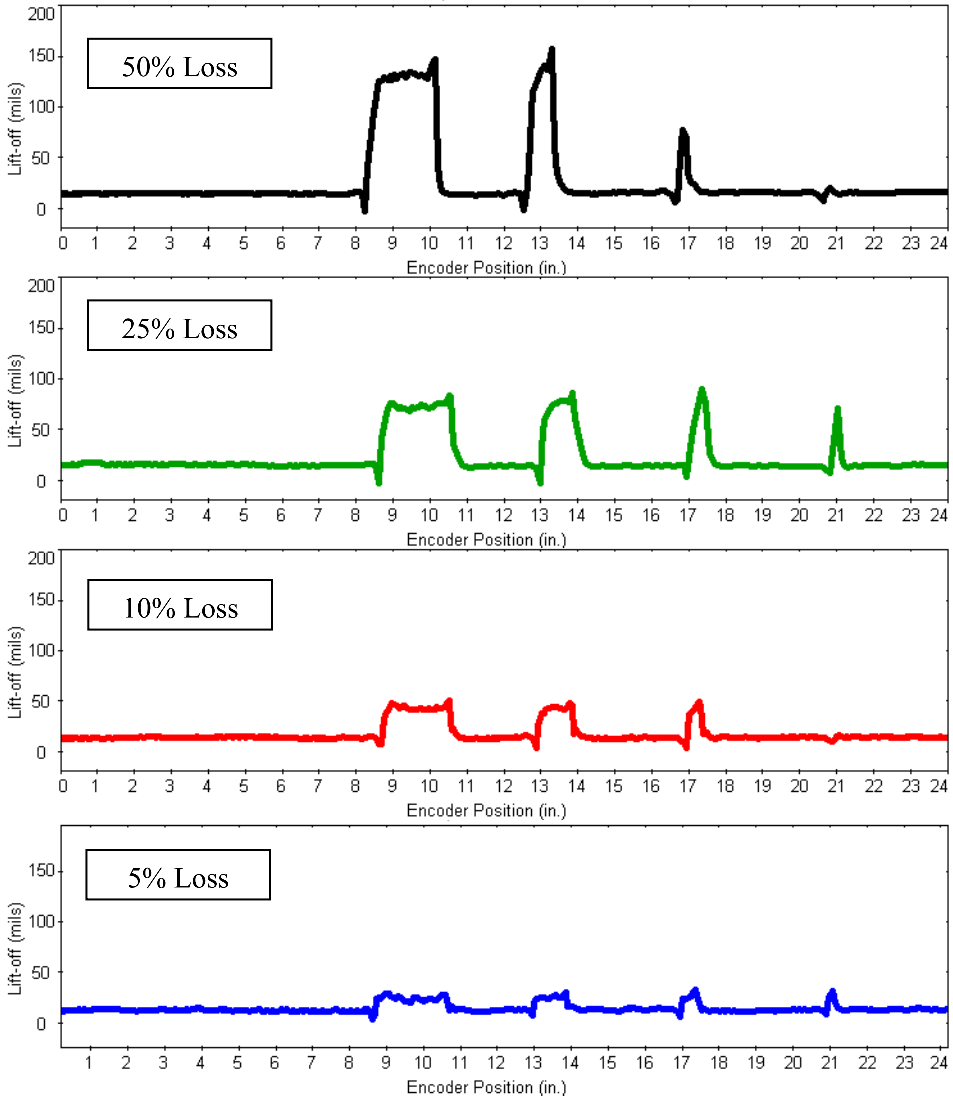

Figure 27. B-scan lift-off plots for an FA24 sense element with a 0.020-in. thick coating.

Similar measurements were performed with the larger VWA001 sensor array scanned over the external pipe section. For the measurements with the VWA001, a 0.5-in. thick layer of Neoprene was wrapped around the surface to represent a medium thickness coating. Figure 28 shows the pipe section with Neoprene and the scanning fixture with the sensor array in place. For these measurements a 1-inch gap was used between the linear array of sense elements and the drive winding. The scanner fixture has a linear position encoder at the front and two support wheels in the back. The plastic sheet is used to hold the sensor in place during the scan and attaches to the scanner fixture on each side. This sheet replaces the foam and rigid backing used for flat-plate measurements and provides some flexibility for scanning pipelines having different sizes.

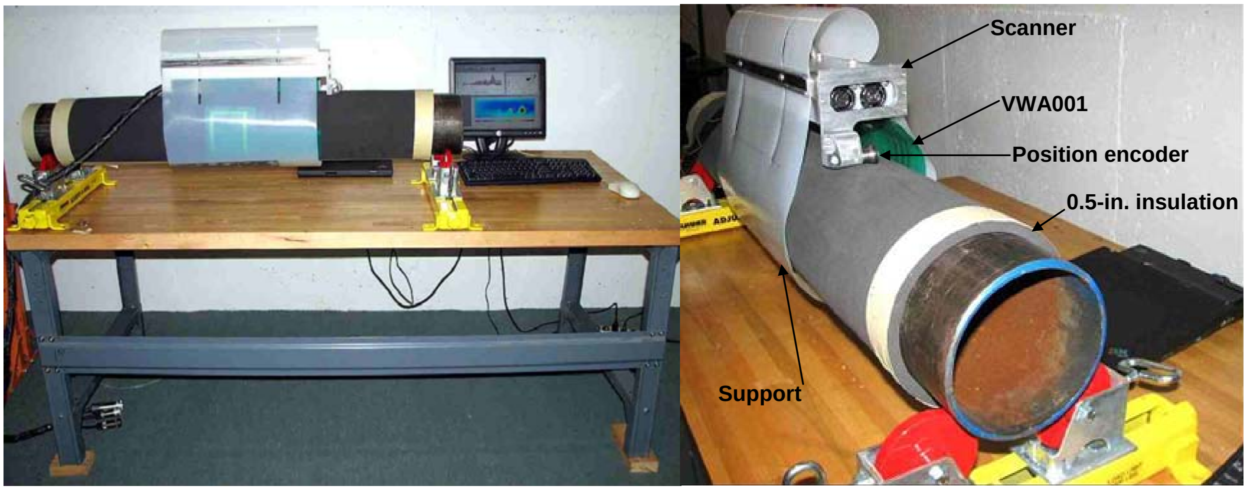

Figure 28. Photographs of the external material loss steel pipe section wrapped with a 0.5-in. layer of Neoprene along with the scanning fixture for the larger sensor arrays. The plastic sheet is attached to both sides of the scanner and holds the VWA001 in place around the pipe section during the scan.

Figure 29 shows lift-off data obtained with the VWA001 over a 0.5-in. coating. Many of the machined areas are visible in this image with the larger diameter and deeper flaws appearing most clearly. This image was created from several scans at different circumferential positions over the surface. The fixture does not appear to hold all of the sense elements in contact with the coating surface and there are background variations in the lift-off associated with how the scanner fixture holds the array in position. Improving the fixture will enhance the imaging capability of the sensor arrays. The B-scan plot can also be used to determine the presence of damage. For example, while the 0.5-in. material loss region is difficult to see in the C-scan image, there is a local increase in lift-off for the sense element channels that went over the flaw.

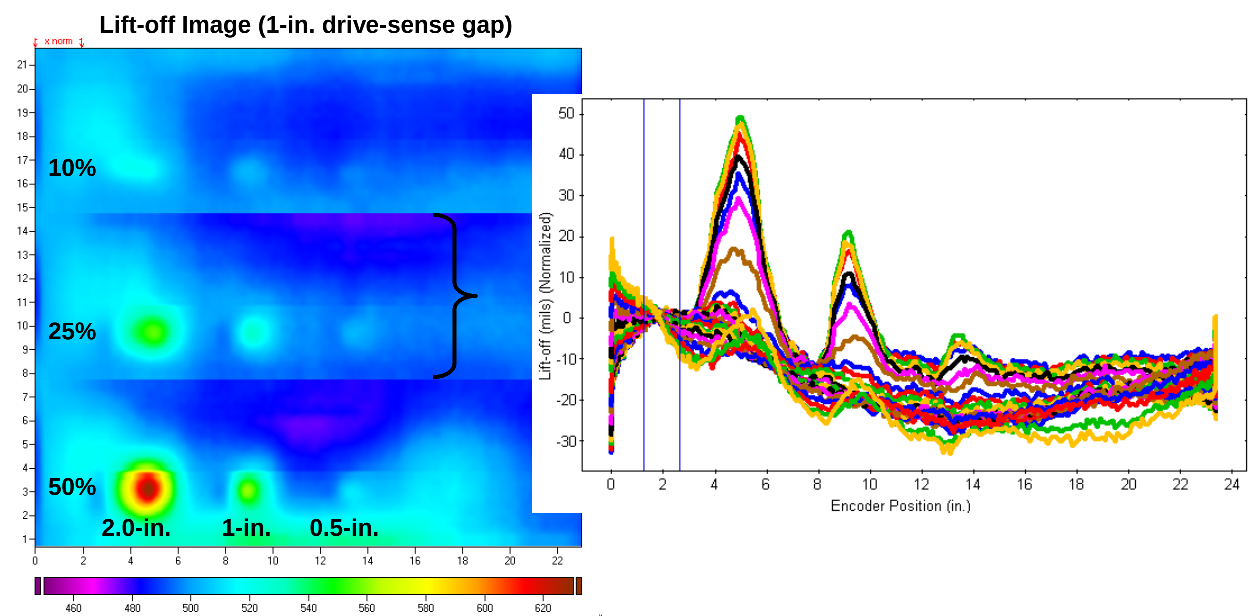

Figure 29. C-scan lift-off image obtained from a scan with the VWA001 at 631 kHz over the 50% material loss flaws for the external material loss pipe section and a 0.5-in. layer of Neoprene.

A series of measurements were performed with the VWA001 to determine the sensitivity to different operating condition parameters. These parameters include the excitation frequency, drive-sense gap spacing, the type of calibration performed, the use of extra signal amplification, and the use of different probe electronics, as well as the different coating thicknesses.

Figure 30 shows a series of lift-off images obtained with the VWA001 and a drive-sense gap of 25.4 mm (1.0-in.) for a range of coating thicknesses. The images show the 25% and 50% material loss regions, with the high spatial resolution images obtained for coating thicknesses of 0.5 and 1.0-in. For larger coating thicknesses the larger flaws are still visible but there is a noticeable degradation of the flaw images. For the 1.75-in. thick coating the sensor array only passed over the 50% material loss regions. For these measurements, two types of calibrations were performed. An air-shunt calibration was performed for the 0.5 and 1.0-in. coating thicknesses since the sense element impedance change between the air value and the proximity of the steel pipe was large compared to the measurement noise. However, for the larger coating thicknesses, a reference calibration was performed where reference measurements were performed on the coated pipe with and without a 0.10-in. shim. This lift-off change led to a shift in the sense element impedance that was distinct from the measurement noise and provided a better alignment of the sensor response with the measurement grids. Although the air-shunt calibration is preferred, since it requires fewer assumptions about the steel and coating properties, the reference calibration is useful when the inspection requires measurements of relatively small impedance changes.

Figure 31 contains plots of the effective lift-off change associated with a single sense element that passed over the centers of the 50% material loss regions. This lift-off change is taken as the difference between the lift-off at each location and an average lift-off obtained for an unflawed region at the beginning of the scan. An 11 point moving average was applied and the peak in the response for the 2-in. diameter flaw at 100 kHz was used to align the measurement scans. The 12.7 mm (0.5-in.) coating data used an air-shunt calibration while the other measurement used a reference calibration. For the moderate thickness coatings (0.5 and 1.0-in. thick), all three material loss regions are visible at the higher frequencies (100 and 631 kHz), but only the two larger loss regions are visible at the lower frequency of 10 kHz. Also there is a visible decrease in the measurement noise (for example, for the 44.5 mm (1.75-in.) thick coating) as the frequency increases. This suggests that the near-surface material loss measurement through insulating coatings should use a relatively high frequency.

Although each of these regions has the same maximum depth of 3.56 mm (0.14-in.), the change in the effective lift-off depends upon the size of the flaw region. Since the peak value for the material loss does not change appreciably with the coating thickness, it appears that the size of the flaw region has a more significant effect than the coating thickness on the measurement response. Models and measurement grids that account for the size of the flaw region can improve the depth estimate. The measured response to each flaw region reflects a combination (or convolution) of the sensor dimensions as well as the flaw dimensions. The width of the material loss is approximately the response width at half the maximum value.

Figure 32 shows the corresponding effective permeability change at 100 kHz. For the smaller diameter flaws the material loss appears as an increase in the relative permeability but for the larger flaw there is an initial decrease followed by a peak in the relative permeability. These lift-off and permeability variations are generally consistent with measurements performed on the riser section samples, which are described in Section 6.4.1.4. As examples, Figure 59 shows the response to an oblong-shaped section of material loss that appeared to be several inches in diameter; the relative permeability change shows both a peak and dip in the response associated with the flaw. Figure 60 shows that the response to a circumferential flaw that was approximately 1-in. wide and 6-in. long appears as a reduction in the permeability. Figure 61 shows that the response to an axial flaw that was approximately 1-in. wide and 9-

in. long appears as an increase in the permeability. In all of the cases, the material loss regions appear as an increase in the lift-off.

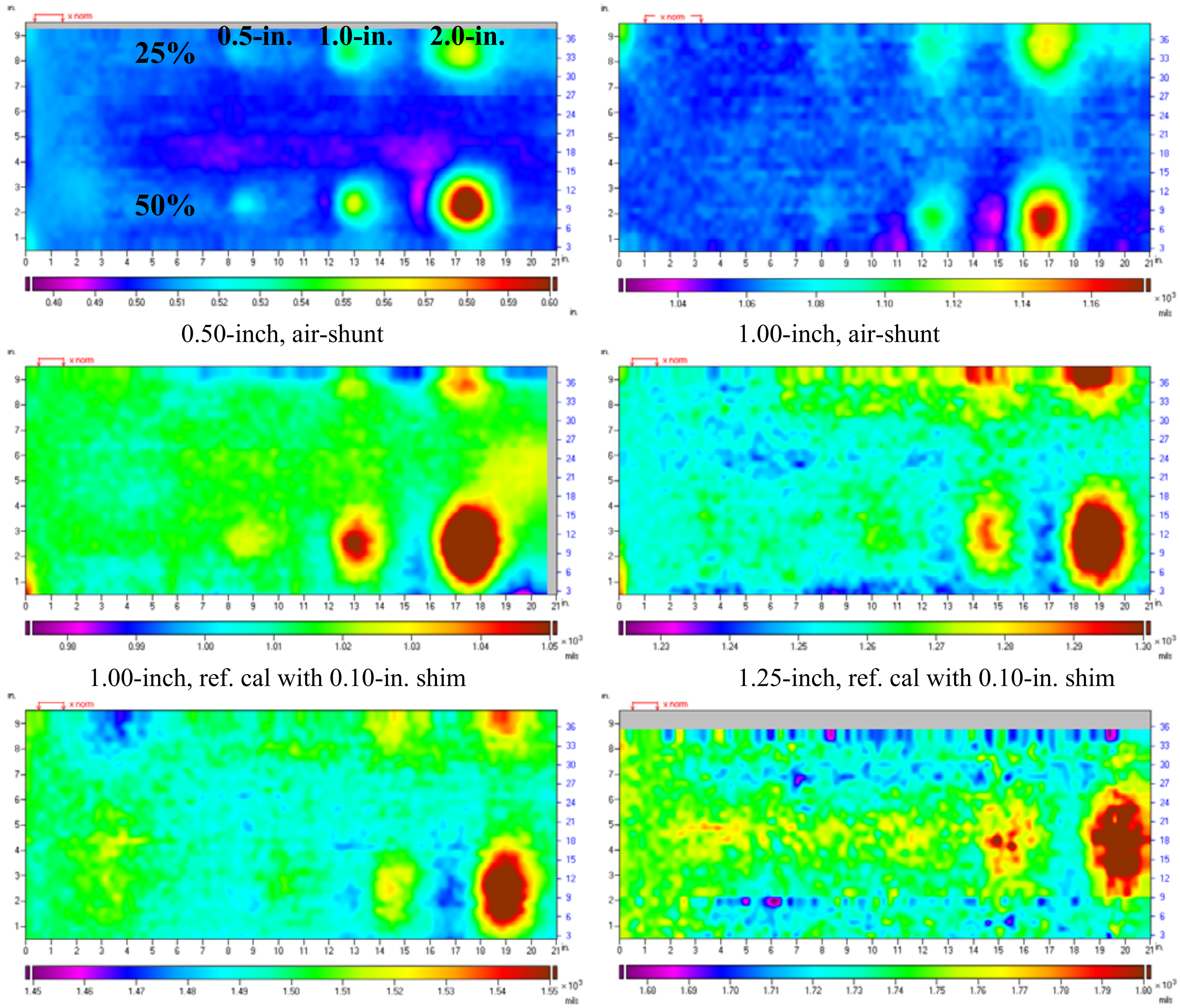

0.50-inch, air-shunt

1.00-inch, air-shunt

1.00-inch, ref. cal with 0.10-in. shim

1.25-inch, ref. cal with 0.10-in. shim

1.50-inch, ref. cal with 0.10-in. shim

1.75-inch, ref. cal with 0.10-in. shim

Figure 30. Effective lift-off images for the steel pipe with manufactured material loss regions using a VWA001 with a 25.4 mm (1.0-in.) drive-sense gap and a frequency of 100 kHz.

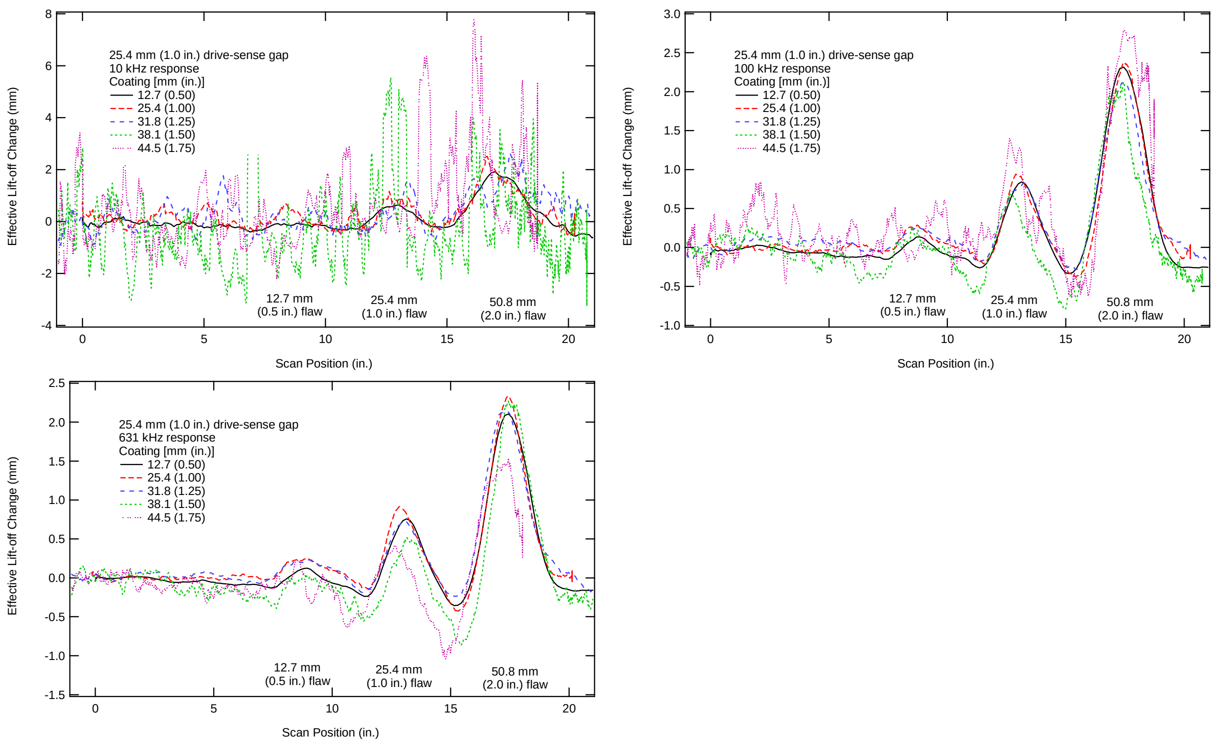

Figure 31. Effective lift-off change plots for the 50% material loss regions for a VWA001 with a 25.4 mm (1.0-in.) drive-sense gap as the coating thickness is varied.

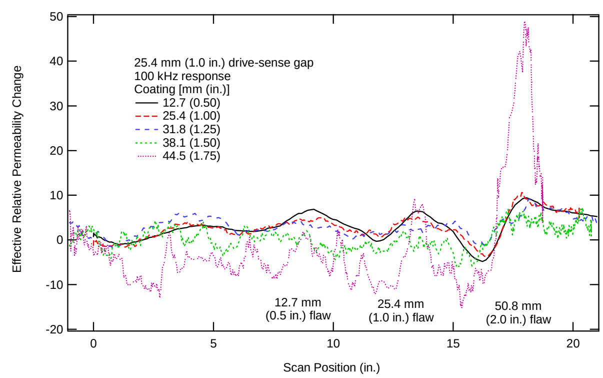

Figure 32. Effective relative permeability change plot for the 50% material loss regions for a VWA001 with a 25.4 mm (1.0-in.) drive-sense gap as the coating thickness is varied and at 100 kHz.

Figure 33 shows a similar series of lift-off images obtained with the VWA001 and a drive-sense gap of 50.8 mm (2.0-in.) for a range of coating thicknesses. The first two images show the 25% and 50% material loss regions for 0.5-in. coating and high spatial resolution images are obtained with both air-shunt and reference calibrations. For larger coating thicknesses the larger flaws are still visible but there is a noticeable degradation of the flaw images. This configuration allowed the 2.0-in. diameter material loss to be imaged with a 2.0-in. thick coating, even though there is a noticeable degradation in image quality for the larger thicknesses. For thicker coatings, such as 2.5-in., the instrument noise was too large to observe the flaws. However, after modifying the instrumentation by inserting an amplifier to increase the drive signal level, the measurement noise was substantially reduced and the larger flaw could be observed.

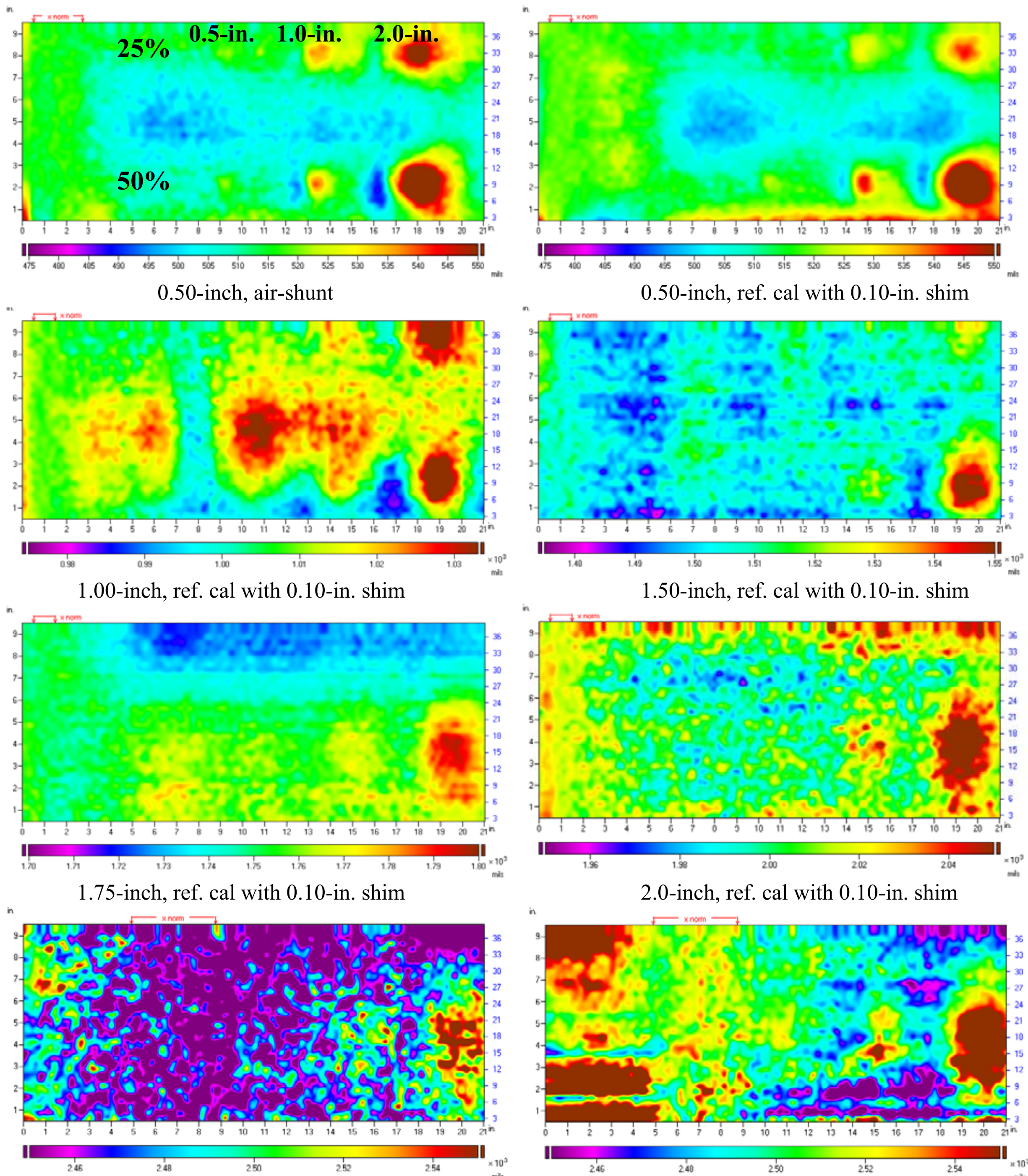

Figure 33. Effective lift-off images for the steel pipe with manufactured material loss regions using a VWA001 with a 50.8 mm (2.0-in.) drive-sense gap and a frequency of 100 kHz.

Figure 34 contains a plot of the effective lift-off change associated with a single sense element that passed over the centers of the 50% material loss regions. The 12.7 mm (0.5-in.) coating data used an air-shunt calibration while the other measurement used a reference calibration. There are peaks in the lift-off change associated with the two larger loss regions; these are similar to the results obtained for the 1.0-in.

drive-sense gap. However, the peak value is substantially smaller for the larger gap. Thus, **increasing the drive-sense gap has two effects: it provides a modest improvement in image resolution to large flaws for large coating thicknesses**, particularly when appropriate amplification is used to compensate for small signal strengths, but **it leads to a decrease in sensitivity of the absolute change in the sensor response for a given flaw.**

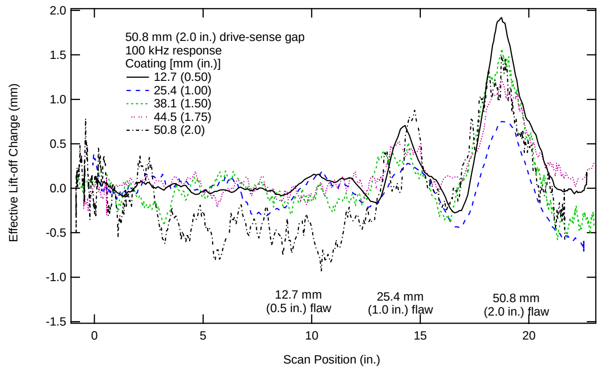

Figure 34. Effective lift-off change plots for the 50% material loss regions for a VWA001 with a 50.8 mm (2.0-in.) drive-sense gap as the coating thickness is varied.

Another option for improving the imaging capability with the large sensor arrays such as the VWA001 is to use probe electronics optimized for lower frequency operation. The use of a drive current amplifier with high-frequency probe electronics improved the response for inspection through thicker coatings. However, if the frequency is limited to less than about 200 kHz, which is reasonable for the inspection of near-surface material loss, then low-frequency probe electronics that incorporates higher amplification settings can be used.

Figure 35 shows lift-off images obtained with the VWA001 and a drive-sense gap of 25.4 mm (1.0-in.) for several coating thicknesses. For the 1.0 and 1.5-in. thick coatings, an air-shunt calibration was performed and several of the material loss areas are clearly visible. Previously, a reference calibration was required with the 1.5-in. coating thickness in order to obtain reliable images; this indicates that the model refinements improved the accuracy of the measurement grids. For the 2.0-in. thick coating, a reference calibration was performed using measurements with and without a 6.35 mm (0.25-in.) thick shim. This image was taken over the 50% material loss flaws and the larger (1.0 and 2.0-in.) diameter flaws are visible.

Figure 36 shows the measurement grid used for processing the 100 kHz data along with some of the measurement data. For the 25.4 mm (1.0-in.) coating the measurement data are in a relatively open region of the grid, which indicates that independent estimates of the permeability and lift-off can be made. In contrast, for the 50.8 mm (2.0-in.) coating the data is near a region of the grid where the grid lines are relatively dense, which indicates that the same measurement noise or unmodeled parasitic effects can have a greater effect on the property estimates. When operating in the regime where the grid lines collapse and are relatively dense, a reference calibration better aligns the sense element responses to the measurement grid and helps reduce the effect of unmodeled parasitics. Alternatively, the sensor geometry can also be altered to improve sensitivity for thick coatings. For example, Figure 37 shows an effective lift-off image for a 50.8 mm (2.0-in.) coating with a 50.8 mm (2.0-in.) drive-sense gap. Compared to Figure 35, for a 50.8 mm (2.0-in.) coating the flaws are more noticeable.

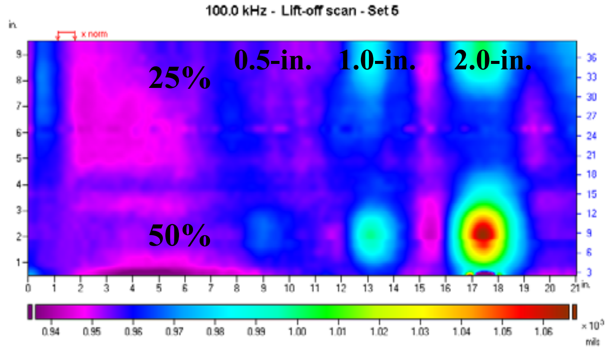

1.00-inch, air-shunt

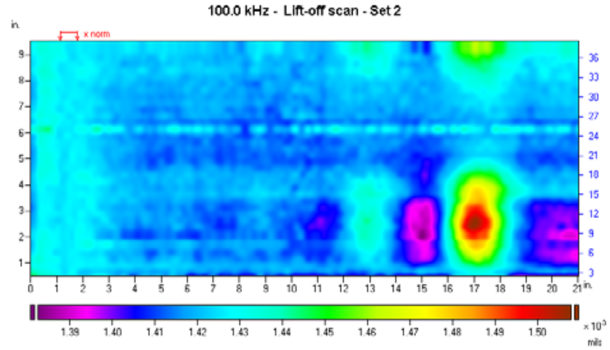

1.50-inch, air-shunt

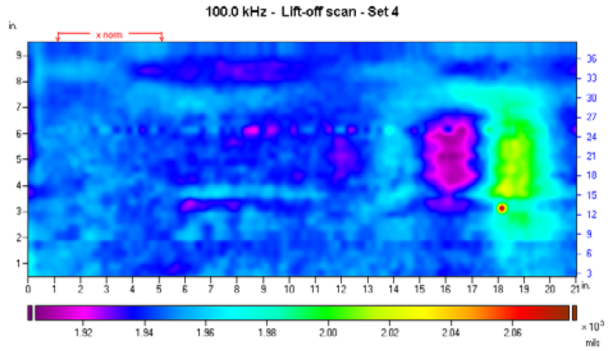

2.00-inch, ref-cal with 0.25-inch shim

Figure 35. Effective lift-off images for the steel pipe with manufactured material loss regions using a VWA001 with a 25.4 mm (1.0-in.) drive-sense gap at 100 kHz and a low-frequency probe.

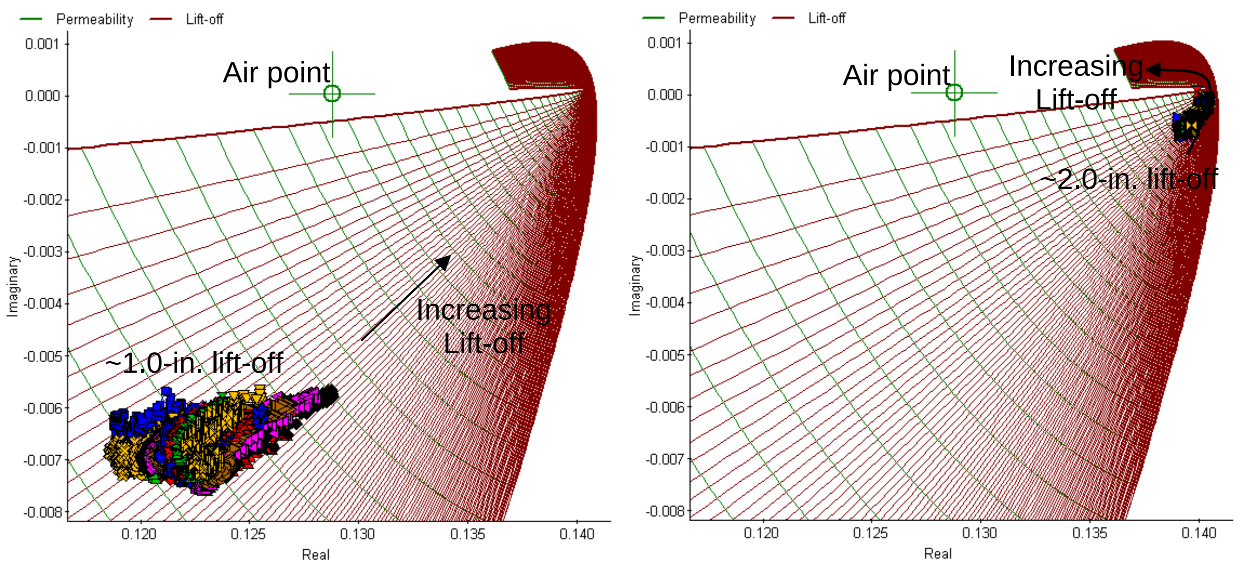

Figure 36. Measurement grid for a VWA001 with a 25.4 mm (1.0-in.) drive-sense gap at 100 kHz. Measurement data are plotted for a (left) 25.4 mm (1.0-in.) and (right) 50.8 mm (2.0-in.) coating.

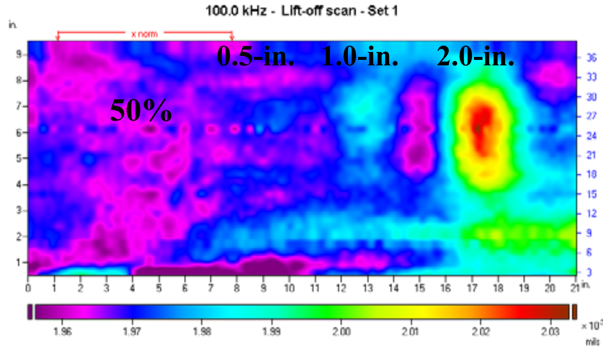

2.00-inch, ref-cal with 0.25-inch shim

Figure 37. Effective lift-off image for the steel pipe with manufactured material loss regions using a VWA001 with a 50.8 mm (2.0-in.) drive-sense gap, a frequency of 100 kHz, and LF probe.

Additional measurements were performed with an even larger drive sense-gap of 76.2 mm (3.0-in.) for a range of coating thicknesses. The top four images of Figure 38 show the results from scans over 0.5 and 1.0-in. thick coatings with both an air-shunt calibration and also a reference calibration. The air-shunt calibration images tend to have less noise while the reference calibration images better indicate the presence of the smaller and shallower flaws. The largest flaw is visible for thicker coatings of 1.5 and 2.0-in. but there is a noticeable degradation of the flaw images. In this case, the use of the drive current amplifier (e.g., current box) substantially improved the flaw images for coating thicknesses of 1.5, 2.0, and 2.5-in. The low-frequency probe was not used for this configuration.

To quantify the results with the various configurations, a signal-to-noise ratio (SNR) analysis was performed. The SNR value was determined from a sense element that passed over largest material loss region (2.0-in. diameter and 50% material loss) by subtracting the average lift-off for an unflawed area from the peak effective lift-off value obtained for the flaw and then dividing the result by the noise (standard deviation of the lift-off for the unflawed area). Similar results were obtained when analyzing the images to obtain the peak response and noise values. If the response to the material loss was not apparent in the data, the SNR value was set to 1.

Figure 39 shows the SNR variation with coating thickness for several drive-sense gaps and test configurations. In general, the SNR values decrease with increasing coating thickness and increase with increasing excitation frequency. For the 25.4 mm (1.0-in.) drive-sense gap, the SNR values are highest for the higher frequencies and for coatings having thicknesses less than approximately 25.4 mm (1.0-in.); reliable results were not obtained at this time with a 50.8 mm (2.0-in.) coating. For the 2.0-in. and 3.0-in. drive-sense gap, the SNR values are still generally highest for the higher frequencies, but there is a more gradual decay in SNR values with increasing coating thickness. While the larger drive-sense gap permits measurements with the thicker coatings, the SNR value was generally larger for the smaller drive-sense gap. Note that the use of the drive current amplifier yielded mixed results; the SNR value increased for 100 kHz but decreased for the other two frequencies.

Figure 39 also shows the low-frequency (LF) probe data for comparison to results for the high-frequency (HF) probe and the HF probe with current box amplification. For both 10 kHz and 100 kHz frequencies and for both drive-sense gap spacings, there tends to be an increase in the SNR value when using the LF probe. (Note that for the LF probe for the 31.75 mm (1.5-in.) coating an air-shunt calibration was used but for the 50.8 mm (2.0-in.) coating a reference calibration was used. Since the use of a reference calibration tends to lead to an increase in SNR value, the apparent increase in SNR with increasing coating thickness for the LF probe can be attributed to the calibration that was used.) **This data confirms that the sensitivity to damage can be improved by varying the drive-sense gap, using refined measurement grids, using somewhat high frequencies (i.e. ≥ 100kHz), and using**

appropriate signal amplification for the sensor array (in this case this is in the form of the low-frequency probe.

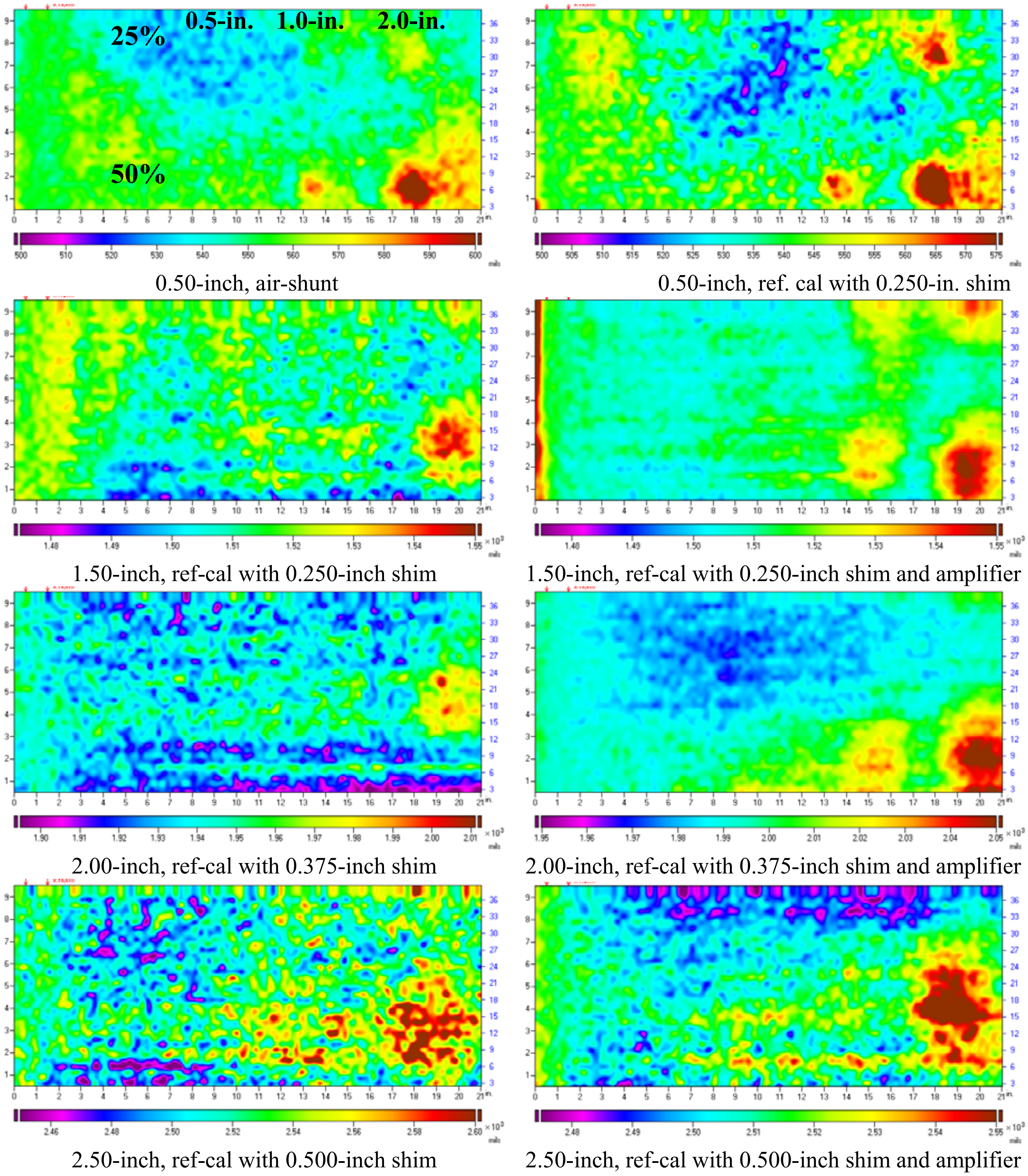

Figure 38. Effective lift-off images for the steel pipe with manufactured material loss regions using a VWA001 with a 76.2 mm (3.0-in.) drive-sense gap and a frequency of 100 kHz.

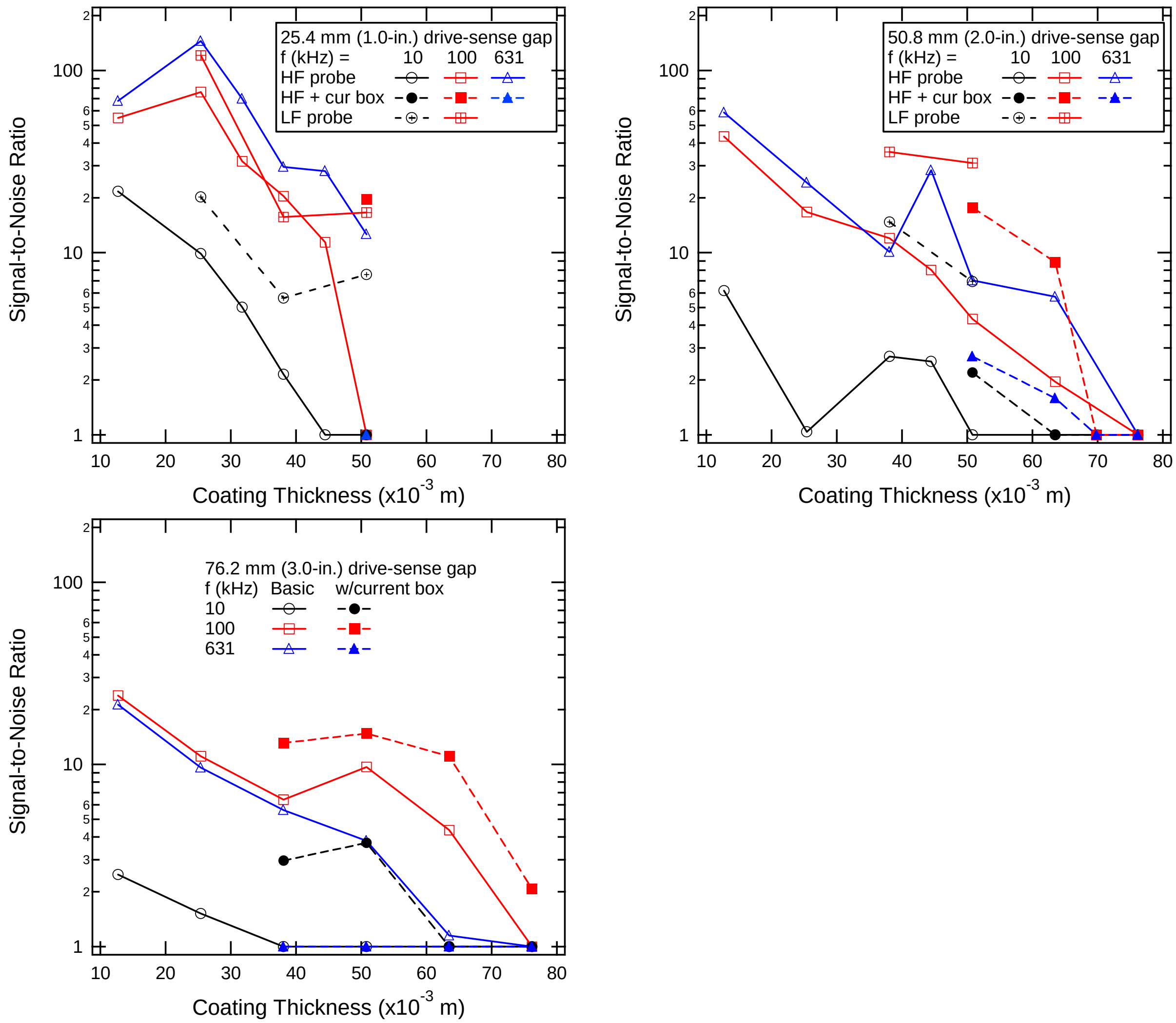

Figure 39. Signal-to-noise ratio variation with coating thickness for effective lift-off changes in response to the 50.8 mm (2.0-in.) diameter 50% material loss region.

In order to reduce the size of the array to make it easier to use during an inspection, configurations with the sense elements placed inside the drive winding loop were investigated. This brought the sense elements closer to the return segment of the drive winding so that the sense elements respond to both the near drive winding segment as well as the return segment. By making the distance to the return segment comparable to the distance to the near segment, the net magnetic field in the vicinity of the sense elements is larger. However, this also required passing the sense element connector leads over the drive winding connections; copper tape was used as a shielding material over most of these leads to minimize this stray coupling. In the following, the copper shielding was used for the VWA001 but not the VWA003.

Measurements were performed with both the VWA001 and the VWA003 arrays with a gap distance between the sense elements and the near drive segment 12.7 mm (0.5-in.). These measurements were taken on a flat steel plate with various insulation coating thicknesses. Figure 40 shows results for a single channel of the VWA001 at 10 kHz and 100 kHz. The data follow a line of constant magnetic permeability as the lift-off increases. Although the grids still collapse at high lift-offs (coating thicknesses) near the air point, the grid itself is better behaved than in Figure 36 and does not wrap around on itself. This indicates a decreased sensitivity to measurement noise. Similar results are observed with the VWA003 as shown in Figure 41.

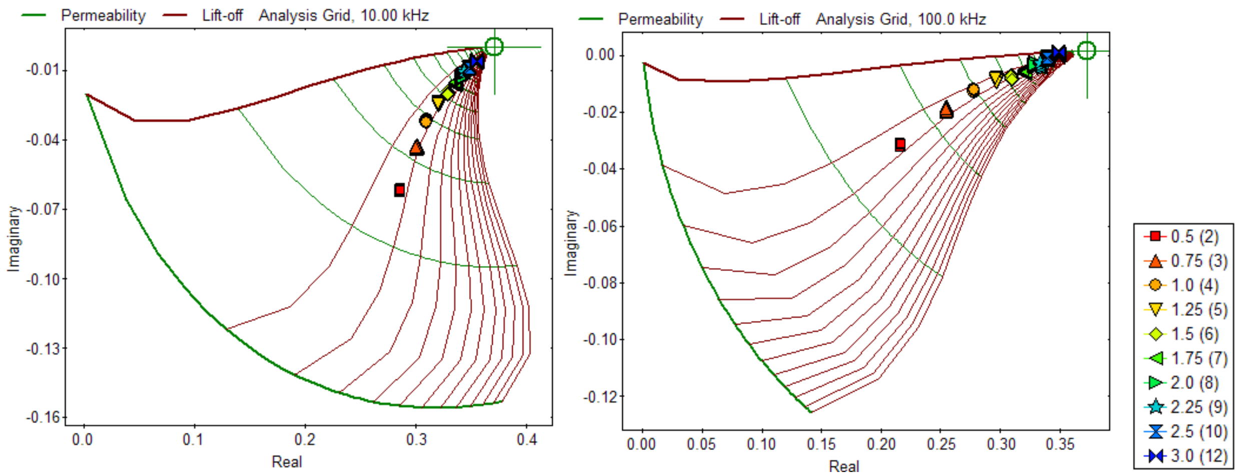

Figure 40. Results for a VWA001 sense element array ***inside*** *the drive winding, a HF probe, and a 12.7 mm (0.5-in.) drive-sense gap. The frequency was (left) 10 kHz and (right) 100 kHz.*

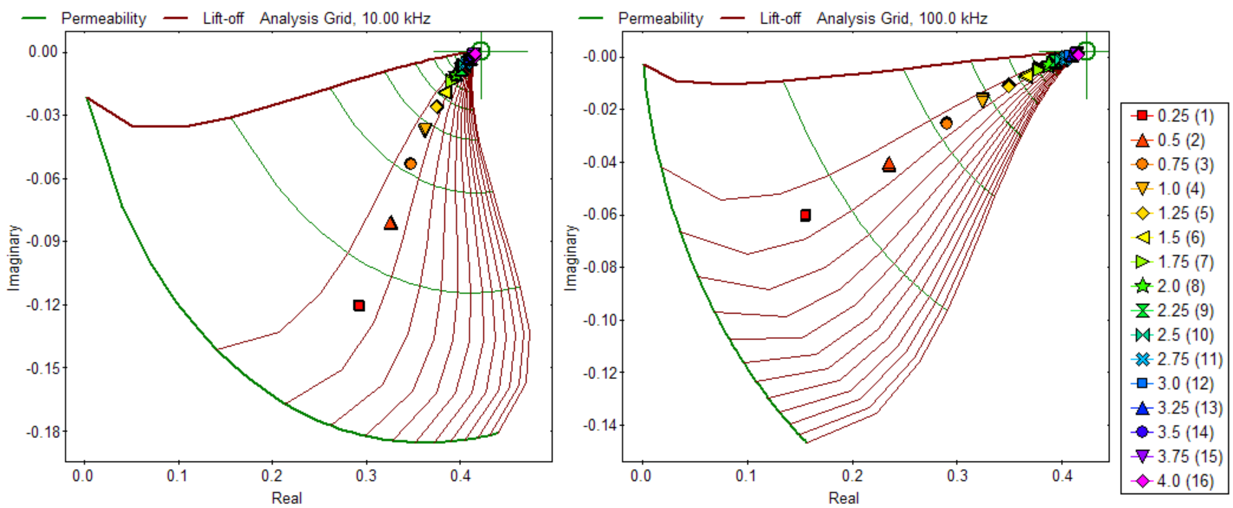

Figure 41. Results for a VWA003 sense element array ***inside*** *the drive winding, a HF probe, and a 12.7 mm (0.5-in.) drive-sense gap. The frequency was (left) 10 kHz and (right) 100 kHz.*

Figure 42 shows the estimated properties obtained with the sense elements inside the drive windings. For the VWA001, measurements were taken up to a coating thickness of 75 mm (3.0-in.) but for the VWA003 measurements were taken for coatings up to 100 mm (4.0-in.) thick. In both cases, the lift-off provides a reasonable estimate of the coating thickness and the permeability values are reasonable. Note that both of these measurements used an air calibration and better results (e.g., better lift-off correlation with coating thickness and a more constant relative permeability) can be expected with a reference calibration**. This is the first demonstration that shows that these eddy-current sensor arrays are sensitive to the steel properties through 100 mm (4 in.) of insulation.** With the added benefit of requiring a smaller sensor footprint, on-going tests are evaluating this configuration for measurements on pipe sections. This approach can also be used with the low frequency sensor array to improve sensitivity to far-surface material loss with inspecting through the pipeline wall.

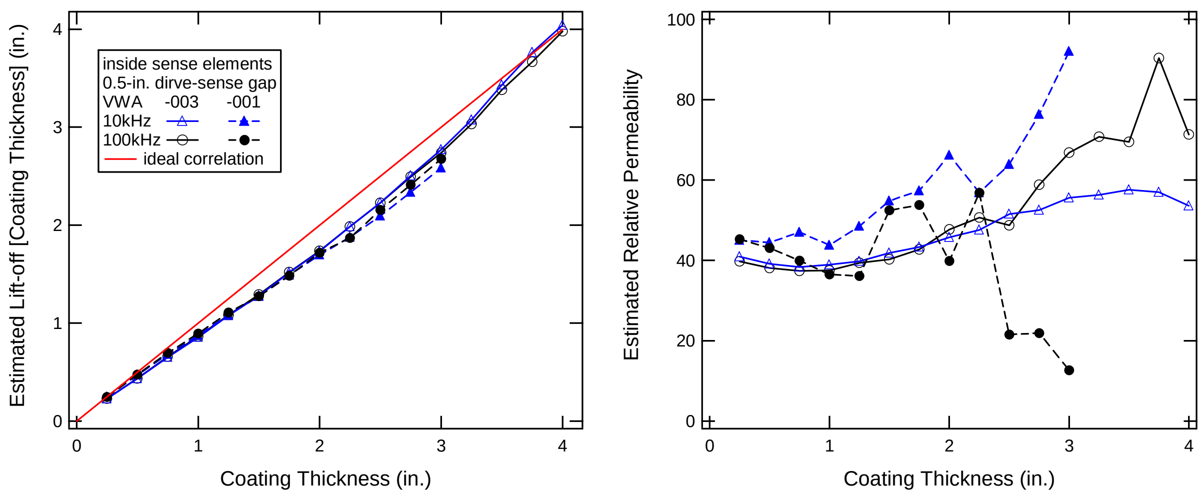

Figure 42. Estimated properties for both the VWA001 and VWA003 with the sense elements ***inside*** *the drive windings for a 12.7 mm (0.5-in.) drive-sense gap and a flat steel plate.*

Several measurements were also performed with the 2nd generation scanning fixture (Figure 15) and the VWA001. The sense element array was positioned inside the drive winding with a 12.7 mm (0.5-in.) spacing between the near drive segment and the sense elements. An air-shunt calibration was performed and low frequency probe electronics were also used. The nominal coating thickness was 12.7 mm (0.5-in.), but in some cases an extra 3.18 mm (0.125-in.) layer of Neoprene was placed underneath the nominal coating in order to test the capability of the scanning fixture to accommodate coating thickness variations. The data was processed using refined permeability/lift-off measurement grids assuming an electrical conductivity of 3.75 %IACS for the steel.

Figure 43 shows the results of an axial scan over flaws having a depth corresponding to a 50% material loss. The 50.8 mm (2.0-in.) and 25.4 mm (1.0-in.) diameter flaws are clearly visible in both the lift-off and permeability images at 100 kHz. Similar results were obtained at 10 kHz. The 12.7 mm (0.5-in.) diameter flaw is visible in the lift-off image but not the permeability image; the color scale can be readjusted and B-scan plots can be used to highlight the presence of this smaller flaw. This baseline scan demonstrates that reasonable flaw images can be obtained on curved pipeline materials through coatings with the sense element array moved inside the drive winding. The estimated lift-off is slightly smaller than the actual coating thickness, which is consistent with the flat plate results of Figure 42. Better agreement is expected with improved sense element designs that have longer lead connections so that the lead shielding layers are farther from the drive winding.

Figure 44 shows the same type of axial scan except a 280 mm (11-in.) wide inner layer of 3.18 mm (0.125-in.) thick Neoprene is placed underneath the 12.7 mm (0.5-in.) thick Neoprene outer layer. This creates a local coating thickness that is similar to what was observed on the coated riser sections described previously. The sensor array was also scanned in the opposite direction compared to Figure 43. The presence of the inner layer is visible in the lift-off images between approximate axial positions of 3.5 and 14.5 inches. Since the Neoprene is relatively stiff, the outer layer does not conform to edges of the inner layer. Consequently, the edge of the inner layer is not very sharp in the images and there appear to be air gaps between the outer layer and steel wall that extend substantially away from the inner layer. Similar results were obtained for the 25% material loss regions with coating thickness variations. The material loss regions are clearly visible in the property images. This confirms that the spring and tensioning portions of the scanner are adequately accommodating the coating thickness changes.

Figure 45 shows the result of increasing the spacing between the drive and sense elements to 19.1 mm (0.75-in.). This figure shows images from axial scans over the (a) 25% and (b) 50% material loss regions through a 25.4 (1.0-in.) thick Neoprene coating. In this case a two-point reference part calibration was used. Both the 50.8 mm (2.0-in.) and the 25.4 mm (1.0-in.) diameter flaws are visible in both the lift-off images for the two regions of material loss. The reference calibration improves the accuracy with respect to the measurement of the absolute coating thickness and reduces element-to-element noise in the images. However, increasing the spacing does not appreciably affect the local signal change associated with the material loss, which is consistent with earlier work that showed a reduction in effective lift-off associated with flaw regions having a diameter (size) that is small or comparable to the coating layer thickness.

Comparisons of axial scans over the 50% material loss regions for both drive-sense spacings are shown in Figure 46 for a 25.4 mm (1.0-in.) coating and Figure 47 for a 38.1 mm (1.5-in.) coating. The images of the flaw regions tend to have a higher spatial resolution for the smaller spacing of 12.7 mm (0.5-in.). However, for a thicker coating of 50.8 mm (2.0-in.) the flaws are not observed with the smaller spacing while, as shown in Figure 48 and Figure 49, the larger flaws still appear for the larger spacing of 19.1 mm (0.75-in.). This is consistent with the results for the sense element array placed on the outside of the drive winding where a larger spacing between the drive winding and the sense elements permits inspections through thicker coatings.

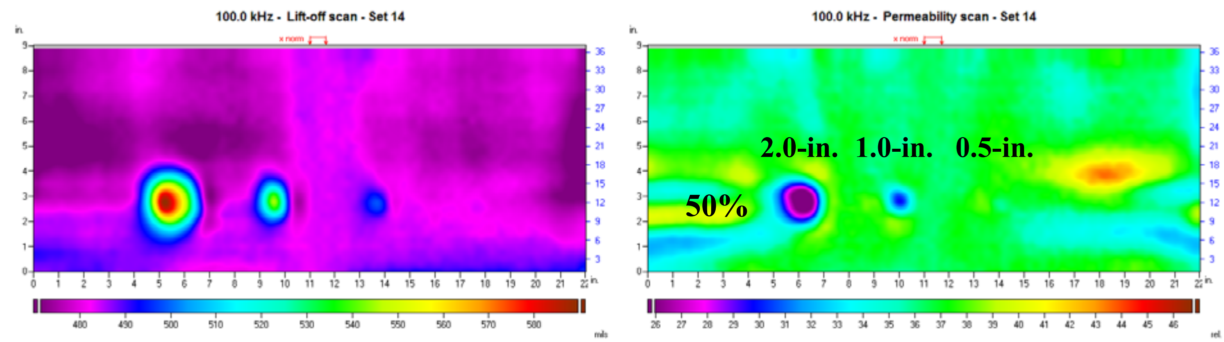

*Figure 43. Axial scans over the 50% loss regions and a 12.7 mm (0.5-in.) coating using a VWA001 with the sense element array placed **inside** the drive and with a spacing of 12.7 mm (0.5-in.).*

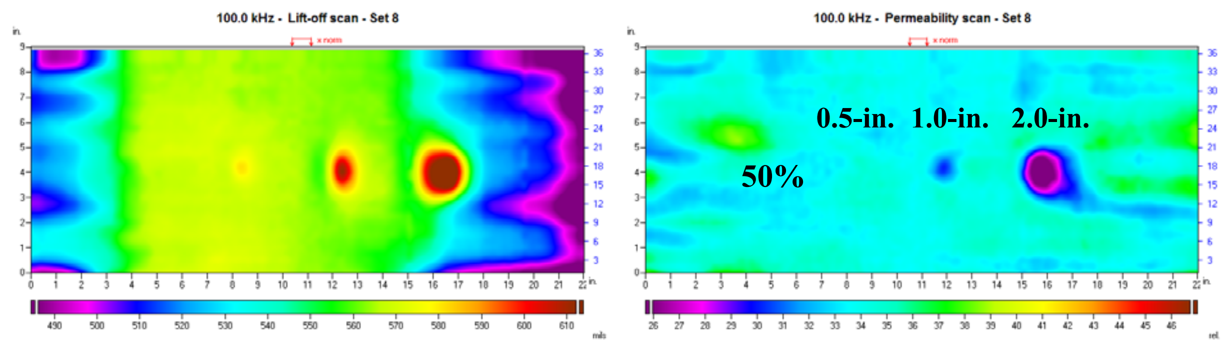

*Figure 44. Axial scans over the 50% loss regions and a 12.7 mm (0.5-in.) coating using a VWA001 with the sense element array placed **inside** the drive and with a spacing of 12.7 mm (0.5-in.). An extra layer of 3.18 mm (0.125-in.) thick insulation was placed under the coating.*

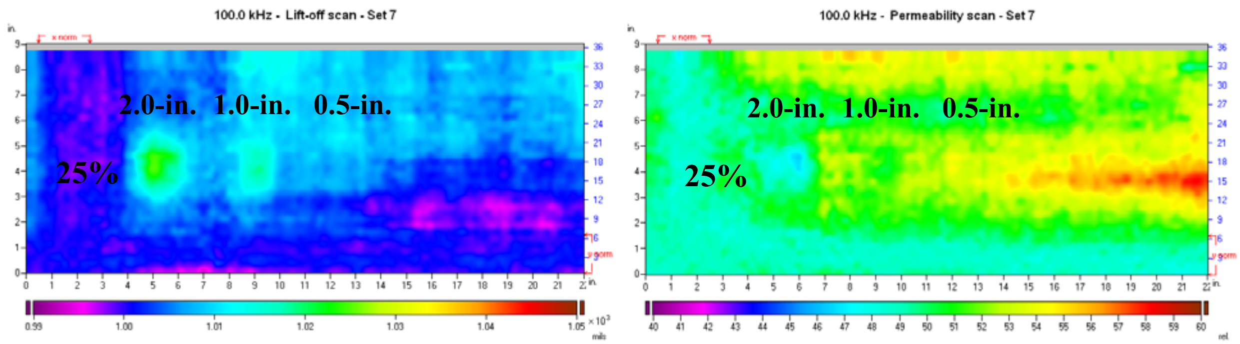

(a)

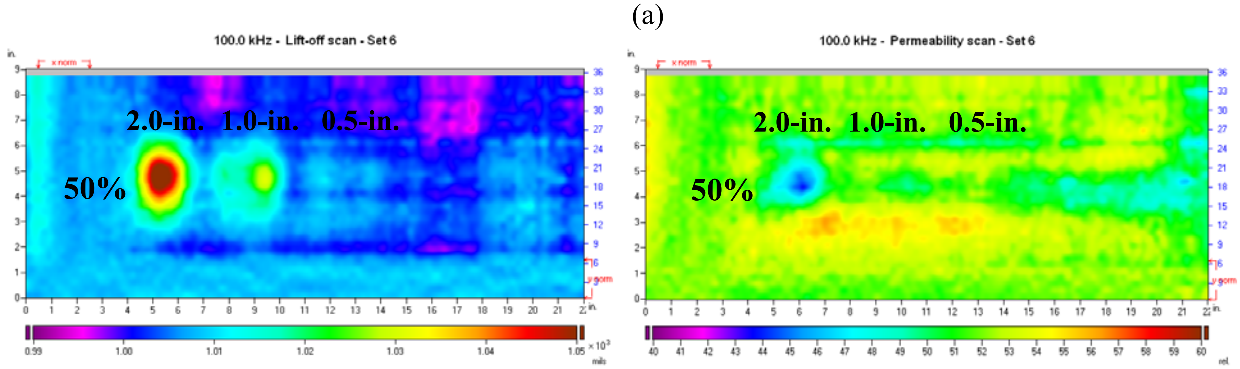

(b)

Figure 45. Axial scans over the (a) 25% and (b) 50% material loss regions and through a 25.4 mm (1.0-in.) Neoprene outer layer using a VWA001 with the sense element array placed ***inside*** *the drive and with a spacing of 19.1 mm (0.75-in.) A two-point reference part calibration was performed.*

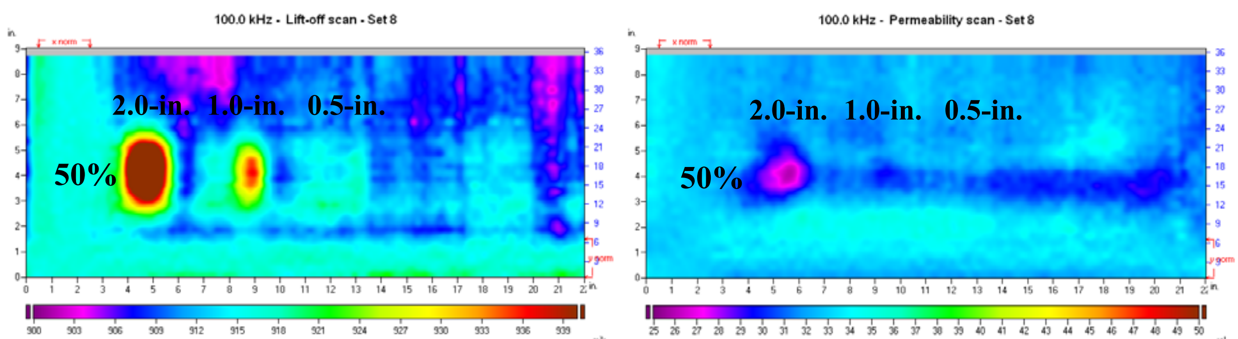

(a)

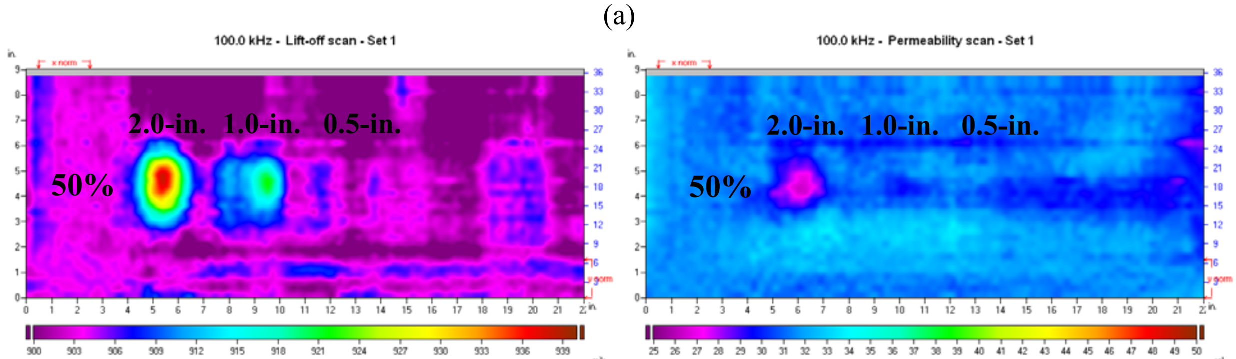

(b)

Figure 46. Axial scans over the 50% material loss regions and a 25.4 mm (1.0-in.) Neoprene outer layer using a VWA001 with the sense element array placed ***inside*** *the drive and with a (a) spacing of 12.7 mm (0.5-in.) and (b) 19.1 mm (0.75-in.). An air calibration was performed.*

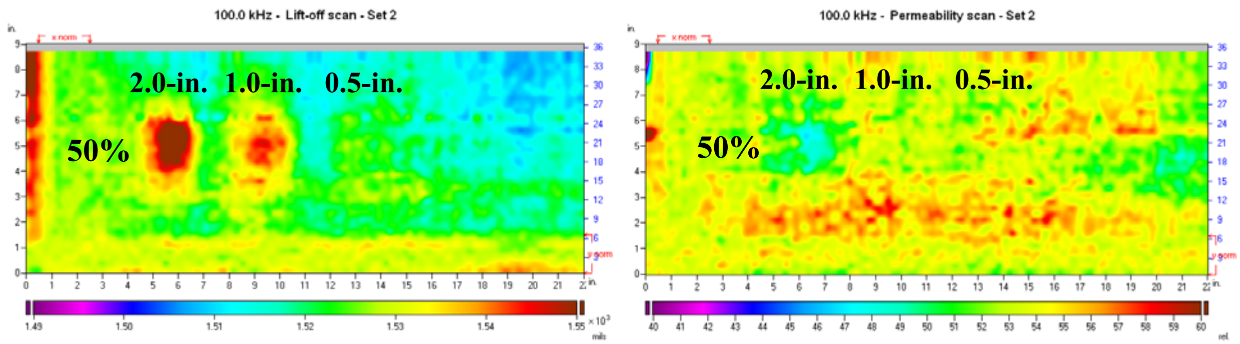

(a)

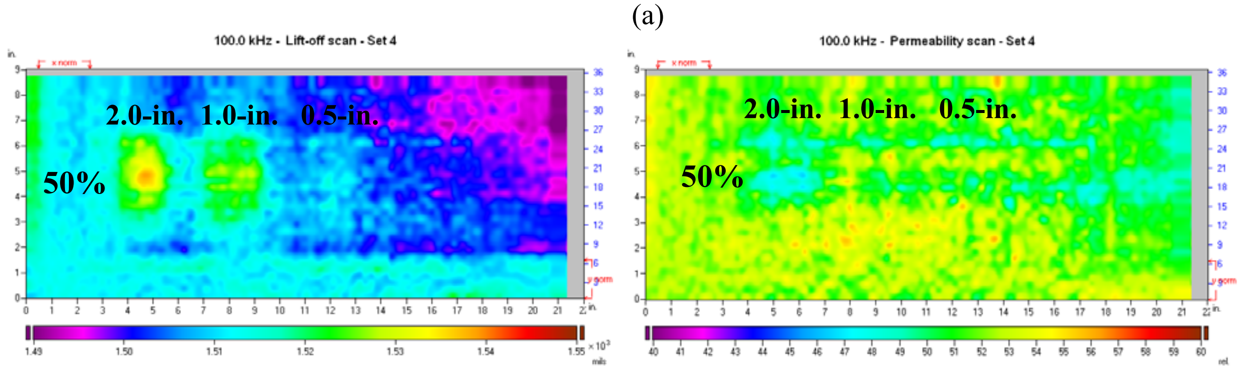

(b)

Figure 47. Axial scans over the 50% material loss region through 38.1 mm (1.5-in.) Neoprene outer layer using a VWA001 with the sense element array placed ***inside*** *the drive and with a spacing of (a) 12.7 mm (0.5-in.) and (b) 19.1 mm (0.75-in.). A two-point reference part calibration was performed.*

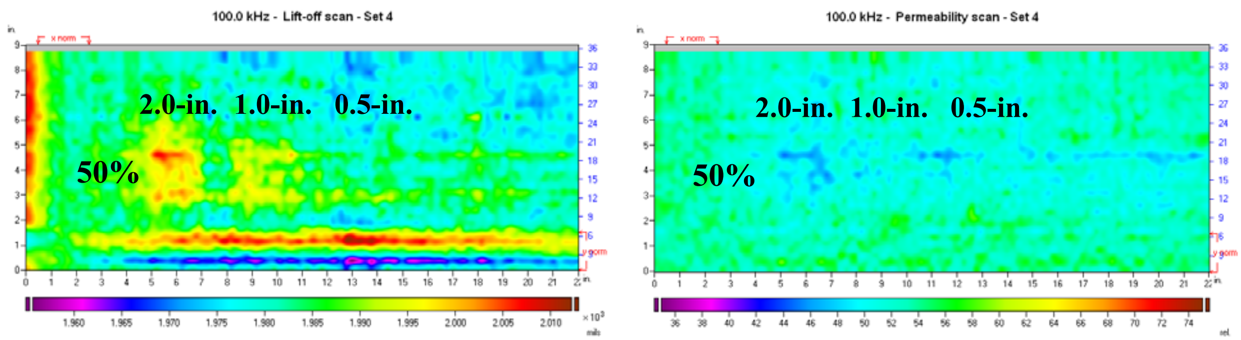

Figure 48. Axial scans over the 50% material loss region through 50.8 mm (2.0-in.) Neoprene outer layer using a VWA001 with the sense element array placed ***inside*** *the drive and with a spacing of 19.1 mm (0.75-in.). A two-point reference part calibration was performed.*

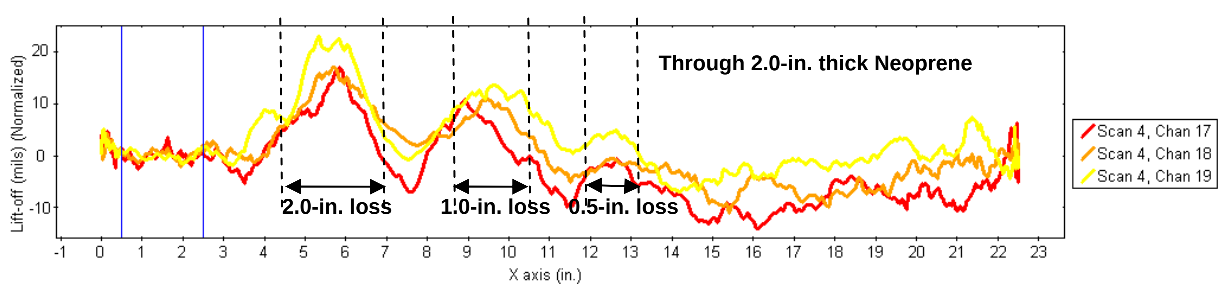

Figure 49. B-scan plot of lift-off measurements with a VWA001 sensor with a 19.1 mm (0.75-in.) spacing between the drive winding and the sense elements. A two-point reference part calibration was performed for scans through 50.8 mm (2.0-in.) thick Neoprene outer layer, over the region of 50% material loss.

Similar measurements were performed with the VWA003 and the hand-held scanning fixture (Figure 16). Figure 50 shows a representative set of property images obtained for the 50% material loss regions and high frequency probe electronics. Three material loss regions are visible in both the lift-off and the permeability images at 10 kHz and in the lift-off image at 100 kHz. These measurements demonstrate the capability for using the smaller scanner to image damage, albeit with a narrower scan width as compared to the VWA001.

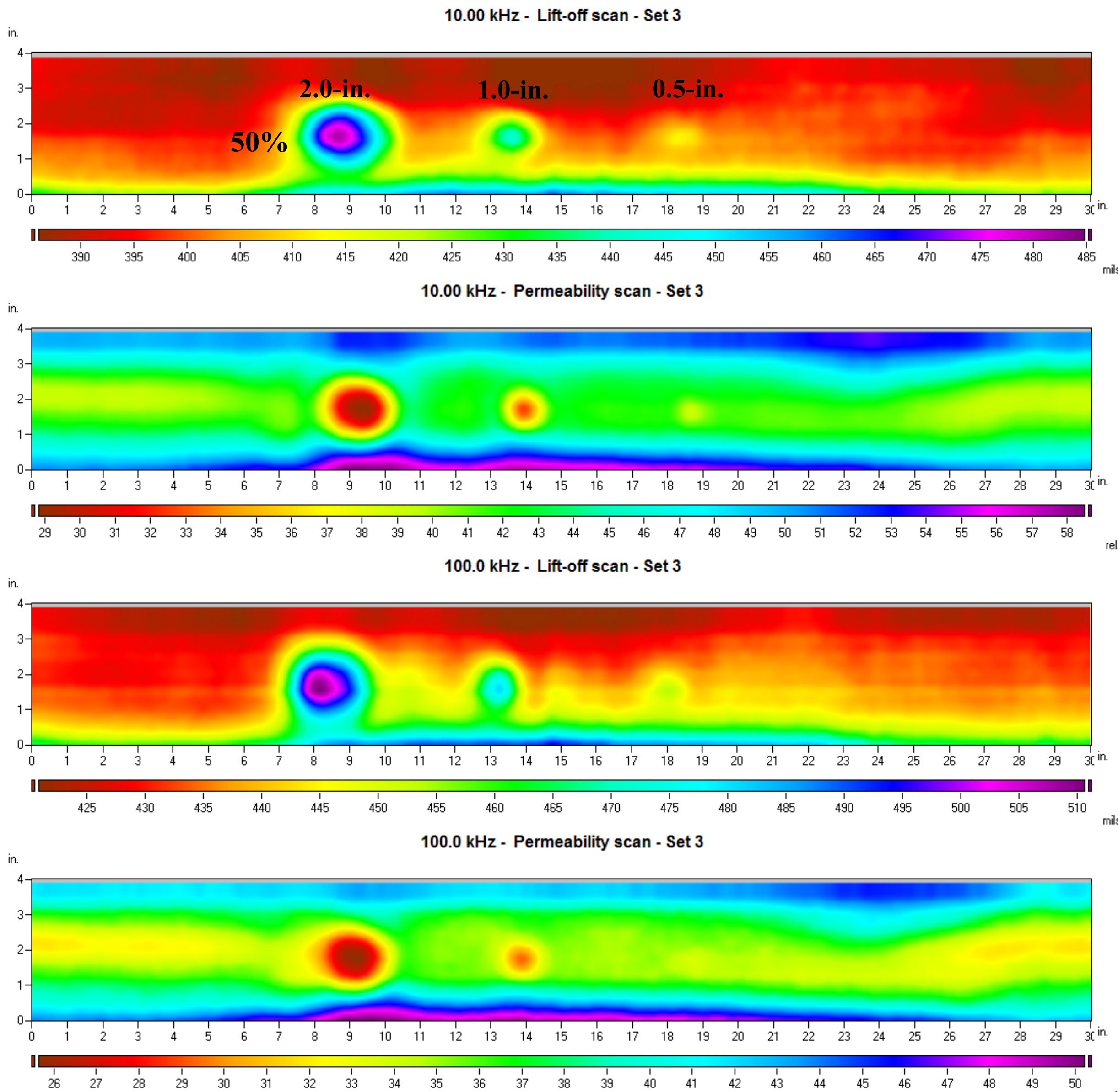

Figure 50. Axial scans over the 50% loss regions and a 12.7 mm (0.5-in.) coating using a VWA003 with the sense element array placed ***inside*** *the drive and with a spacing of 12.7 mm (0.5-in.).*

Figure 51 shows the lift-off images from high frequency (631 kHz) axial scans at different positions around the circumference of the pipe section using the VWA003. Through this moderate thickness coating of 6.35 mm (0.25-in.), all of the flaws that are 12.7 mm (0.5-in.) in diameter and larger are clearly visible, even for a 5% material loss. The 6.35 mm (0.25-in.) diameter flaw is visible for 25% and 50% material loss. **This shows that the larger MWM-Arrays can also be used to inspect through**

relatively thin layers of insulation and to provide a reasonable spatial resolution of the damage. This supports the external inspection project as well as the project for inspection from the inside as this type of array may be used to provide complete circumferential coverage of the internal surface while accommodating realistic stand-off distances.

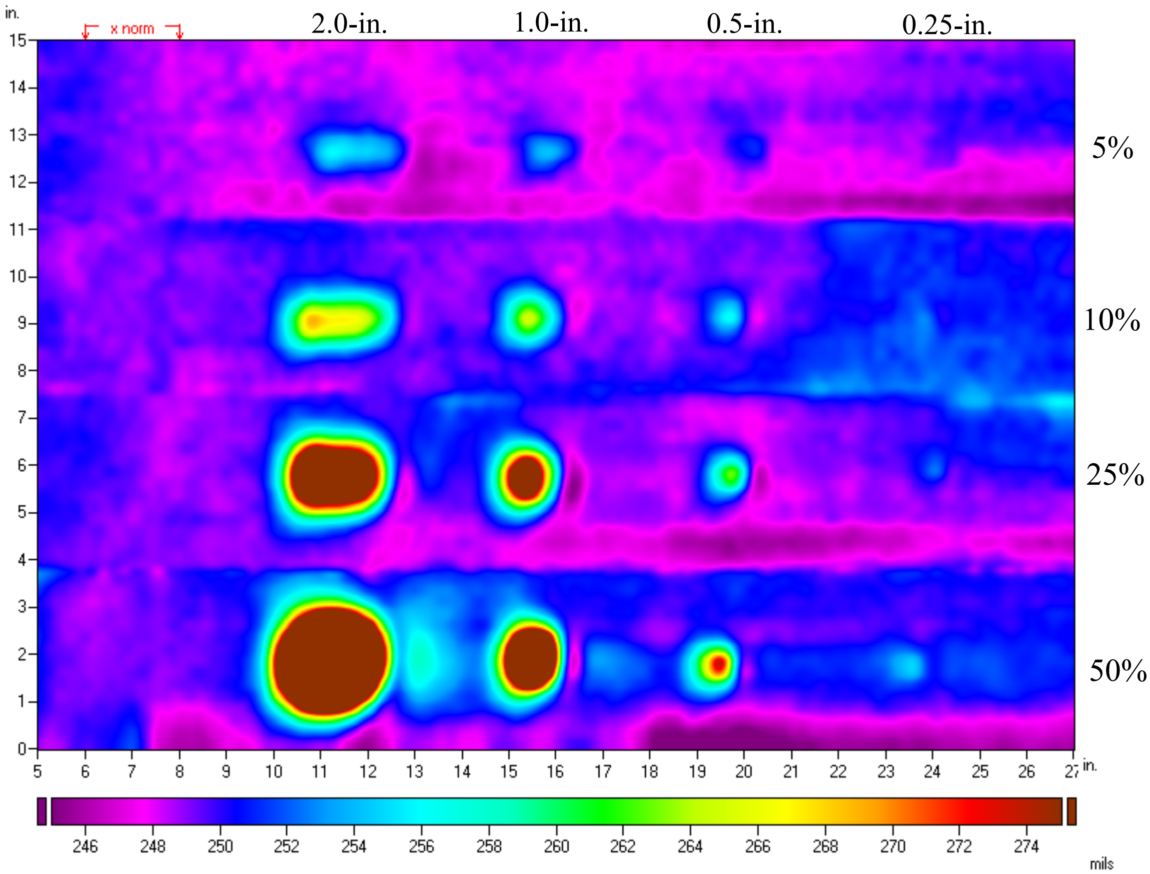

Figure 51. Axial scans over the 5%, 10%, 25% and 50% material loss regions through a 6.35 mm (0.25-in.) Neoprene outer layer using a VWA003 with the sense element array placed inside the drive and with a spacing of 12.7 mm (0.5-in.) A two-point reference part calibration was performed.

6.4.1.3 Measurements on a pipe section removed from service

Several FA24 scans were performed over a region on the inside surface of a 16-in. diameter pipeline section that exhibited actual corrosion damage within a steel pipeline. The surface was relatively rough and includes several regions of significant material loss. In these measurements, an air-shunt calibration was performed and a position encoder was attached to the probe electronics to allow spatial mapping to be performed. Two 0.010-in Mylar shim were attached on to the sensor with double-sided tape (each 0.003-in) and two pieces of 0.010-in plastic were placed on the surface of the pipeline section. Figure 52 and Figure 53 show that the material loss and pitting from the corrosion generally appear as a change in both the lift-off and permeability. These results are consistent with the measurements on the laboratory pipe section that has machined areas of material loss.

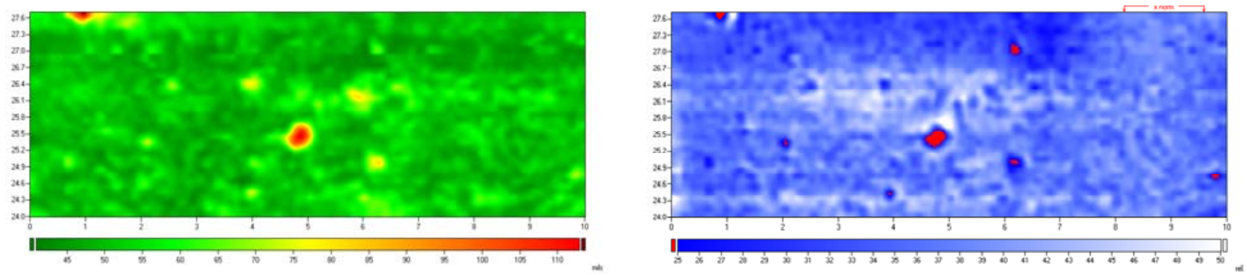

Figure 52. Lift-off (left) and permeability (right) scan images of material loss on the inside surface of the pipeline section through a 0.046-in. coating using an FA24 MWM-Array.

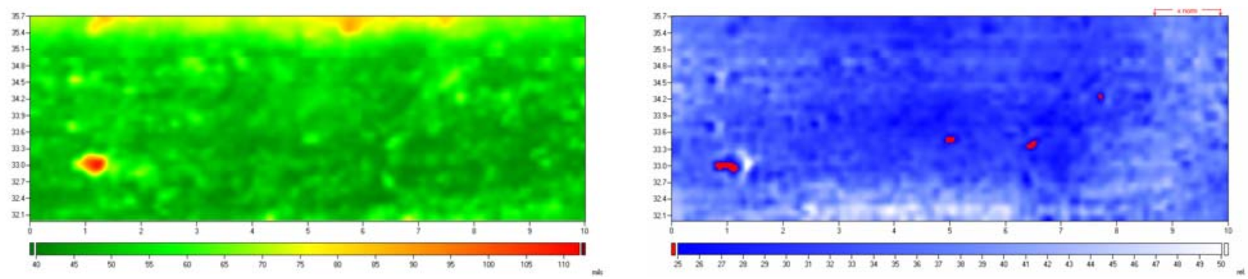

Figure 53. Lift-off (left) and permeability (right) scan images of material loss on the inside surface of the pipeline section through a 0.046-in. coating using an FA24 MWM-Array.

6.4.1.4 Measurements on risers

Measurements have also been performed on 40 ft long, 6.-in. diameter riser sections made available by Chevron and PRCI (Pipeline Research Council International). Figure 54(left) shows five sections containing embedded defects. The schedule 80 steel pipe are coated over approximately 30 ft with 0.5-in. thick “Splashtron” neoprene coating. This coating includes a cloth wrap and is relatively hard since it was vulcanized at elevated temperatures. Each of these pipeline sections contains a mixture of girth welds and embedded flaws of various sizes and orientations. After creating the damage area, the corrosion products were embedded in the flaw region prior to coating. This should have made these samples representative of actual corrosion under coatings.

For these measurements, the prototype external scanner fixture of Figure 54(center) was used along with the VWA001 MWM-Array. The drive-to-sense element gap of the array was set to 1-in. Teflon tape was applied to the portion of the sensor array in contact the Splashtron during the scans to protect the sensor array. The surface of the insulation was uneven; the cloth tape was spiral-wrapped around the insulation creating a surface roughness periodicity of roughly 0.25-in. and the nominal thickness of the coated pipe sections could change, with a circumference change of 0.5-in. common over the span of several feet. Although the foam backing between the sensor array and the support plastic layer wrapped around the pipe provides some compliance, it was not enough to accommodate such large circumferential changes. Consequently, shorter scans were generally required where the coated pipe diameter did not change dramatically over the scan. In follow-on efforts, we plan to develop other methods for maintaining a constant gap between the sensor and the outer pipeline steel surface (or the pipeline centerline).

Figure 54. (Left) Simulated pipeline riser sections with embedded corrosion defects. (Center) Photograph of a prototype external scanner. (Right) Photograph of one of the defects.

For these measurements an air-shunt calibration was performed. Scans were performed at several positions around the circumference to construct a scan image. Each pass of the array imaged approximately ¼ of the pipe surface so four passes spaced approximately 90 degrees apart were used to image the pipe circumference. A chalk line was used to maintain the circumferential position during each scan. The measurement data for each channel was converted into an effective lift-off and permeability using measurement grid methods. Excitation frequencies of 10, 100, and 630.9 kHz were used along with a high-frequency probe; the best results were generally observed with the 100 kHz data.

Figure 55 through Figure 57 show preliminary results over several detected flaws in the pipe underneath the coating. The *x* and *y* axes in the images have dimensions of inches. These are absolute images, without intelligent filtering, where the impedance measurement data has been processed with measurement grids to determine the lift-off (proximity of each sense element to the steel pipe surface (which provides an image of the surface topology, i.e., geometric variations) and the relative permeability for the outer surface steel pipe wall (which is related to material property and residual stress in the outer surface of the steel wall). Flaw responses are evident in each of these images and appear as a local increase in lift-off and variation in magnetic permeability; variations in lift-off that are not associated with a change in the magnetic permeability are caused by coating thickness variations (thus, with intelligent filtering, we anticipate a low false indication rate). Note that no attempt was made to filter these images to reduce channel-to-channel variability (or striping) of the images at this time. It is anticipated that further enhancements in the fixturing and data processing will yield much better images.

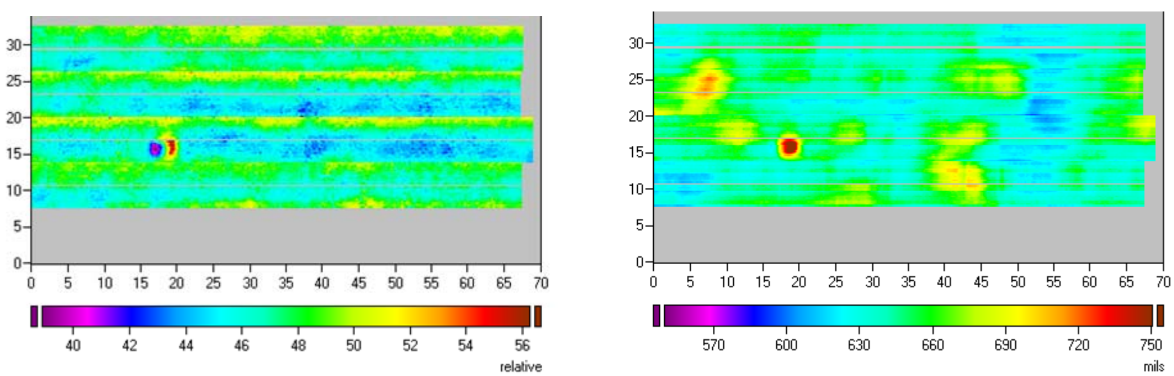

Figure 55. Scan images over an elongated flaw. (Left) Relative permeability. (Right) Lift-off.

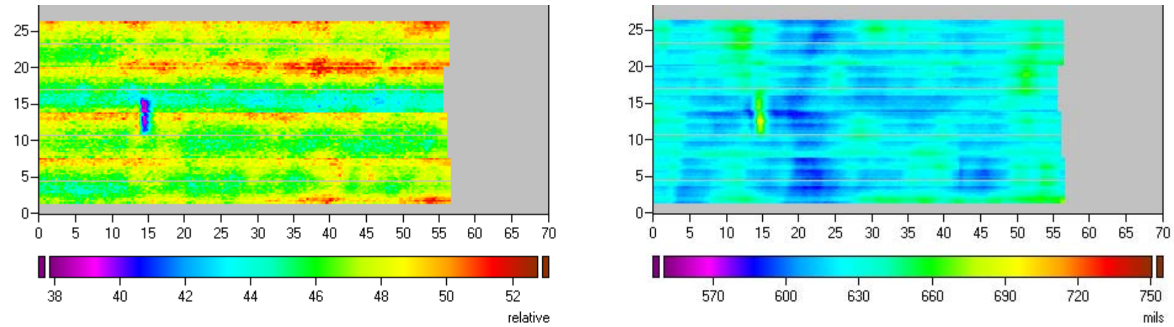

Figure 56. Scan images over a circumferential flaw. (Left) Relative permeability. (Right) Lift-off.

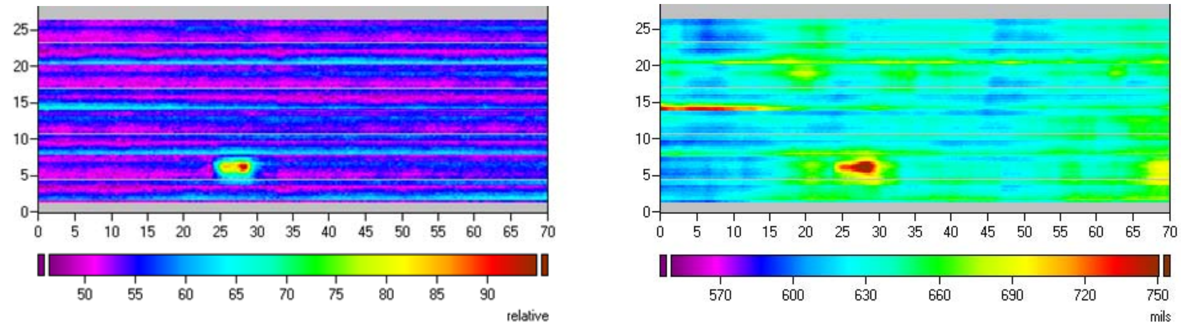

Figure 57. Scan images over an axial flaw. (Left) Relative permeability. (Right) Lift-off.

Scans were performed over four of the five pipe sections. For three of the pipe sections, scans were performed over both the end and middle sections which are separated by the ground support. The sensor fixture was not able to scan the pipe sections over the ground supports and these regions are considered uninspectable with this fixture. Figure 58 shows a representative composite image showing several scan images and a schematic of the pipe section. An axial flaw is visible in the leftmost images. The center region appears to contain two welds (circumferential indications) with a material change between the two pipe sections at the left weld and a defect near the right weld. The rightmost images do not show any flaws.

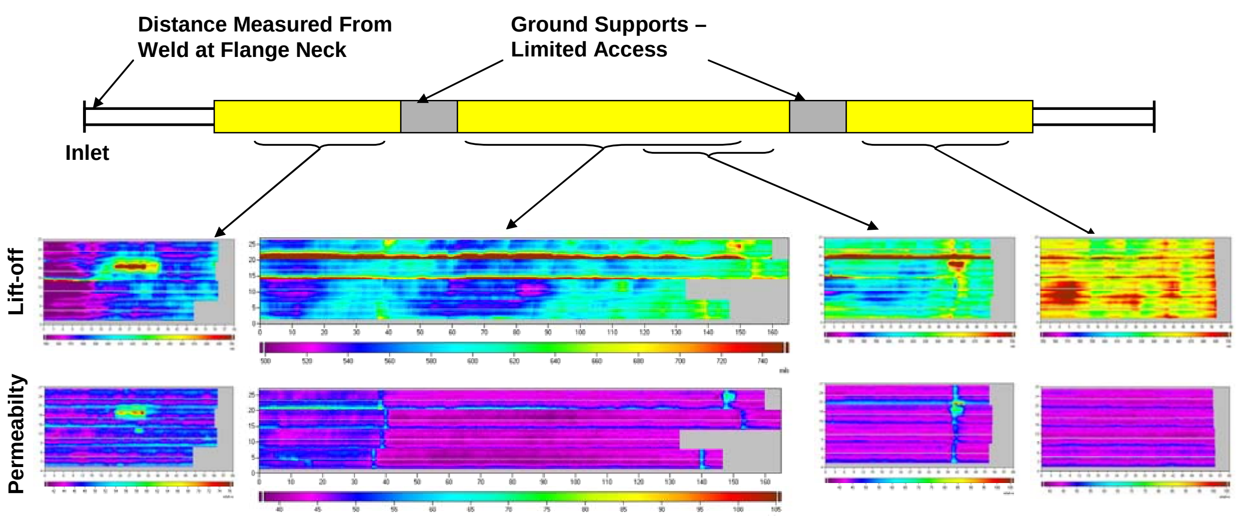

Figure 58. Composite image for one of the pipe sections.

The initial results obtained with the prototype scanning fixture are encouraging, but addressing some of the fixture limitations will result in equipment that can more readily be transitioned to field use for scanning through coatings. The limitations in the prototype fixture include: 1) the foam backing behind the sensor array not being compliant enough to accommodate the coating thickness variations; 2) the endmost sense elements not being reliably held near the pipe section surface; 3) the position encoder wheel not reliably providing scan position; and 4) the fixture weight needing to be reduced to more readily allow scans with the fixture upside down. Several of these limitations are addressed with the 2nd generation wrap-around fixture of Figure 15 and the hand-held fixture of Figure 16.

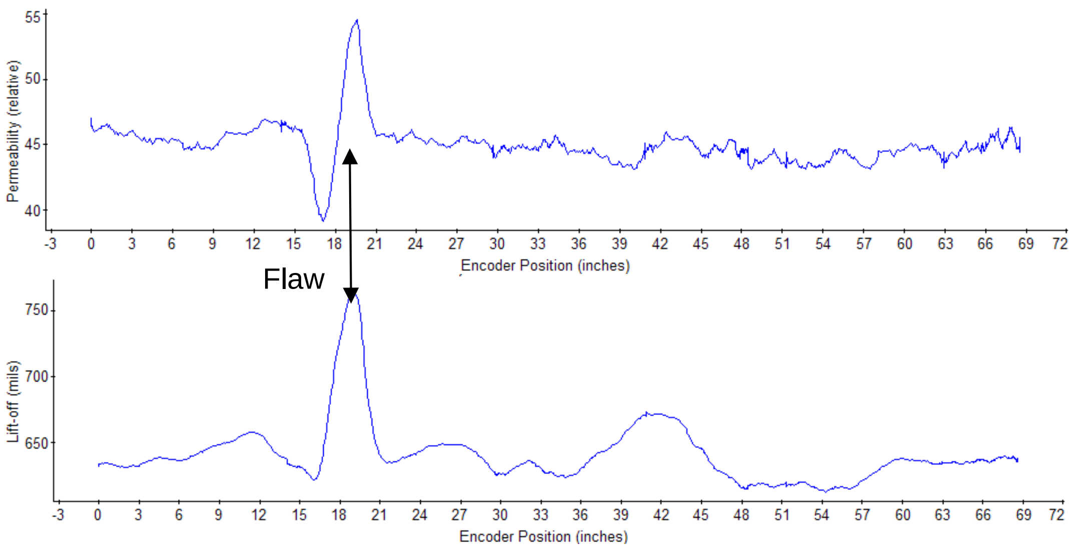

Figure 59. VWA001 response with a 1.0-in. drive gap at 100 kHz for the Chevron pipe samples having a 0.5-in. Splashtron coating for an oblong-shaped indication.

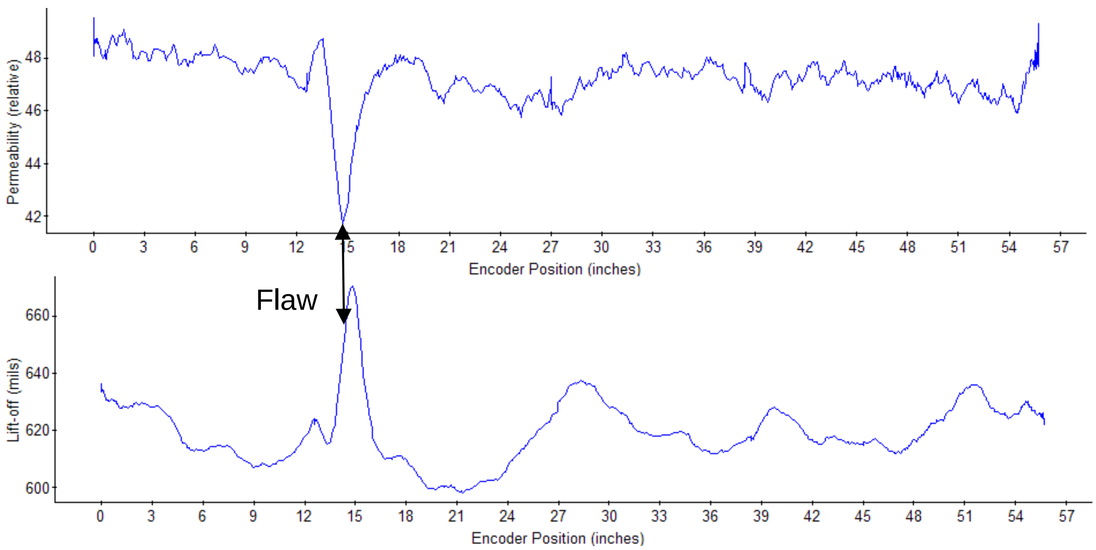

Figure 60. VWA001 response with a 1.0-in. drive gap at 100 kHz for the Chevron pipe samples having a 0.5-in. Splashtron coating for a circumferentially-oriented indication.

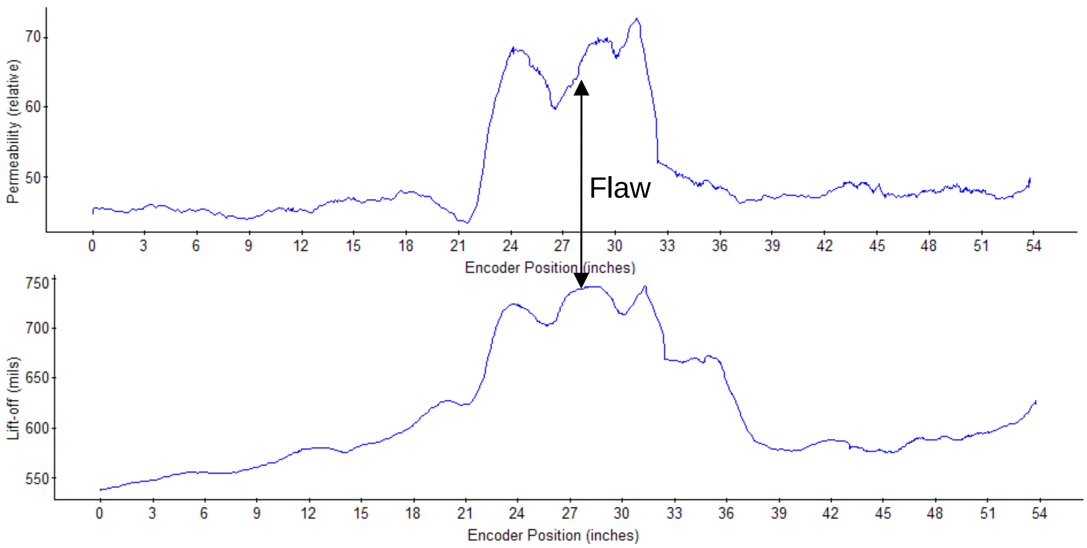

Figure 61. VWA001 response with a 1.0-in. drive gap at 100 kHz for the Chevron pipe samples having a 0.5-in. Splashtron coating for an axially-oriented indication.

A series of simulations were also performed to determine how the effective property values represent the near-surface material loss conditions. These simulations used a two-dimensional finite element model and calculated the effective permeability and lift-off as the flaw width and position relative to a VWA001 sensor array are varied. A drive width of 101.6 mm (4.0-in.), as in the VWA001, and a drive-sense gap of 25.4 mm (1.0-in.) were assumed. Figure 62 shows the results for a coating thickness of 12.7 mm (0.5-in.) and a flaw depth of 2.54 mm. For a 12.7 mm (0.5-in.) steel wall thickness, this corresponds to 20% material loss. For wide flaws with a width greater than about 50.8 mm (2.0-in.) the effective lift-off has plateau and peak that approach the lift-off change associated with the actual flaw depth and the effective permeability has a central peak with local minima on either side of the peak that occur when the drive winding closest to the sense element passes over the edge of the flaw. For narrow flaws, the peak in the effective lift-off becomes much smaller than the lift-off change associated with the presence of the flaw, which is consistent with previous work that showed that flaw geometry must be accounted for in the material loss depth estimates when the extent of the flaw becomes small compared to the sensor dimensions. Note that the extent of the material loss is approximately equal to the full-width-at-half-maximum for the effective lift-off response. The effective permeability has a relatively complicated dependence on the flaw width and scan position; however, it is worth noting that these plots are consistent with the measurement results obtained for oblong, axial, and circumferential flaws in the 6-in. diameter pipe sections shown in Figure 59 through Figure 61. Similar results are obtained when the coating thickness is increased to 25.4 mm (1.0-in.), as shown in Figure 63, or when the material loss is increased to 7.62 mm (60% material loss for a 12.7 mm wall), as shown in Figure 64. This indicates that the effective lift-off change needs a flaw-width correction factor to provide an accurate depth estimate, at least for the narrower flaws.

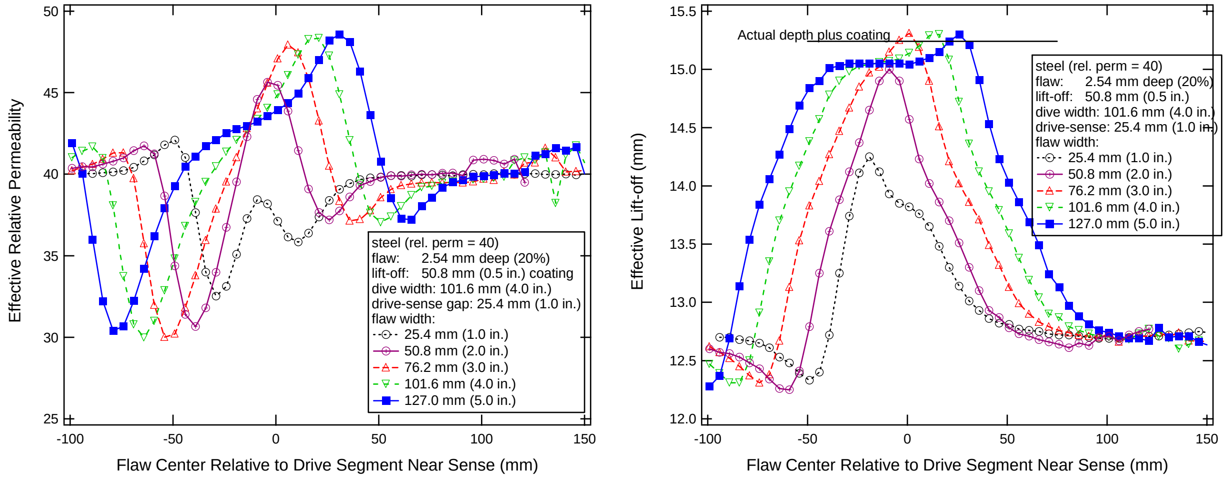

Figure 62. Effective property response as the flaw center and width are varied for the VWA001 with a drive-sense gap of 25.4 mm (1.0-in.). The coating thickness was 12.7 mm (0.5-in.).

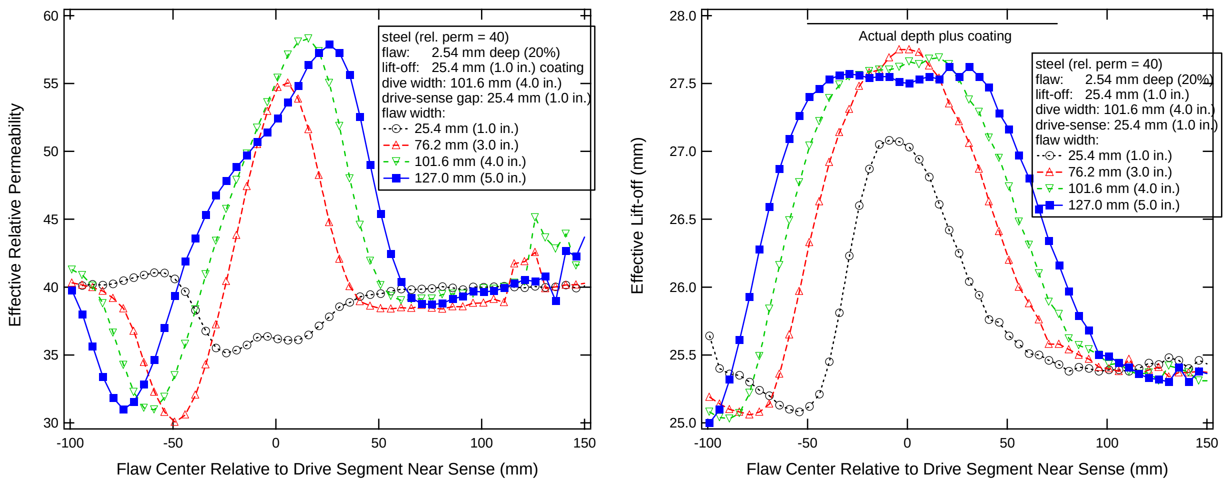

Figure 63. Effective property responses as the flaw center and width are varied for the VWA001 with a drive-sense gap of 25.4 mm (1.0-in.). The coating thickness was 25.4 mm (1.0-in.).

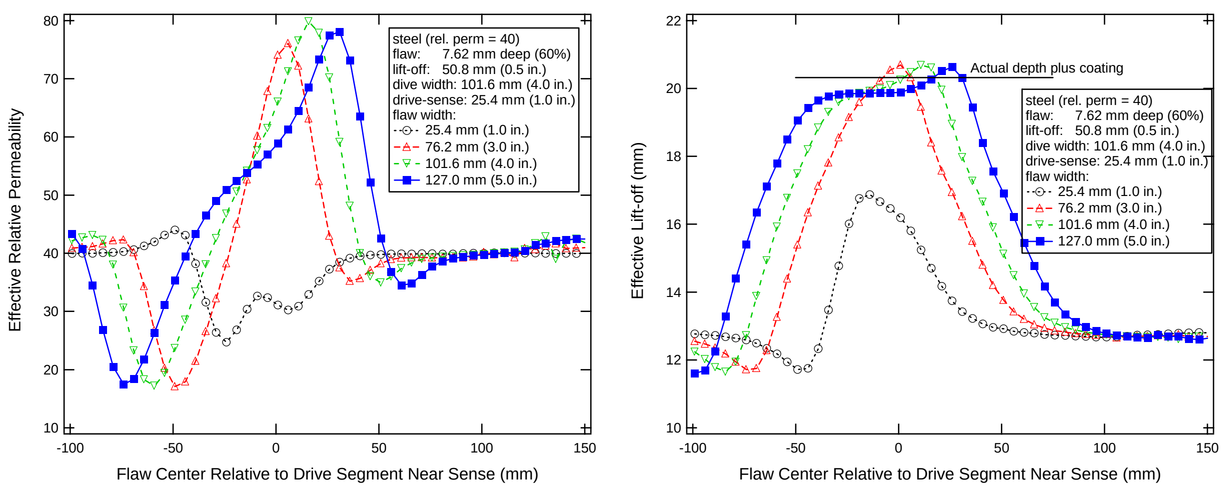

Figure 64. Effective property response as the flaw center and width are varied for the VWA001 with a drive-sense gap of 25.4 mm (1.0-in.). The coating thickness was 12.7 mm (0.5-in.). The depth of the flaw was 7.62 mm (0.3-in.).

6.4.2 Mechanical Damage Imaging

Several measurements have shown that the MWM-Arrays can image mechanical damage in steel. These measurements involve scanning an MWM-Array over the surface, processing the data with measurement grids to obtain lift-off (sensor proximity) and permeability images of the material being inspected, and evaluating these images to determine the presence and extent of the damage. Mechanical damage appears as both an increase in sensor proximity, i.e., lift-off (associated with denting or gouging of the surface), and a variation in the local magnetic permeability (which is associated with variations in the residual stress around the damage site and other microstructure changes due to plastic deformation).

Measurements were performed on a flat steel plate to demonstrate the capability of the MWM-Arrays to image mechanical damage through thin and moderate thickness coatings. The steel plate had dimensions of 12-in. x 12-in. x 0.064-in. A hydraulic press was used to introduce a dent into the center of the steel plate. As shown in Figure 65, the 1-in. diameter punch created a shallow (0.100 in.), flat-bottomed depression, surrounded by a depressed region. For the measurements, JENTEK's small-size FA24 and the VWA001 MWM-Array sensors were scanned over the plate. The smaller size of the FA24 makes it more suitable for obtaining high spatial resolution images of damage through relatively thin coatings while the VWA001 is more suitable for thicker coatings. For both sensors, an air-shunt calibration was performed. This type of calibration uses a measurement in air and a measurement with a shunt sensor in which the sense elements are shorted. The frequency used for both sensors was 100 kHz.

Figure 66 shows B-scans across the damage region, and the corresponding images. The peak change in lift-off is approximately 0.100-in., consistent with caliper measurements on the plate itself. Based on some of the other research with thicker coatings, as long as the damage region is large compared to the coating thickness, the change in the lift-off associated with the damage provides a reasonable measure of the depth of the damage. Additional information is available in the magnetic permeability plot. There is a considerable change in the magnetic permeability beyond the region where the lift-off change was apparent (about an extra 1.0-in. in this case). This probably reflects the residual stress distribution; additional work is required to confirm the spatial variation in the stress distribution for this type of damage, either with finite element analysis of the stress or through a comparison to literature, if available.

Figure 65. (Left) A dented steel plate. (Right) Plate with an FA24 MWM-Array and a 0.020-in. plastic sheet.

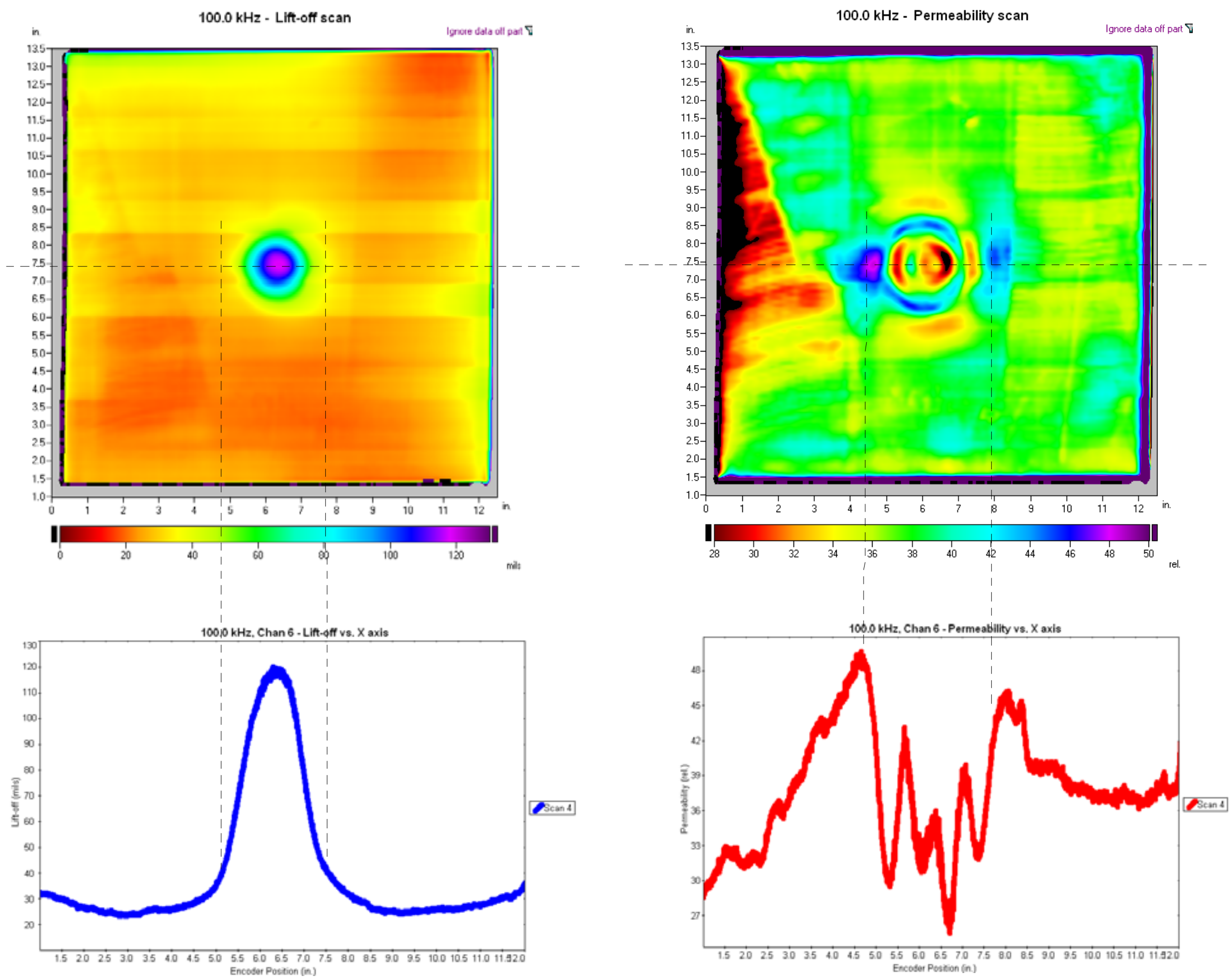

Figure 66. B-Scans of lift-off (left) and permeability (right) across the damage region with an FA24.

Similar measurements were performed with the VWA001 and a thicker (0.5-in.) coating. For these measurements, the gap between the drive and sense elements was set to 1.0-in. The VWA001 was placed in a 2D scanner for creating scan images. Due to limitations on the y-axis for the scanner and the large sensor array size, data was only obtained for angles of -45° and +45°. In these scans, the surface of the Neoprene coating, used to create the 0.5-in. stand-off, was found to be somewhat sticky and an additional 0.010-in. Mylar shim was placed over the surface to facilitate scanning.

Figure 67 shows a set of images obtained with the VWA001 and an angle of -45°. The mechanical damage region is again visible in both the lift-off and permeability. However, the spatial resolution of the images is lower and there is a broadening of the responses to the regions compared to the FA24. This is illustrated more clearly in Figure 68, which plots the responses for both the FA24 and VWA001 relative to the center of the mechanical damage region. The lift-off change is the measured lift-off minus the nominal coating thickness. For the VWA001, the response is slightly wider because the fields diffuse or spread out further through the thicker coating. The peak is also smaller for the VWA001 as the coating thickness becomes comparable to the size of the damage region and a shape correction should be used with the measurement grids. For the permeability, there is a shift in the baseline responses that may be a result of the sensor array being large compared to the sample and edge effects as part of the sensor is off of the plate. For the VWA001, the sharp features in the spatial permeability variations are averaged together so that more gradual trends are observed.

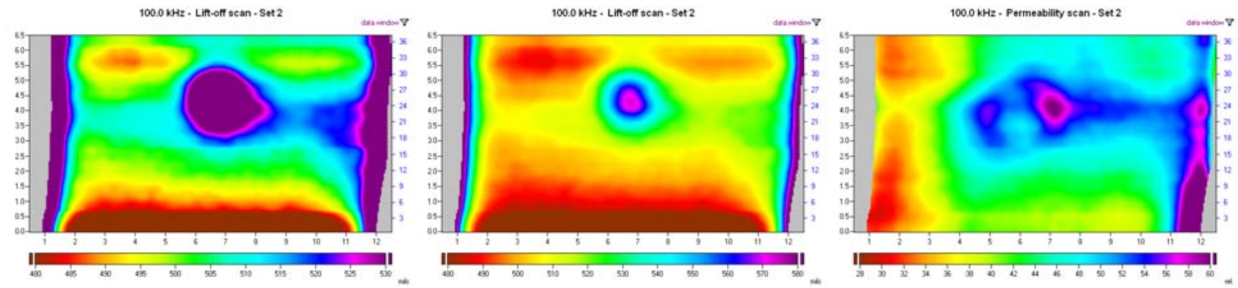

(a) (b) (c)

Figure 67. Mechanical damage scan images for (a and b) lift-off [in two different color scales] and (c) permeability for a VWA001 MWM-Array having a 1-in drive-sense gap.

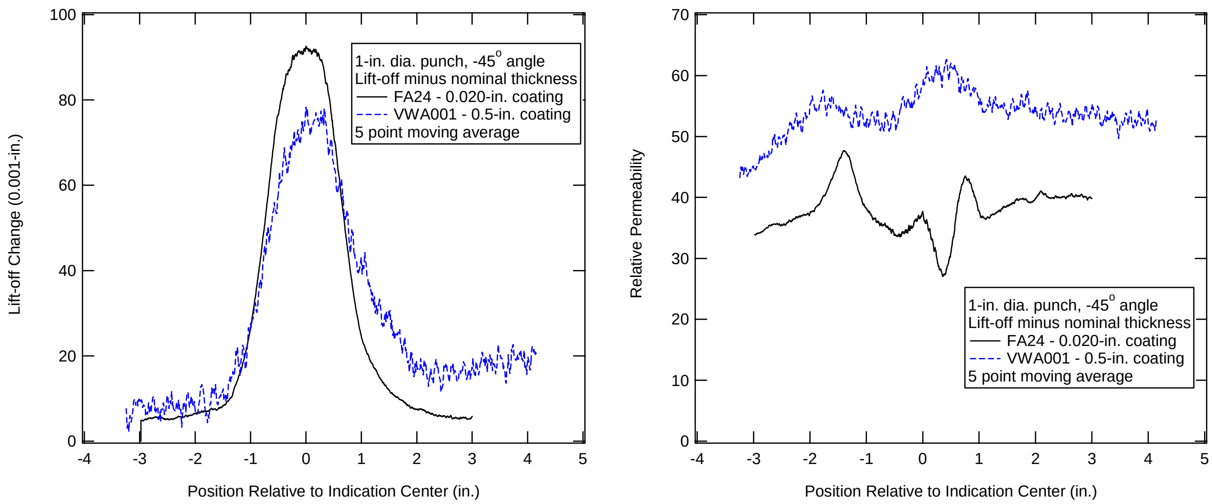

Figure 68. Comparison plots of the lift-off change (left) and relative permeability (right) for FA24 and VWA001 sense elements that pass over the center of the mechanical damage region.

Several scans were also performed over a region on the outer surface of the 16-in. diameter pipeline section. This region included a small (< 0.5-in. diameter) area of mechanical damage as shown in Figure 69. Two 0.010-in. plastic shims were attached on to the sensor with double-sided tape (each 0.003-in.) and two pieces of 0.010-in. plastic were placed on the surface of the pipeline section. As shown in Figure 70, the mechanical damage appears as a change in both the lift-off and permeability.

Figure 69. Area of mechanical damage on the external section of a pipe section.

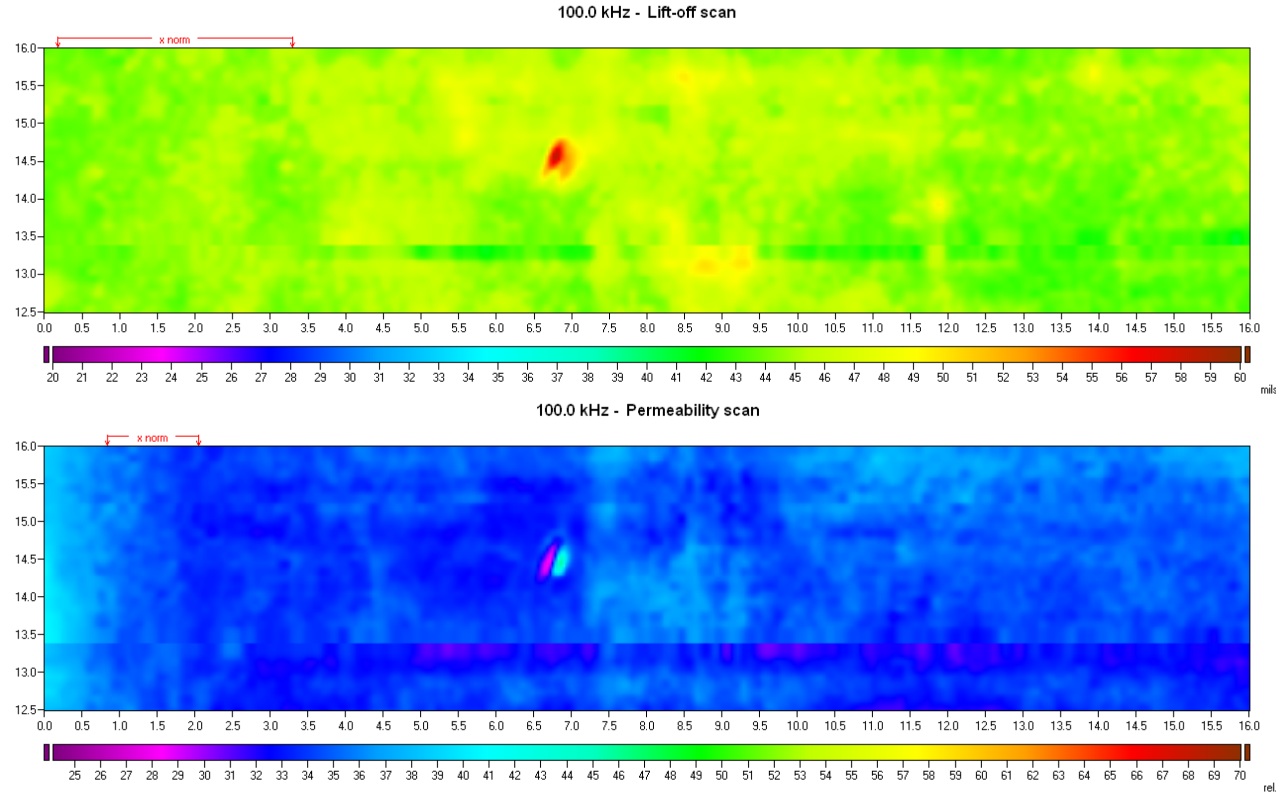

Figure 70. Lift-off scan image (upper) and permeability image (lower) of the region of external mechanical damage using an FA24 MWM-Array through a 0.046-in. coating.

Measurements were also performed on a 24-in. diameter pipeline section that included a large plain dent. Figure 71 shows the pipe section and the dent. The dent was at least 1-in. deep at the center and deformed the pipe wall over an area several inches in diameter. This set of measurements was performed with the VWA001 with a 1-in. drive gap. The prototype pipeline scanning fixture was used; the wrap-around sheet was not used and a two-inch layer of foam was placed behind the sensor array and used to hold the array against the coated pipe surface by hand. An air-shunt calibration was performed and the data was processed using permeability/lift-off measurement grids.

Figure 72 shows property images obtained with the VWA001 through a 0.25 mm (0.010-in.) semi-rigid insulating sheet. Even though a drive-sense gap of 25.4 mm (1.0-in.) is relatively large for such a thin coating, the nominal coating thickness of approximately 0.25 mm (0.010-in.) is obtained. Similarly, Figure 73 shows property images obtained with the VWA001 through a 12.7 mm (0.50-in.) semi-rigid insulating sheet of Neoprene rubber. Far from the damage the lift-off is approximately 12.7 mm (0.5-in.), consistent with the nominal coating thickness. For both coatings, the region of mechanical damage appears as both an increase in the effective lift-off and increase in the relative permeability over a region that is several inches in diameter. The change in lift-off indicates that the depth of the damage is at least 25.4 mm (1.0-in.). This is not the true depth since the measurement grids assumed a planar material geometry and did not account for the geometry of the dent. However, based on other work this depth is an underestimate of the actual depth of the damage. In the center of the flaw, the data no longer falls on the measurement grids and the property estimates are less reliable; this is most apparent in the 100 kHz data. On the left side of the mechanical damage there is a small decrease in the relative permeability that may be associated with residual stresses in the pipe wall.

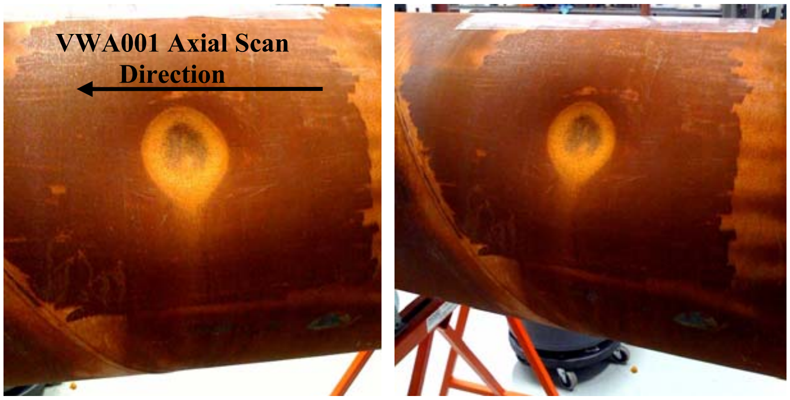

Figure 71. 24-in. diameter pipe section with plain dent. The scan directions for the VWA001 and FA24 MWM-Arrays are indicated.

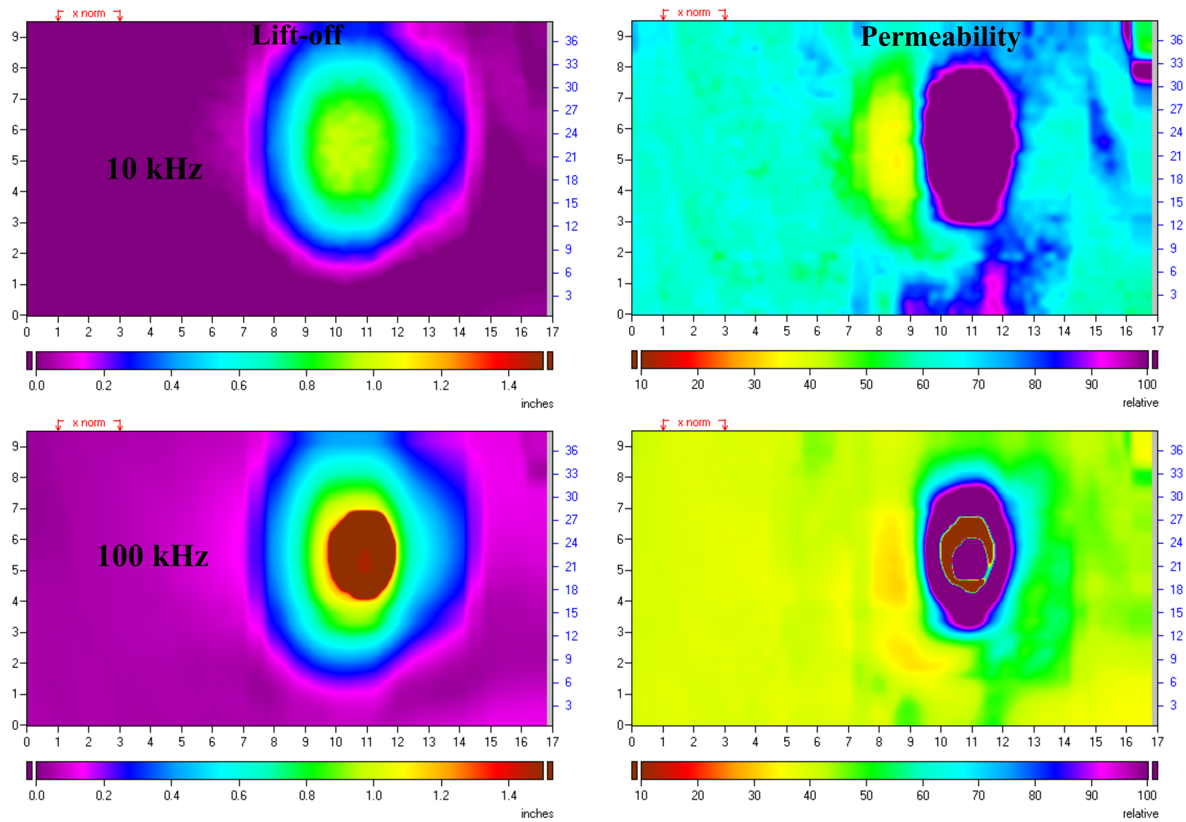

Figure 72. Effective property images obtained with a single pass of a VWA001 with a 25.4 mm (1.0-in.) drive-sense gap and a 0.25 mm (0.010-in.) thick coating.

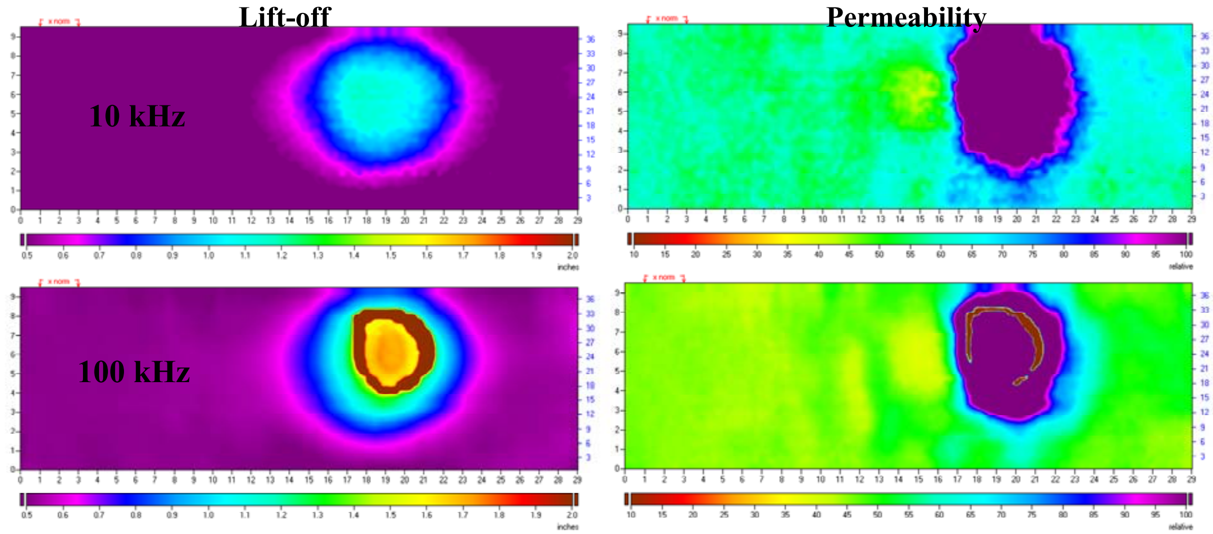

Figure 73. Effective property images obtained with a single pass of a VWA001 with a 25.4 mm (1.0-in.) drive-sense gap and a 12.7 mm (0.50-in.) thick coating.

Figure 74 contains a plot of the effective for several channels with both coating thicknesses. Note that the channel number is indicated on the right side of each of the scan images in Figure 72 and Figure 73. Channels on the lower portion of the mechanical damage are plotted and show the gradual increase in lift-off associated with the damage. Channel numbers that passed over the center of the damage were not plotted since the data points over the center of the damage did not fall on the measurement grids and the property estimates are not robust. However, these plots show that the measurement procedure, with an air-calibration, correctly provides the nominal coating thickness and the shape of the plots of the mechanical damage are similar for both coating thicknesses. These images were obtained with a single scan of the VWA001 over the pipeline surface and the actual measurement time was very fast (less than a minute) for creating these images.

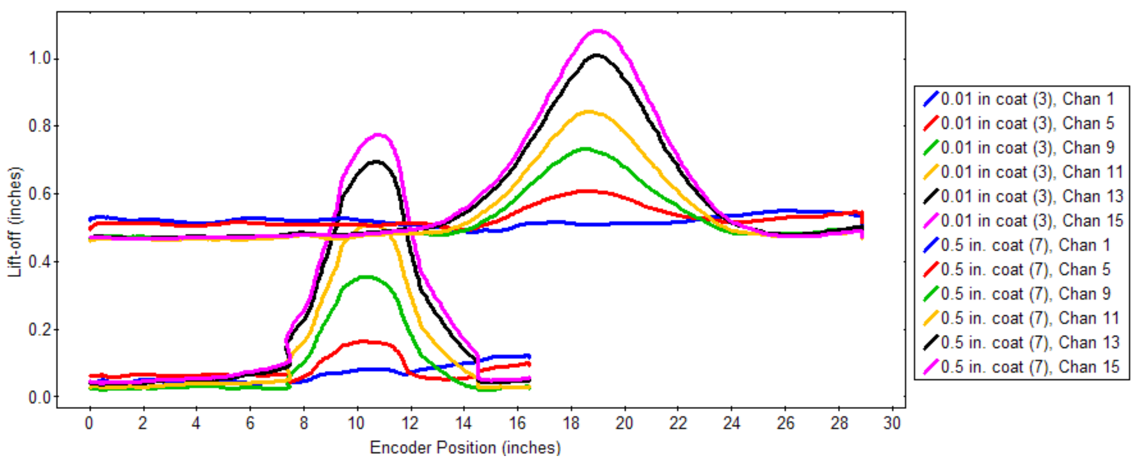

Figure 74. Effective lift-off plots for several channels for two coating thicknesses at 631 kHz.

6.4.3 Imaging of Pitting Damage

Another inspection application that can use the MWM technology is the detection and mapping of pitting corrosion under very thin coatings in pipeline materials. Although the main focus of the corrosion under insulation effort was for detection of generalized corrosion damage under thicker coatings, the inspection application for pitting damage represents a near-term commercialization opportunity that can help with transitioning the MWM-Array technology into the field. In this application, one of the main hurdles for fielding this technology is demonstrating the capability to meet API specifications.

To demonstrate the capability of the imaging MWM-Arrays to perform this type of inspection through coatings, a 10 foot long, 6 inch OD, and 0.4 inch wall thickness pipe section at JENTEK was used as a test specimen. The relevant flaw size of interest is determined by API Specification 16C, section 6.3.6.9, which describes criteria for inspection according to ASTM standard E709, which is a Guide for Magnetic Particle Inspection. The API specification requires a capability to detect surface breaking flaws with a major dimension of at least 1/16-in. Accordingly, a small flaw, representing the typical size of a corrosion pit, was made on the pipe external surface using a 1/16 – in. drill bit. The flaw depth was less than 1/16-in.

For the inspection, an FA28 MWM-Array, mounted on a manual scanning fixture, was used for inspection of pits. Two 0.010-in Mylar shims were placed over the circular flaw to simulate the presence of a coating. The measurement procedure involved ranging with the MWM-Array in air and then on the part; this sets the gain parameters for some of the amplifiers within the instrumentation. An air-shunt calibration was then performed. Multiple scans were performed over the region containing the pit. The impedance data obtained with the FA28 MWM-Array was converted into an effective lift-off and magnetic permeability using measurement grids. These measurement grids used an assumed value of 3.75 %IACS for the steel. More accurate inspections could incorporate measurements that perform a full three-unknown multivariate inverse method to determine a more accurate value for the conductivity and baseline permeability, but for basic field measurements an assumed value for the conductivity should be adequate.

Figure 75 shows representative scan image results at 251.1 kHz using an FA28. The pit/flaw appears as a local increase in the lift-off and a local change in the permeability as well. Other than adding the shims to simulate a surface coating, there was no other preparation of the pipe surface. The pipe surface was somewhat rough and dirty, which is indicated by the background variations in the properties of the images. Some of the background noise created due to the surface roughness of the pipe sample was suppressed by applying a threshold in the image.

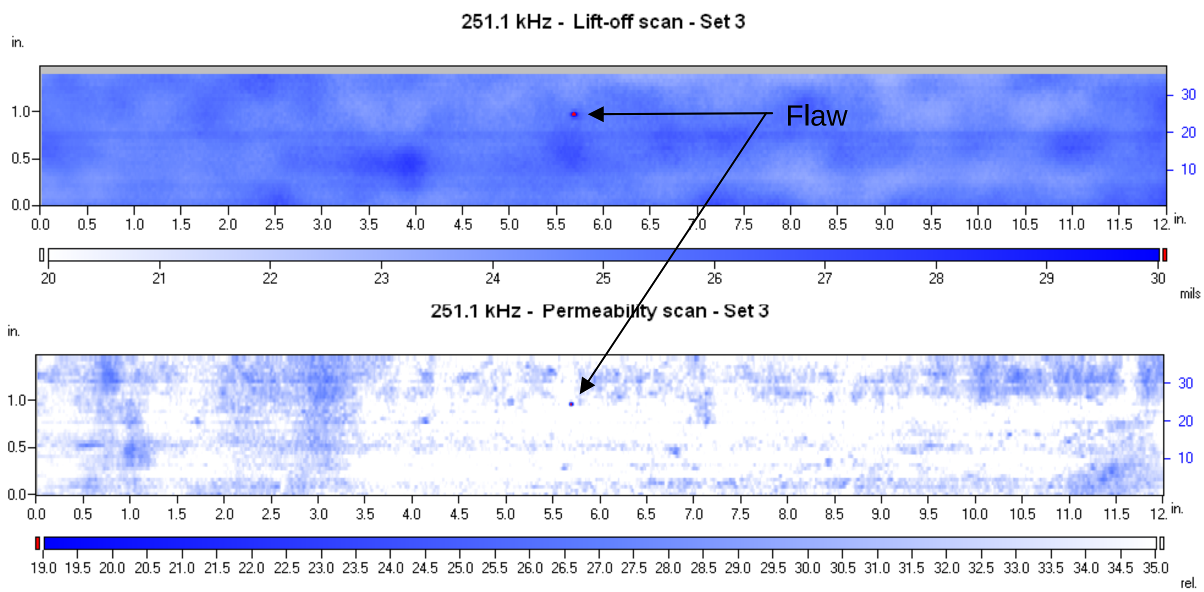

Figure 75. FA28 lift-off (upper) and permeability (lower) scan images at 251.1 kHz. Two 0.010-in. thick clear Mylar shim were placed over the manufactured pit to simulate presence of a coating.

Figure 76 contains B-scan plots of the response of the FA28 channel that passed over the flaw/pit. The background variation in the lift-off and permeability due to surface roughness and material property changes are evident. However, there is a sharp local increase in the lift-off and a local reduction in the permeability associated with the presence of the flaw/pit. This is consistent with the detection of wide-area corrosion under thick insulation where changes in both properties are present when local material loss is present. Note that the average lift-off is approximately 0.025-in., which is larger than the nominal coating thickness of 0.020-in. since the MWM-Array have a nominal thickness and there may be a slight air gap between the nominal coating and the pipe surface.

Note that data was acquired over a wide frequency range of 10 – 631 kHz. The lift-off responses at intermediate frequencies around 250 kHz provided the most accurate measurements of the pit dimensions and the least amount of measurement noise. In order to able to perform this type of inspection in the field, it is recommended that a shape filter algorithm be applied to both the lift-off and the permeability to better show the presence of the local pit. It also appears that to support field inspections reference measurement on flat or curved plates with discrete flaws would be necessary. While imaging with the MWM-Array does not require standardization (or calibration) on such flaws, performance verification measurements on such flaws can confirm proper operation of the inspection system.

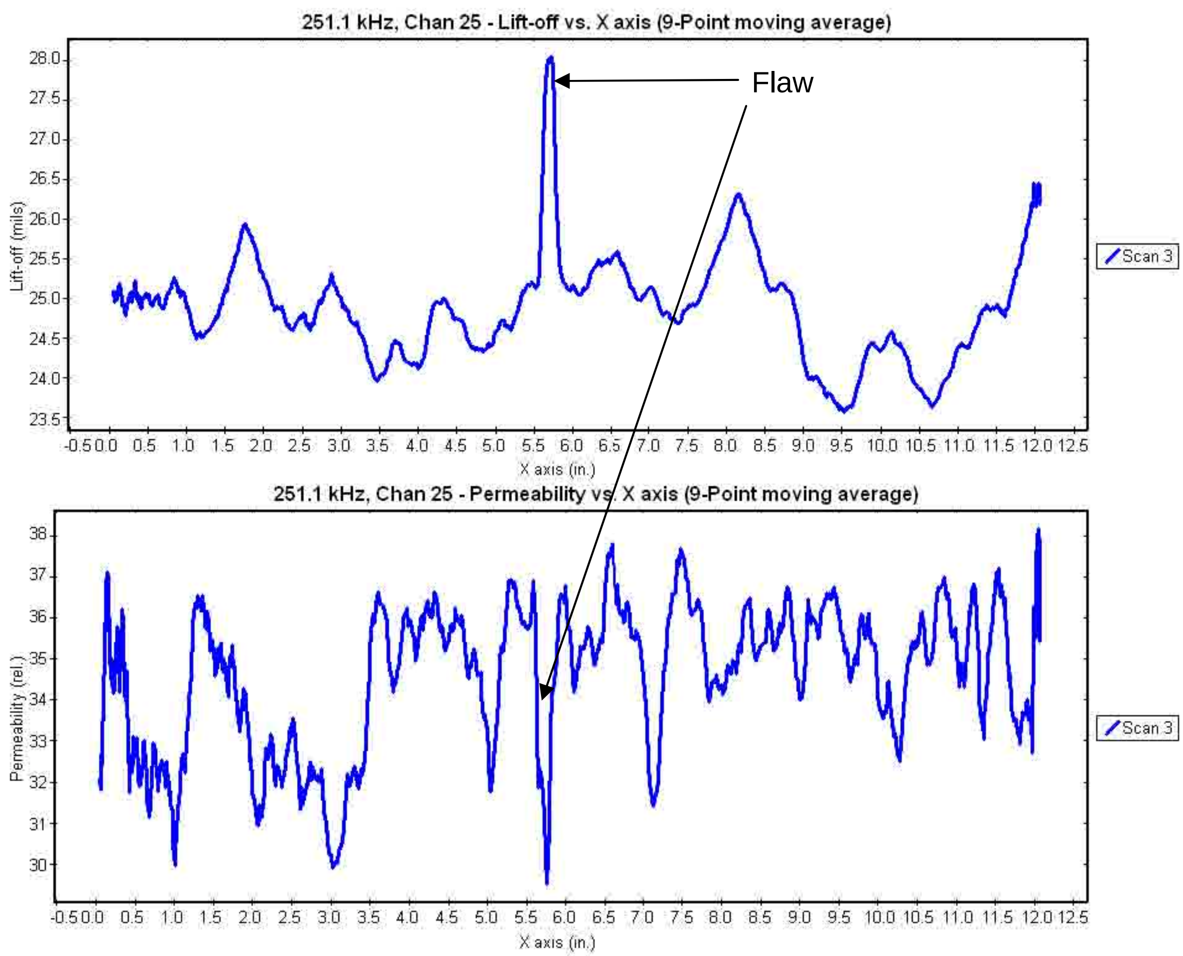

Figure 76. B-scan plots of the lift-off (upper) and permeability (lower) at 251.1 kHz for a single channel of the FA28 which passed over the flaw/pit.

6.4.4 *Stress Corrosion Crack Imaging*

Measurements were performed on a steel pipeline section that contains a region of SCC to demonstrate the capability of the MWM-Arrays to image SCC through thin and medium thickness coatings. This was a limited study aimed at establishing that the flexible eddy-current sensor arrays could image regions of SCC damage through coatings. The pipeline section for these measurements is shown in Figure 77(left) and has approximate dimensions of 18-in. x 13-in. x 0.33-in. For these measurements, JENTEK's very small-size FA28 and the small-size FA24 MWM-Array sensors were scanned over the section. A photograph and schematic for the FA28 are shown in Figure 3(a) and for the FA24 in Figure 3(b). Figure 77(middle) shows a photograph of the setup used to perform manual scans of the triangular plate. Shown are JENTEK's 39-Channel impedance instrument, host laptop computer, and the triangular plate with a lined Mylar sheet laying on it to assist in registering the position of the multiple scans. More shims were added to simulate thin coatings and thicker Neoprene coatings were used to simulate moderate and thicker coatings. Figure 77 (right) shows a photograph of the probe electronics/scanning cart assembly showing the position encoder and foam-backed sensor, which conforms to the curvatures of the plate. The excitation frequencies used for both sensors was 100 kHz. An air-shunt calibration was performed.

Figure 77. Photographs of (left) the steel pipeline section having clusters of SCC damage, (middle) the scanning setup, and (right) the MWM-Array sensor cart assembly.

The response of each sense element was processed using JENTEK's multivariate inverse methods to provide a material electrical conductivity and the sense element lift-off (proximity to the conducting material surface). These inverse methods use measurement grids, which are precomputed databases that relate the sense element response to two or more unknown parameters that are to be determined. For crack detection in this steel, the magnetic permeability was assumed to be constant at a relative permeability of 50; the measured (or "effective") electrical conductivity then provides information about the material condition, such as the presence of cracks. Note that the cracks interrupt the flow of the induced eddy-currents and decrease the effective electrical conductivity of the material. The lift-off provides information about the surface topology, as well as the coating thickness. Figure 78 shows a representative plot of data from one of the FA24 sense elements on a measurement grid for four different coating (shim thicknesses). As the lift-off changes, the data groups follow a line of constant conductivity.

Figure 79 shows a series of conductivity scan images obtained with a FA24 MWM-Array over coating thicknesses ranging from 0.010-in. to 0.330-in. The region of SCC damage appears as a reduction in the electrical conductivity and is apparent on the left side of the images. For thin coatings, less than approximately 0.080-in. in thickness, the images appear to show individual cracks within the SCC clusters. However, as the coating thickness gets larger the responses from nearby cracks overlap and it is more difficult to resolve individual cracks. The SCC clusters remain visible with this sensor array even for relatively thick coatings of order 0.25-in. For even thicker coatings, of order 0.330-in. the SCC clusters are visible but there is a noticeable degradation in the image quality as individual pixels become apparent. This is a result of filtering the data to only plot measurement data that falls on the measurement grid; for thick coatings, where "thick" is relative to the sensor dimensions, the measurement grids become narrow and noise in the measurement can lead to the data not falling on the measurement grid.

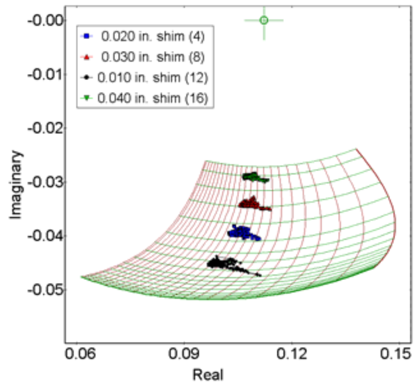

Figure 78. FA24 conductivity/lift-off measurement grid with data as the coating/shim thickness is varied.

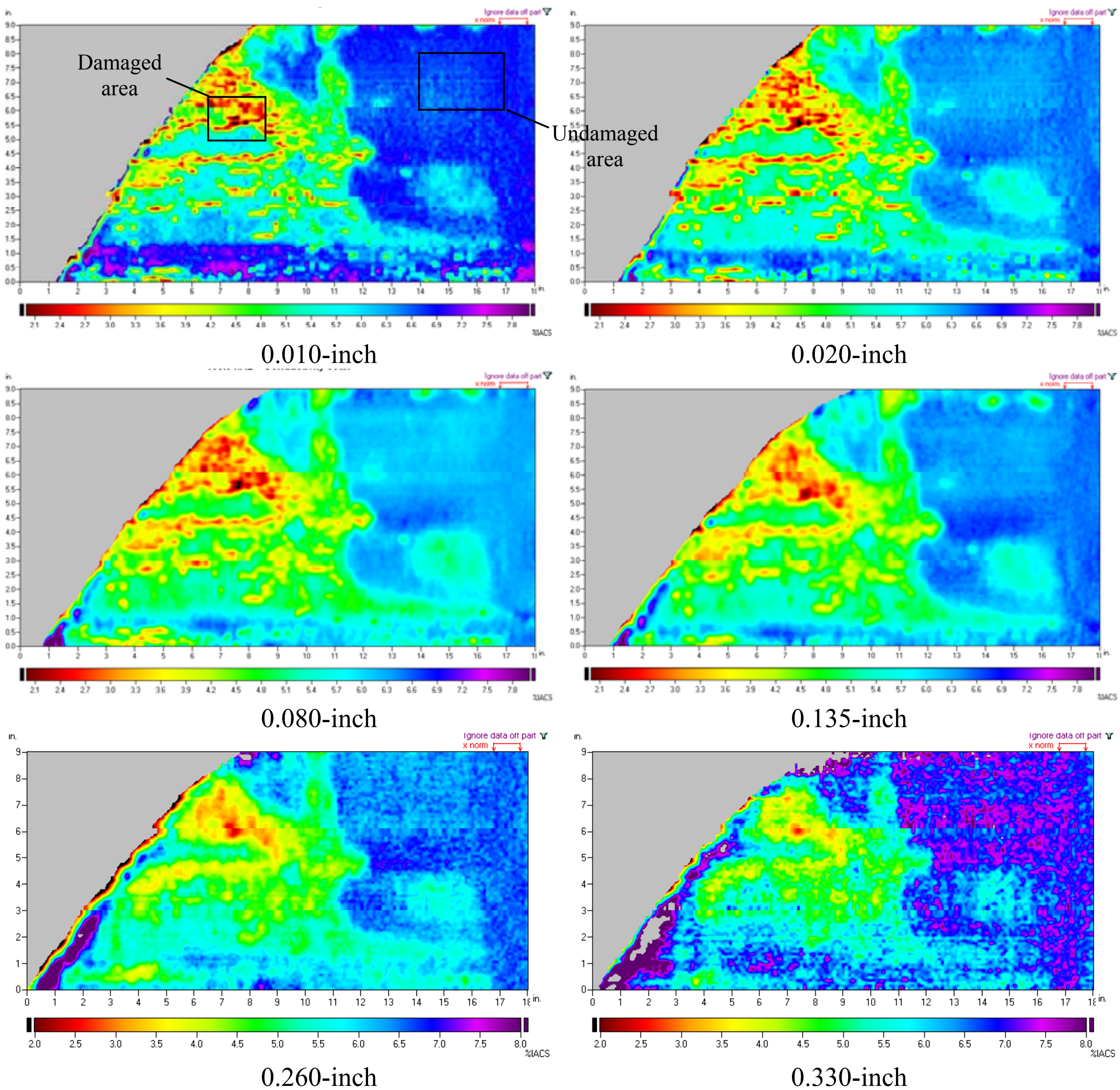

Figure 79. FA24 conductivity images of the steel plate sample for several coating thicknesses.

Figure 80 shows a similar series of conductivity scan images obtained with a FA28 MWM-Array. The smaller size of the FA28 and the smaller gap between the drive winding and the sense elements, compared to the FA24 makes it more suitable for obtaining very high spatial resolution images of damage through relatively thin coatings. This high resolution may be required for obtaining accurate crack depth estimates; under a separate program crack depth estimation algorithms are being developed. For this sensor, the scan image degrades when the coating thickness is approximately 0.060-in. and greater, which is consistent with the sensor array having smaller dimension than the FA24.

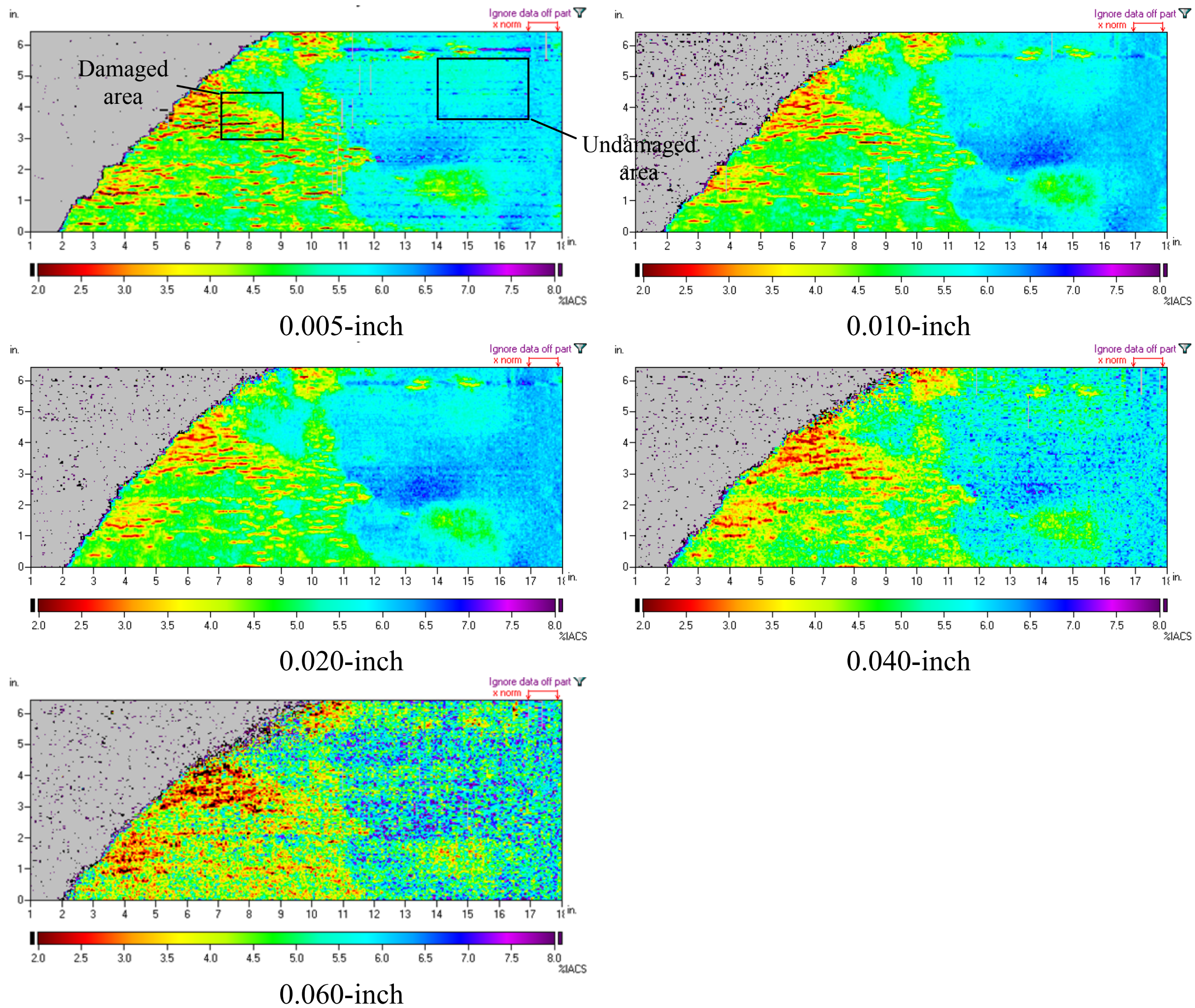

Figure 80. FA28 conductivity images of the steel plate sample for several coating thicknesses.

To quantify the variation in sensitivity to SCC with coating thickness, portions of the images were further analyzed. In particular, for the FA24 images (Figure 79) the average conductivity of an undamaged background region (spanning 14 to 17-in. in the *x* direction and 6 to 8-in. in the *y* direction) and the minimum conductivity of a damaged region (spanning 6.5 to 8.5-in. in the *x* direction and 5 to 6.5-in. in the *y* direction) were obtained. This damage region contains a distinct SCC cluster. Similarly, for the FA28 images (Figure 80), the average conductivity of an undamaged background region (spanning 14 to 17-in. in the *x* direction and 3.5 to 5.5-in. in the *y* direction) and the minimum conductivity of a damaged region (spanning 7 to 9-in. in the *x* direction and 3 to 4.5-in. in the *y* direction) were obtained.

Figure 81 shows a plot of the resulting effective conductivity variation with coating thickness. The baseline conductivity is essentially constant with thickness for both sensors; the small variation in the conductivity is probably due to the assumed relative permeability being slightly in error. A reference calibration using measurements at two different lift-offs (or coating thicknesses) would reduce this effect. Figure 81 also shows the reduction in conductivity associated with the SCC damage. The conductivity is lowest for the thinner coatings. As the coating thickness increases, the minimum conductivity increases as the sense elements average the response of the SCC damage with nearby undamaged material. As the coating thickness becomes large relative to the dimensions of the sensor array, the minimum conductivity value for the damaged region becomes less reliable, probably as a result of the narrowing of the measurement grid.

Figure 82 shows a plot of the ratio of the minimum conductivity of the SCC damage region to the baseline conductivity. This type of a ratio may be suitable for accounting for slight conductivity variations along pipeline sections to improve estimates of SCC damage condition. The value is lowest for the thinnest coatings and then increases to a maximum value of about 0.35, which appears to reflect the nominal SCC damage. As expected, since the FA28 has smaller dimensions than the FA24, it reaches this maximum value for smaller coating thicknesses.

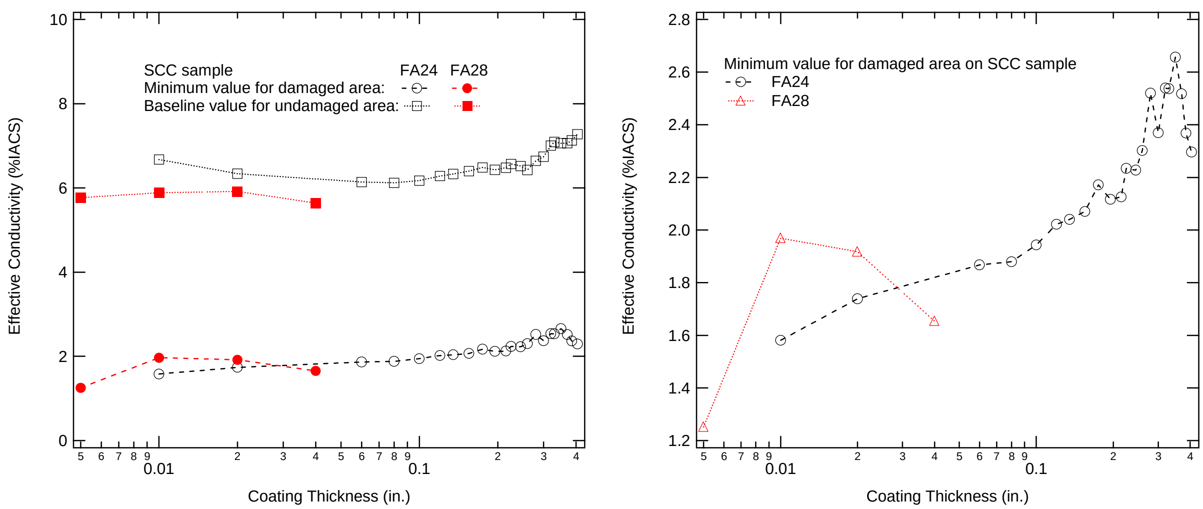

Figure 81. Effective conductivity variation with coating thickness for bothundamaged and SCC damaged areas.

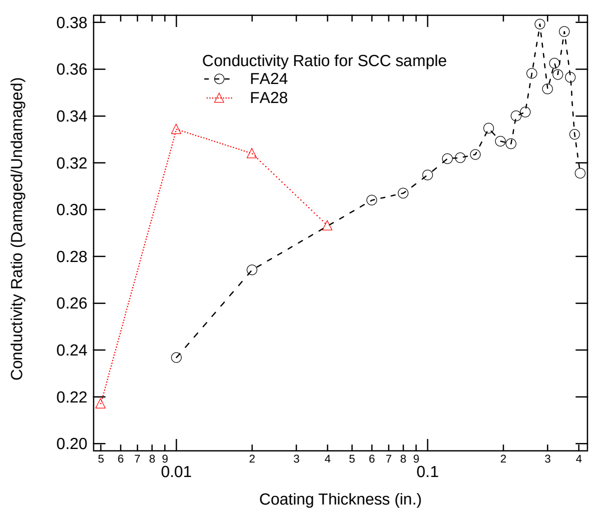

Figure 82. Effective conductivity ratio as the coating thickness is varied.

As part of the field demonstration measurements and to help generate feedback for field hardening requirements, Applus/RTD worked under a subcontract on this project and used a JENTEK GridStation system to perform field measurements of SCC during routine service inspections. As an two Applus/RTD Engineers mapped nine pipe cutouts approximately 12 meters long and 36 inches in diameter. It is our understanding that the coatings had been removed from the cutouts. This allowed the use of the small spatial wavelength FA28 MWM-Array for obtaining high spatial resolution images of the damage. A plastic coating/wear layer was placed between the MWM-Array and the pipe surface to prevent damage to the sensor during the measurements and to act as a guide to align multiple passes of the MWM-Array over the test section as the property images are built. The plastic layer is typically 0.010-in. thick and, as far as the MWM measurement is concerned, behaves the same as a typical barrier coating. Using this system approximately 200 SCC crack colonies were mapped, analyzed and compared to the actual SCC that was made visible by Magnetic Particle Inspection.

Figure 83 shows an example image of an SCC cluster. In this example the color scale for the effective property obtained with the GridStation software is adjusted to highlight the presence of the cracks and to suppress background variations in the response. The use of this type of color scale display has previously been shown to be effective at highlighting the presence and location of cracks within SCC clusters. Feedback from this type of study indicated the need for a longer cable between the impedance instrument and probe electronics, sealed probe electronics, and a more robust scanning fixture.

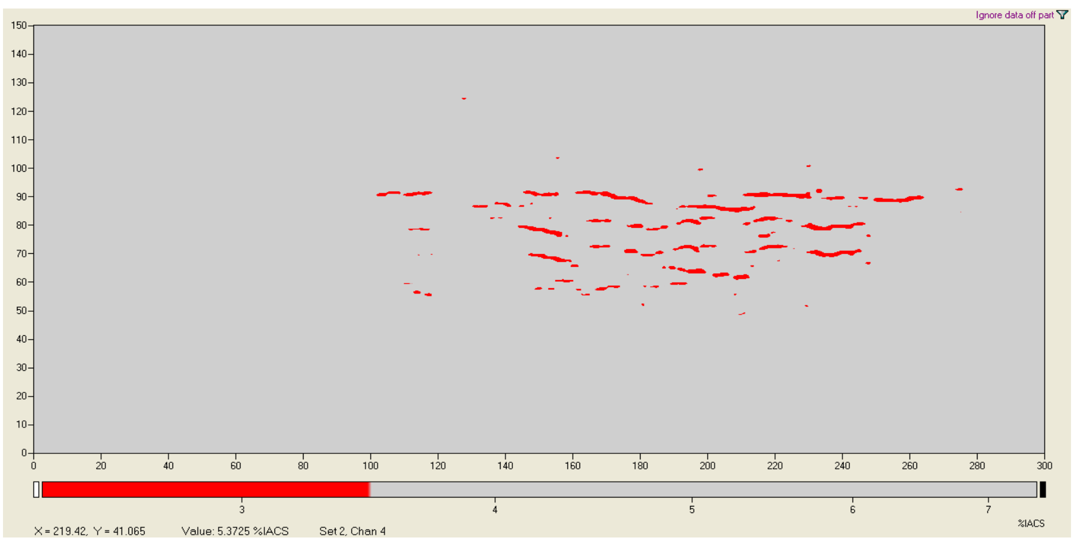

Figure 83. Representative image of SCC clusters from pipeline samples scanned by Applus/RTD.

6.4.5 Far-Surface (Internal) Corrosion Imaging

For inspecting through the thickness of the steel walls and also for inspecting through magnetic and/or conducting coatings or liners, low excitation frequencies are needed. Example barrier layers include aluminum weather jacket layers and corrosion resistant alloys used as internal liners. Frequencies of 1-10 kHz can be used for inspecting through nonmagnetic conducting layers but lower frequencies of order 30 Hz are needed for inspecting through the magnetic layers and the steel wall thickness. Experiments showed that the VWA001 can be operated down to approximately 1 kHz, but to achieve the low operating frequencies it is better to use sense elements that respond directly to the magnetic flux, such as magneto-resistive (MR) sensors or Hall effect devices, in place of inductive loops that respond to the time rate-of-change of the magnetic flux.

A prototype 37 channel MR-MWM-Array was made available for testing in this program and used to investigate the independent measurement of lift-off, steel magnetic permeability, and steel wall thickness using multiple frequency measurements. This array has 37 MR sense elements, as shown in Figure 84(left), and is designed to fit within a large (12-in. x 6-in.) drive winding as shown in Figure 84(right). The array has a basic geometry similar to the FA24 used for high frequency/thin coating applications, but uses a larger drive winding. Through minor hardware and software adjustments, the current instrument's low frequency range was extended to 31Hz; previously, the lowest frequency for the instrument was 100 Hz. Note that at 30 Hz, the skin depth for a steel having an electrical conductivity of 5%IACS and relative permeability of 70 is approximately 6.35 mm (0.25-in.). If the measurement noise is low enough, this suggests that the instrumentation could be sensitive to a wall thickness of order 0.5-in.

In principle multiple frequency data, taken simultaneously over a 31 Hz to 3.16 kHz range, permits estimation of the wall thickness, relative permeability, wall thickness of the steel as well as the sensor lift-off. However, since the precomputed response lattices are multi-valued over the property ranges of interest, different estimation results can be obtained depending upon the frequencies and approach used. By separating the multiple unknown inverse method into two problems each having fewer unknowns, robust property estimates were obtained. Instead of using a wide range of frequencies to simultaneously estimate lift-off, thickness and permeability, it is better to use high frequencies to accurately estimate the liftoff and then lower frequencies to estimate the thickness and permeability of the material given the previously estimated liftoff.

To demonstrate an initial scanning capability, a series of measurements were performed on flat 4340 steel plates having dimensions of 12-in. by 12-in. by 0.125-in. In two of these plates, as shown in Figure 17, five regions were machined on one side of the plate to represent areas of material loss. Although the MR-MWM-Array has large dimensions compared to the plate edge effects were not an issue if the sensor array was positioned near the center of the plate. Assuming the plate thickness and that the array was not over a flawed area, it was possible to use permeability/conductivity/lift-off lattices and multiple frequency measurements to determine a nominal plate conductivity of 8%IACS. Subsequent measurements used this electrical conductivity value so that the local plate thickness, permeability, and lift-off could be estimated.

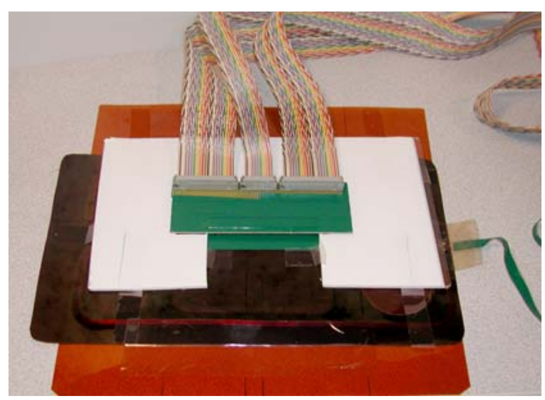

Figure 84. Photographs of a 37 channel MR sensor array (left) and the MR-Array within a large hand-wound drive winding (right).

Figure 85 through Figure 88 show representative images obtained for the multivariate inverse methods over the center material loss region which has a depth of 0.10-in. and a remaining plate thickness of 0.025-in. A 0.25-in. thick Neoprene layer was used as a simulant coating. The horizontal axes provide a measurement number since the measurements were taken at discrete intervals of approximately 0.25-in. over the plate surface. The vertical axes provide the sense element number. Frequencies of 1.0 and 2.5 kHz were used for the high frequency lift-off estimation while frequencies of 31, 100, and 316 Hz were used for the low frequency thickness estimation. In each set of images, the thickness decreases from the nominal plate thickness of 0.125-in. to approximately 0.050-in., which is approaching the thickness of the material loss region. The lift-off ranges from approximately 0.34-in., which includes the Neoprene thickness of 0.25-in. and the internal lift-off of the sense element in the array of 0.10-in.) to 0.44-in. when the material loss is on the upper surface of the plate nearest the sensor. As shown in Figure 86 and Figure 88, when the material loss is on the bottom surface of the plate (the side opposite the sensor array), the plate thickness shows the material loss but the lift-off is relatively constant. **This series of measurements demonstrates the capability of the MR-MWM-Arrays to independently determine near-surface and far-surface material loss,** for 0.125-in. thick steel layers.

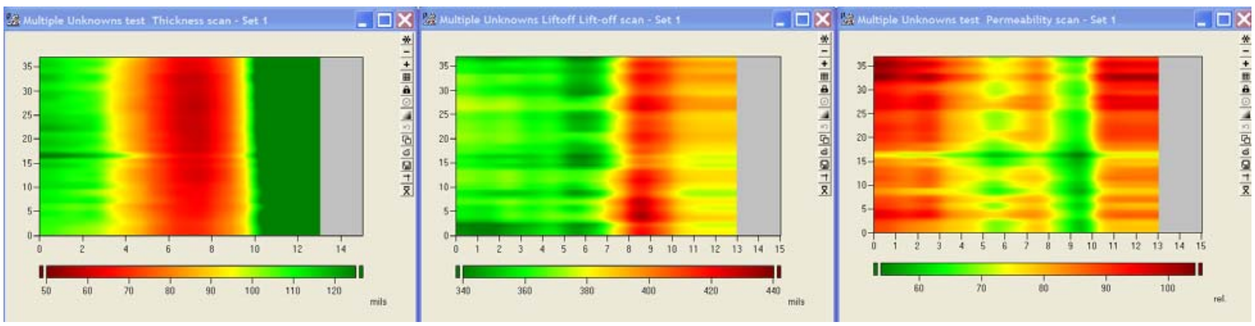

Figure 85. Representative property images for vertical slots in the upper surface of the plate showing plate thickness (left), lift-off (middle), and relative permeability (right).

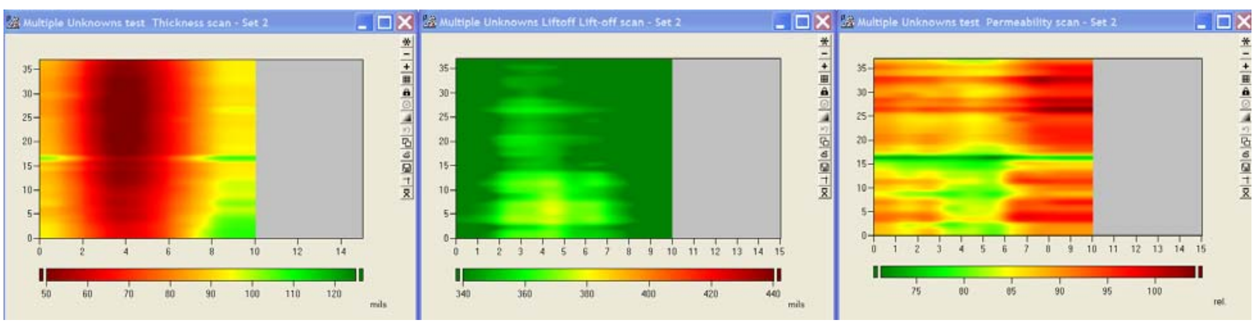

Figure 86. Representative property images for vertical slots in the bottom surface of the plate showing plate thickness (left), lift-off (middle), and relative permeability (right).

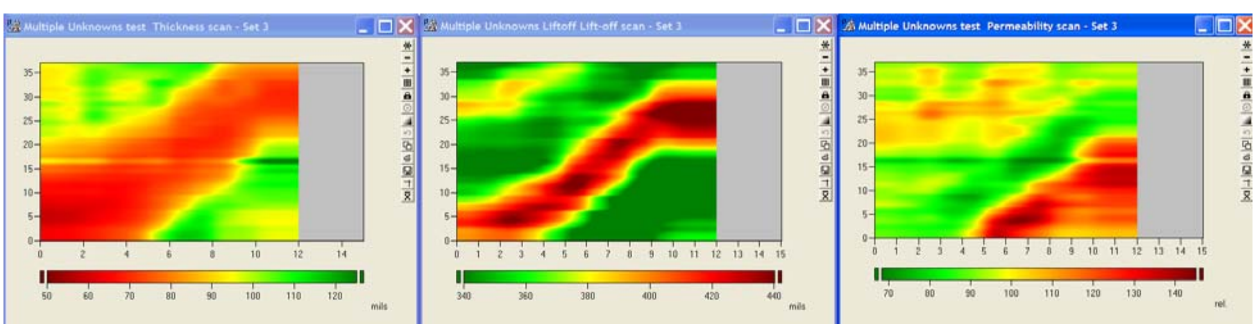

Figure 87. Representative property images for diagonal slots in the upper surface of the plate showing plate thickness (left), lift-off (middle), and relative permeability (right). (Note that the elongation of the diagonal at the ends is due to scanning in the middle in larger increments than on the ends.)

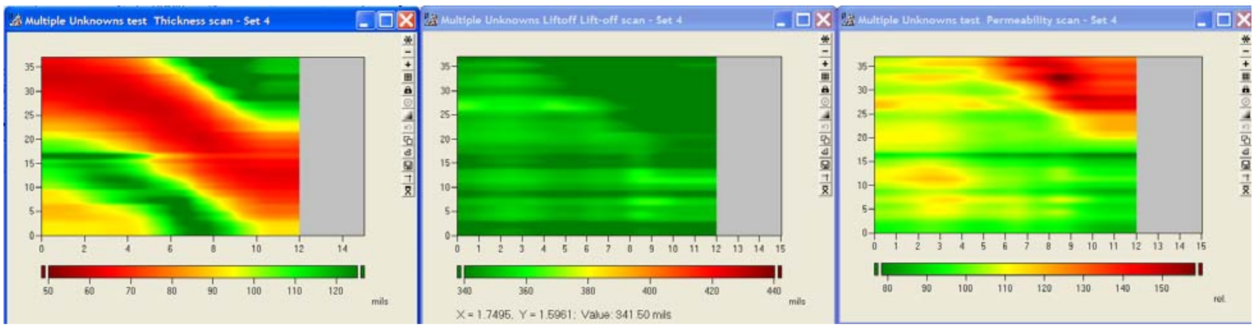

Figure 88. Representative property images for diagonal slots in the bottom surface of the plate showing plate thickness (left), lift-off (middle), and relative permeability (right).

Measurements were also performed on larger steel plate samples that did not contain machined flaws. Following the method described above, the thickness, permeability, and lift-off were estimated using an assumed value for the electrical conductivity. The estimated plate thickness is shown in Figure 89 though Figure 90 at several positions on the plates; these thickness values are in reasonable agreement with the nominal thickness and were relatively consistent for each sense element. Based on our measurements, the appropriate value for the electrical conductivity decreased with increasing plate thickness as 10%IACS for the 0.125-in. plate, 9%IACS for the 0.19-in. plate, and 7.5%IACS for the 0.25-in. plate. All of the measurements here used an air calibration and a reference calibration may help to minimize any dependence on the assumed conductivity value.

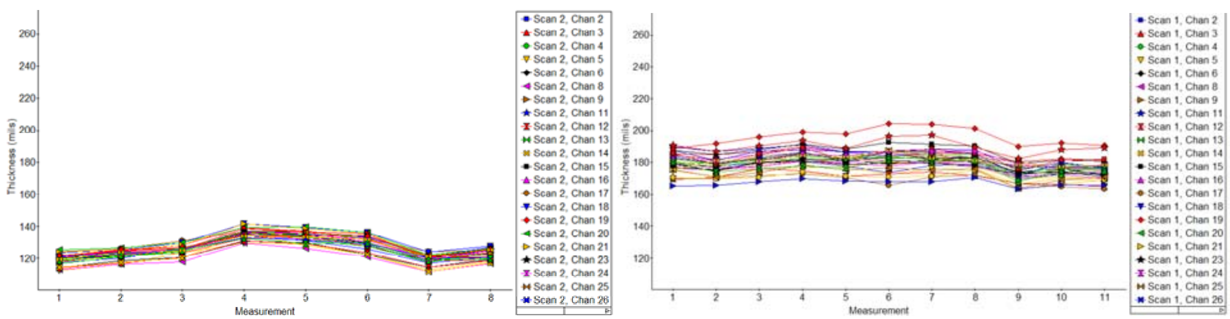

Figure 89. Plate thickness estimates at several measurement locations for (left) a 0.125-in. steel plate assuming an electrical conductivity of 10%IACS and (right) a 0.19-in. steel plate assuming an electrical conductivity of 9%IACS.

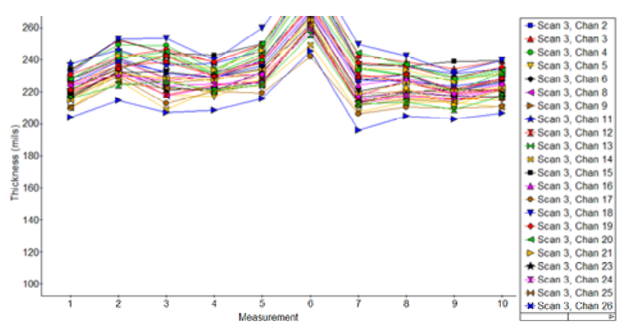

Figure 90. Plate thickness estimates at several measurement locations for the 0.25-in. steel plate assuming an electrical conductivity of 7.5%IACS.

Figure 91 shows the result of measurements on the 0.125-in. steel plate with and without an extra 0.5-in. layer of Neoprene. While the permeability estimate appears to be more reliable for the 0.25-in. layer of insulation, **the plate thickness estimate is independent of the presence of the extra Neoprene**. These results are consistent with the results of the VWA001; the gap between the drive and the MR sense element array is approximately 22 mm and, based on a 25.4 mm (1.0-in.) gap with the VWA001, reasonable results are expected for coatings thicknesses of at least 1.0-in. Ongoing work is aimed at improving this measurement capability for thicker steel walls.

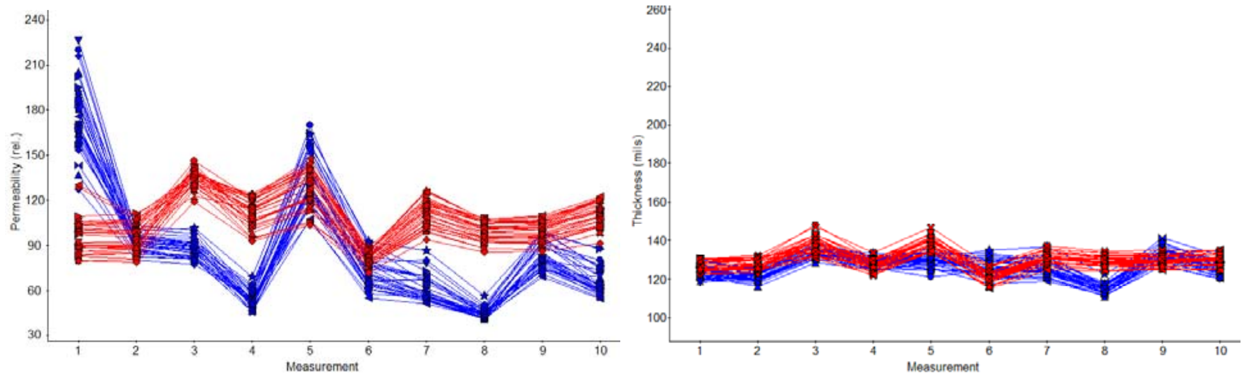

Figure 91. Permeability (left) and thickness (right) of the 0.125-in. plate with a 0.25-in. (red) or 0.75-in. (blue) Neoprene insulation layer.

For practical implementation of an MR-MWM-Array in pipeline inspections, instead of using a flat, rigid array of sense elements, a flexible array similar to the VWA001 design, would permit inspection of pipelines having different diameters. This led to the fabrication of the next generation version of the MR-MWM-Array, which has a linear array of 12 magnetoresistive (MR) sensors placed 6.35 mm (0.25-in.) apart. Each sensor provides three outputs corresponding to three orthogonal field directions. Since this leads to 36 sensor outputs, JENTEK's standard 37-channel impedance measurement instrumentation can be used. The same drive winding used with the prototype MR sensor array was used the new MR array. Figure 92 shows a photograph of the next generation MR-MWM-Array.

Figure 92. Photograph of the next generation MR-MWM-Array with the old (dual rectangle) drive winding placed on a flexible substrate of 0.25-in. thick Neoprene.

The sensor array configuration with a separate drive winding and sense element array is similar to that used with the VWA001 and VWA003. However, the capability to measure three magnetic field directions simultaneously provides new challenges and potentially complementary information about detected flaws. The magnetic field created by the drive winding has a large component normal to the face of each sensor. This is the orientation used in the inspections with the inductive sense elements and the MR sensors act as absolute sense elements. The other two (tangential) components of the magnetic field are substantially smaller, with the field component in the direction of the array elements ideally zero; in these orientations the MR sensors act more like differential sense elements since the fields are small unless a flaw is present. The emphasis of the preliminary measurements has been on the response to the normal fields but ongoing work will test the response to the other field components as well.

To test the next generation MR-MWM-Array, one set of measurements were made on large steel plates (approximately 24-in. x 24-in.) that did not contain machined flaws. Using multivariate inverse methods, the thickness, permeability, and lift-off were estimated using an assumed value for the electrical conductivity. Measurements were taken using frequencies from 30 Hz to 1 kHz. The sensor array was placed inside one of the drive winding loops approximately 0.5-in from the central drive winding conductor. An air calibration was performed. These results are still being analyzed and will support follow-on R&D.

The flexible MR-MWM-Array of Figure 92 was then placed around a 4 ft long pipe section with internal flaws. This pipe section has an outer diameter of 6.625-in. and a wall thickness of 0.4-in. It has two rows of flaws machined into the inside surface to represent internal material loss, which was accomplished by drilling holes through the pipe on the opposite sides from the flaws. The flaws are located 90^{o} apart and have nominal diameters of 0.5 and 1.0 inches. The flaws have depths corresponding to 25%, 50% and 75% material loss, so that the remaining wall thickness is 0.3, 0.2, and 0.1-in., respectively.

Figure 93 shows photographs of the MR-MWM-Array wrapped around the pipe section, with a 0.25-in. thick layer of Neoprene used as the sensor array substrate and placed between the sensor array and steel pipe. The sensor array and drive winding were both flexible enough to wrap around the pipe section and conformed reasonably well to the pipe contour.

For measurements with the MR-MWM-Array on the pipe section, an extra layer of 0.25-in. thick Neoprene was wrapped around the sensor array to hold it in place as shown in Figure 94. A suitable scanning fixture was not fabricated for this prototype array so an image of the pipe properties was obtained by taking a set of measurements at discrete intervals of approximately 6.35 mm (0.25-in.) over the pipe surface. Frequencies from 30Hz to 1kHz were again used for the inversion, along with an air calibration. This data is also undergoing further analysis to support follow-on work.

Despite the differences in the absolute electrical property values, measurements of the MR-MWM-Array on the pipe section and application of the multivariate inverse methods yielded reasonable results. Images showed the wall thickness, pipe wall magnetic permeability, and sensor lift-off. Images were obtained for measurements taken over the 1.0-in. diameter internal material loss regions. The results were encouraging since they demonstrated the capability of the approach for simultaneously estimating multiple pipe wall parameters using only an air calibration. Ongoing work is aimed at reducing the measurement time for each location to demonstrate a scanning capability.

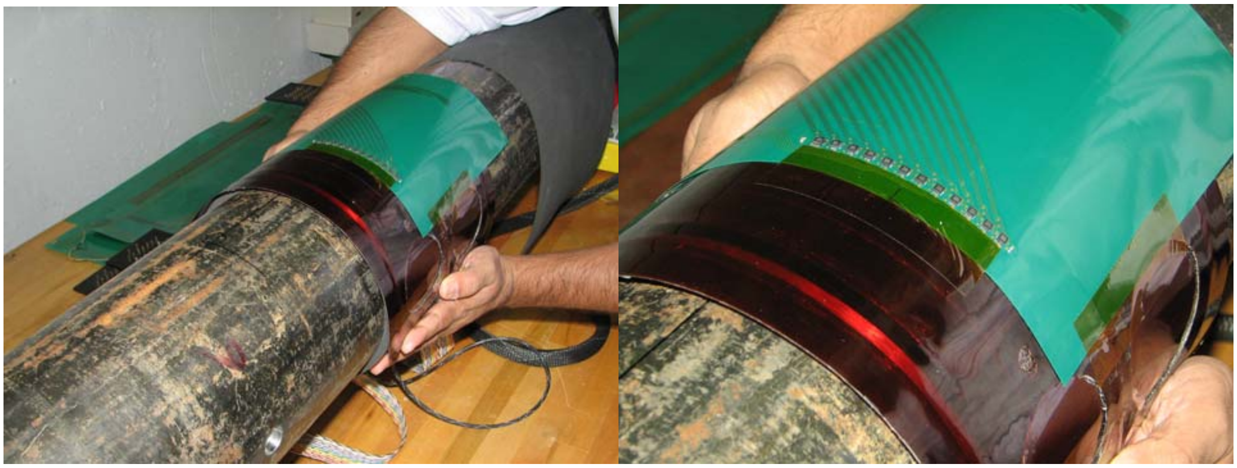

Figure 93. Photographs of the flexible MR-MWM-Array wrapped around a 6-in. diameter pipe section with several 25.4 mm (1-in.) diameter flat-bottom regions machine out of the inner surface.

Figure 94. Photograph of the flexible MR-MWM-Array wrapped around a 6-in. diameter pipe section with an extra layer of 0.25-in. thick Neoprene wrapped around the sensor array.

6.5 Technology Transition

Transitioning of this technology for in-service use in pipeline applications has several components. One component is a commercialization plan that reviews the technology status and inspection requirements for a variety of applications. Another component is the development of training information and standards since this information needs to be available in order for widespread adoption by the industry. Finally, preparing papers and presenting at conferences increases awareness of the technology throughout the industry. Each of these components is described below.

6.5.1 Commercialization Plan

In broad terms, the commercialization plan involves an initial demonstration of inspection capability for specific applications that can be made available to lead customers. This capability would be in the form of prototype inspection systems that can be purchased and leased systems would also be available. While these prototype systems are being used, the plan is to continue to harden the instrumentation, refine measurement and training procedures, and incorporate feedback obtained from the lead customers to provide a field-ready inspection capability. Since the same basic system can be used for multiple inspections, typically with a different sensor array being used for families of inspection applications, ongoing work is aimed at defining product configurations and remaining development requirements for the various applications.

To assist with transitioning this technology, a capabilities summary was drafted that is useful for planning and for discussions with service providers and end-users. This summary reviews both relatively mature technologies which should be suitable for near-term commercialization as well as those that are less-mature and require additional development. It also includes a review of the MWM technology and provides results for specific applications. The emphasis of the summary is on external inspection through coatings and insulation, but the basic technology can also be applied to in-line inspection (ILI) applications with suitable hardware modifications to integrate with an ILI platform. For several no-coating, very thin and thin coating applications, such as SCC, mechanical damage, near surface corrosion, and crack inspection, the technology is mature with capability demonstrations already performed and prototype systems available. For some applications, such as external corrosion and mechanical damage inspection through moderate thickness coatings (up to 1.0 or 1.5-in.), the capability has been demonstrated but further system refinement is required, such as redesign of scanners and sensor arrays to facilitate field-level inspections. For other applications, such as external corrosion inspection through thick coatings or SCC depth estimation, basic feasibility has been demonstrated through limited measurements. Basic feasibility has been also demonstrated for inspection through weather jackets and for through-thickness material loss estimates in steel, but substantial system improvements are required, such as implementation of very low frequency (< 100Hz) instrumentation and solid-state sensing elements.

6.5.2 Development of Industry Standards and Training Information

To help transition and establish a basis for the technology, a standard practice has been drafted for imaging of damage in metallic materials using flexible eddy current sensor arrays. The draft practice covers the use of model-based sensor arrays and is suitable for damage inspections with and without coatings and/or insulation between the sensor array and the metallic material of interest. The draft practice reviews factors that need to be considered as part of the examination procedure as well as standardization and calibration procedures along with the associated verification of the system performance for a particular application. The practice is generic enough to cover crack detection, material loss, and SCC imaging.

Once the standard is completed, the plan is to submit it to ASTM International for approval as an NDE procedure involving eddy current sensor arrays. ASTM International, particularly Committee E07 on Nondestructive Testing, is an appropriate standards organization since this committee is responsible for the maintenance of existing standards and development of new standards related to inspection methods. It is also our understanding that for specific applications the inspection requirements using this type of array will be specified in documents from other organizations, such as API. This will probably lead to other standards development activities, but the initial standard should help to establish the use of imaging eddy current sensor arrays as a mature technology suitable for field implementation.

For the training manuals, JENTEK has general manuals that cover basic operation of the equipment and software. Presentation slides also cover the fundamentals for eddy current sensing methods and the use of Grid Measurement Methods. Specific manual and presentation information will be generated as necessary for the inspection of steel pipeline walls. This includes information about the scanning fixtures, selection of the sensor array configurations and operating frequencies, software configurations, measurement grids being used, and considerations for estimating damage conditions.

6.5.3 Increased Industry Awareness of the MWM-Array Technology

Ongoing work is aimed at increasing awareness of the capabilities of imaging eddy current sensor arrays, and the MWM-Array technology in particular, throughout the industry. This includes preparing papers for publication, presenting at conferences and workshops, and participating in industry forums.

Example technical meetings that have been attended include the 2010 PRCI Pipeline Program Research Exchange Meeting, 2010 International Pipeline Conference, the 2008, 2009, and 2010 Fall ASNT Conferences, and the 2010 Chevron NDE Forum.

6.6 References

1. N. Goldfine, V. Zilberstein, T. Lovett, "Pipeline & Piping Damage Mapping and Tracking using High-Resolution Imaging MWM-Arrays," ASNT International Chemical and Petroleum Industry Inspection Technology (ICPIIT) X Conference, Houston, TX, June 20-23, 2007.
2. N. Goldfine, "Magnetometers for Improved Materials Characterization in Aerospace Applications," *Materials Evaluation*, Volume 51, No. 3, March 1993.
3. N. Goldfine and D. Clark, "Introduction to the Meandering Winding Magnetometer (MWM) and the Grid Measurement Approach," SPIE NDE Techniques for Aging Infrastructure and Manufacturing, Scottsdale, Arizona; Dec., 1996. SPIE Proceedings, Vol. 2944, 1996. pp186-192.
4. N. Goldfine, et al., "Surface Mounted Periodic Field Current Sensors for Structural Health Monitoring," SPIE, Smart Structures and Materials NDE for Health Monitoring and Diagnostics, Newport Beach, California; March 2001.
5. N. Goldfine, V. Zilberstein, A. Washabaugh, D. Schlicker, I. Shay, D. Grundy, "Eddy Current Sensor Networks for Aircraft Fatigue Monitoring," *Materials Evaluation*, Volume 61, No. 7, July 2003, pp. 852-859.
6. U.S. Patent Nos. 5,453,689, 5,629,621, 5,793,206, 5,966,011, RE39,206, 6,784,662, 7,049,811, 7,385,392, 7,467,057, and pending patents.
7. Haus, H.A. and J.R Melcher, Electromagnetic Fields and Energy, Prentice Hall, Englewood Cliffs, NJ, 1989.
8. N. Goldfine, Y. Sheiretov, D. Schlicker, A. Washabaugh, "Rapid, Nonlinear "System" Identification for NDT, Using Sensor Response Databases," *Materials Evaluation*, Vol. 66, No. 7, July 2008.
9. N. Goldfine, A. Washabaugh M. Windoloski, V. Zilberstein, "Replacing magnetic particle and liquid penetrant inspections with high resolution MWM-Array eddy current imaging," ASM AeroMat Conference and Exposition, Baltimore, MD; June 26-27, 2007.